Structure and Properties
of Carbon Nanotubes

DISSERTATION

**zur Erlangung eines Grades eines Doktors
der Naturwissenschaften**

**der Fakultät für Mathematik und Physik
der Eberhard-Karls-Universität zu Tübingen**

vorgelegt von

Jannik Meyer

aus Herdecke

2006

Tag der mündlichen Prüfung: 3. Februar 2006

Dekan: Prof. Dr. Peter Schmid

1. Berichterstatter: Prof. Dr. Dieter Kern

2. Berichterstatter: Prof. Dr. Oliver Eibl

3. Berichterstatter: Prof. Dr. Angus I. Kirkland, University of Oxford, UK

List of publications

Parts of this work were published in:

Single-Molecule Torsional Pendulum
J. C. Meyer, M. Paillet, S. Roth
Science **309** pp. 1539-1541, (2005)

Raman modes of index-identified free-standing single-walled carbon nanotubes
J. C. Meyer, M. Paillet, T. Michel, A. Moreac, A. Neumann, G. S. Duesberg, S. Roth, J.-L. Sauvajol
Phys. Rev. Lett. **95**, 217401 (2005)

Electron diffraction analysis of individual single-walled carbon nanotubes
J. C. Meyer, M. Paillet, G. S. Duesberg, S. Roth
Ultramicroscopy **106** pp. 176-190 (2006)

Transmission electron microscopy and transistor characteristics of the same carbon nanotube
J. C. Meyer, D. Obergfell, S. Roth, S. Yang, S. Yang
Appl. Phys. Lett. **85** pp. 2911-2913 (2004)

Novel freestanding nanotube devices for combining TEM and electron diffraction with Raman and Transport
J. C. Meyer, M. Paillet, J.-L. Sauvajol, D. Obergfell, A. Neumann, G. S. Duesberg, S. Roth
In: H. Kuzmany, J. Fink, M. Mehring, S. Roth (eds.): *Electronic Properties of Novel Materials*, American Institute of Physics, New York, USA 2005. (AIP Conference Proceedings No. **768**, pp. 512-515)

Freestanding Nanostructures for TEM-Combined Investigations of Nanotubes
J. C. Meyer, D. Obergfell, M. Paillet, G. S. Duesberg, S. Roth
In H. Kuzmany, J. Fink, M. Mehring, S. Roth (eds.): *Electronic Properties of Synthetic Nanostructures*, American Institute of Physics, New York, USA 2004. (AIP Conference Proceedings No. **723**, pp. 540-543)

4

Publications related to this work:

Growth and physical properties of individual single-walled carbon nanotubes
M. Paillet, V. Jourdain, P. Poncharal, J.-L. Sauvajol, A. Zahab, J. C. Meyer, S. Roth, N. Cordente, C. Amiens, B. Chaudret
Diamond and Related Materials **14** pp. 1426-1431 (2005)

Selective growth of large chiral angle single-walled carbon nanotubes
M. Paillet, J. C. Meyer, T. Michel, V. Jourdain, P. Poncharal, J.-L. Sauvajol, N. Cordente, C. Amiens, B. Chaudret, S. Roth, A. Zahab
Diamond and Related Materials, in press (2006).

Vanishing of the Breit-Wigner-Fano Component in Individual Single-Walled Carbon Nanotubes
M. Paillet, P. Poncharal, A. Zahab, J.-L. Sauvajol, J. C. Meyer, S. Roth
Phys. Rev. Lett. **94**, 237401 (2005)

Versatile synthesis of individual single-walled carbon nanotubes from nickel nanoparticles for the study of their physical propertes
M. Paillet, V. Jourdain, P. Poncharal, J.-L. Sauvajol, A. Zahab, J. C. Meyer, S. Roth, N. Cordente, C. Amiens, B. Chaudret
J. Phys. Chem. B **108** pp. 17112-17118 (2004)

Progress in actuators from individual nanotubes
J. Meyer, J.-M. Benoit, V. Krstic, S. Roth
In: H. Kuzmany, J. Fink, M. Mehring, S. Roth (eds.): *Molecular Nanostructures*, American Institute of Physics, New York, USA 2003. (AIP Conference Proceedings No. **685**, pp. 564-568)

Transport and TEM on the same individual carbon nanotubes and peapods
D. Obergfell, J. C. Meyer, A. Khlobystov, S. Yang, S. Yang, S. Roth
In: H. Kuzmany, J. Fink, M. Mehring, S. Roth (eds.): *Electronic Properties of Novel Materials*, American Institute of Physics, New York, USA 2005. (AIP Conference Proceedings No. **768**, pp. 548-552)

Electrical Transport in Dy Metallofullerene Peapods
D. Obergfell, J. C. Meyer, P.-W. Chiu, S. Yang, S. Yang, S. Roth
In H. Kuzmany, J. Fink, M. Mehring, S. Roth (eds.): *Electronic Properties of Synthetic Nanostructures*, American Institute of Physics, New York, USA 2004. (AIP Conference Proceedings No. **723**, pp. 556-560)

Other publications:

Nanotomography based on hard x-ray microscopy with refractive lenses
C. G. Schroer, J. Meyer, M. Kuhlmann, B. Benner, T. F. Günzler, B. Lengeler
Appl. Phys. Lett. **81** pp. 1527-1529 (2002)

Parabolic refractive X-ray lenses
B. Lengeler, C. G. Schroer, B. Benner, A. Gerhardus, T. F. Günzler, M. Kuhlmann,
J. Meyer, C. Zimprich
Journal of Synchrotron Radiation **9** pp. 119-124 (2002)

Contents

Chapter 1

Introduction

The properties of nanoscopic objects depend critically on the position of each atom, since finite-size and quantization effects play an important role. For carbon nanotubes, for example, the electronic, mechanical, and vibrational properties vary significantly depending on their structure. Depending on the structure, a nanotube can be e.g. either metallic or semiconducting with varying band-gaps. In investigations on nanometer-sized objects often the problem arises that the true nature of the object is not fully known. The interpretation of such measurements then depends on assumptions, and leads to unclear conclusions.

Yet, most investigations on individual carbon nanotubes are carried out on objects with unknown structure. After more than a decade of intensive research in carbon nanotubes it is still not possible to sort or grow a specific single nanotube structure, as defined by the tube indices (n,m). All production and sorting procedures end up with a mixture of different indices. For practical applications, it might be sufficient to sort metallic from semiconducting nanotubes. But for understanding the physics of a single molecule, it is desired to know the precise structure of the object under investigation.

The analysis of individual single-walled nanotubes (SWNTs) is commonly done by Raman spectroscopy or electric transport measurements, providing information about the vibrational properties and electronic structure. In the case of Raman spectroscopy, the nanotube structure can be sometimes derived from the spectroscopic data by a modelization of electronic and vibrational properties. But no previous work exists where an unambiguous independent identification of the SWNT lattice structure is possible on the same nanotube as the Raman or transport measurement.

This very problem was solved in this work by developing a versatile approach that facilitates an electron diffraction analysis in a transmission electron microscope (TEM) in combination with a wide range of experimental techniques on the precisely same nano-object. I present an analysis of Raman active vibrational modes of individual single-walled carbon nanotubes, with an independent and unambiguous identification of the nanotube lattice structure by electron diffraction. I

11

also present electronic transport measurements, partly in a transistor configuration, again with an independent characterization of the same object by high-resolution transmission electron microscopy and electron diffraction. The results allow a verification of conclusions drawn from previous experiments on unidentified nanotubes.

Further, I show various novel devices based on individual single-walled carbon nanotubes. These include free-standing contacted nanotubes for TEM in-situ transport measurements, and nanoelectromechanical devices, comprising individual SWNTs as molecular-scale motion-enabling element. The in-situ transport measurements provide important data on modifications of the metal-nanotube contact, and allow a visualization of nanotube breakdown. The nanoelectromechanical devices demonstrate the enormous potential for carbon nanotubes in future integrated devices that may be not only electronically but also mechanically active.

The common aspect in all these experiments is that they are carried out on individual molecules that are precisely characterized, by high-resolution TEM and electron diffraction. This is a new quality not common in investigations on this class of materials. It may thus provide a direct test e.g. for molecular dynamics simulations. We expect that the developed techniques are also applicable to measurements on various other nanostructures and nanomaterials, or different types of combined investigations.

Chapter 2

Carbon nanotubes - Structure and properties

Carbon nanotubes are long hollow cylindrical molecules made up solely from carbon. Most of the fascination for this novel material, and many of its unique properties, stem from the unusual structure and aspect ratio. The cylinder is made up from a single layer of sp^2 bonded carbon, with a hollow inner channel, a diameter of a few nanometers, and a length of typically several micrometers. They are often considered as truly one-dimensional systems and exhibit unusual electrical and mechanical properties.

2.1 Structure

The carbon nanotube can be considered as a graphene sheet rolled into a cylinder (graphite is a layered three-dimensional material, and a single layer of graphite is called 2D graphite, or a *graphene* layer). The structural indices (n,m) of the nanotube define how the nanotube would be formed from the graphene sheet. This is illustrated in Fig. 2.1.
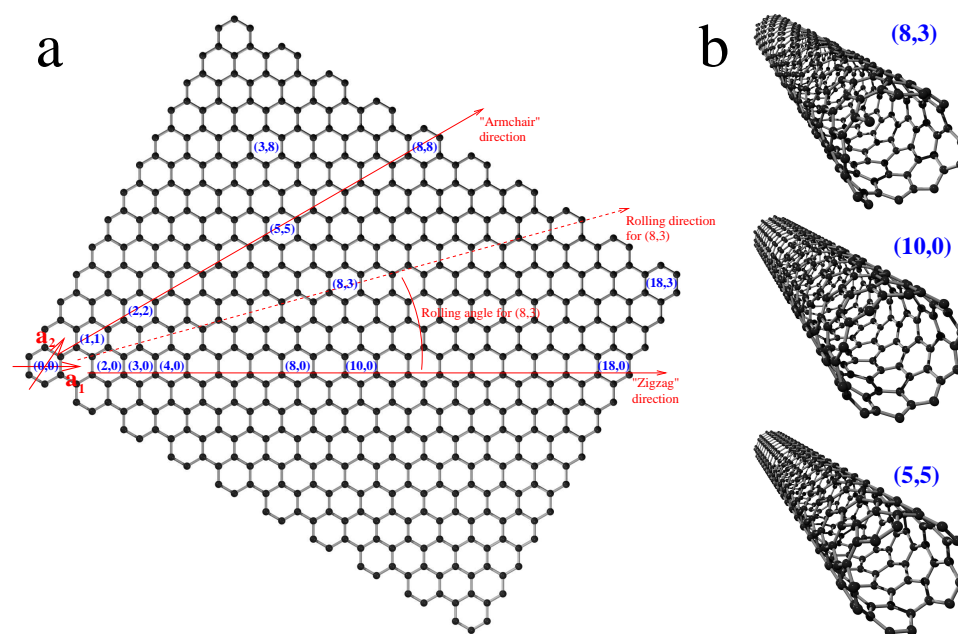
Figure 2.1: (a) A planar graphene sheet with a coordinate system (red arrows). Starting from (0,0) each hexagon (n,m) in the plane is reached by n and m steps along the graphene lattice vectors a_1 and a_2. The carbon nanotube is formed by rolling the graphene sheet so that the hexagons (0,0) and (n,m) coincide. For example, the (8,3) nanotube is formed by rolling the graphene sheet with an angle and radius so that the hexagons denoted by (0,0) and (8,3) coincide on the cylinder surface. The (3,8) nanotube is mirror-symmetric to the (8,3) (left and right-handed enantiomers). (b) (8,3) nanotube, (10,0) "zigzag" nanotube, and (5,5) "armchair" nanotube.

If the indices are (n,0) or (n,n), the nanotubes are achiral molecules. They are denoted as "zigzag" (n,0) and "armchair" (n,n), due to the shape of the graphene sheet edges (or tube ends). The remaining nanotube species (n,m) with m$\neq$ 0 and n$\neq$m are chiral molecules, i.e. they are not identical with their mirror images. The two enantiomers can be represented as (n,m) and (m,n). However in many cases it is of no importance whether the right- or left handed enantiomer is present, and the nanotube is simply indexed as (n,m) with 0<m<n.

We use here, like in the majority of recent literature on carbon nanotubes, base

vectors including an angle of $60°$. However we note that sometimes base vectors with an angle of $120°$ are used (e.g. in [1, 2]), which leads to different indices for the same nanotube.

From the indices (n,m), and the length of the carbon-carbon bond a_{CC} we can calculate the diameter d of the nanotube

$$d = \frac{\sqrt{3} \cdot a_{CC}}{\pi} \cdot \sqrt{n^2 + nm + m^2} \tag{2.1}$$

and the rolling angle θ as indicated in Fig. 2.1:

$$\theta = \arcsin \frac{\sqrt{3} \cdot m}{2\sqrt{n^2 + nm + m^2}} \tag{2.2}$$

The structure described above is a single-walled carbon nanotube (SWNT). It is the molecule mainly investigated in this work. There exist also multi-walled carbon nanotubes (MWNTs), which consist of multiple concentric SWNTs, stacked with an inter-wall distance close to that of graphite.
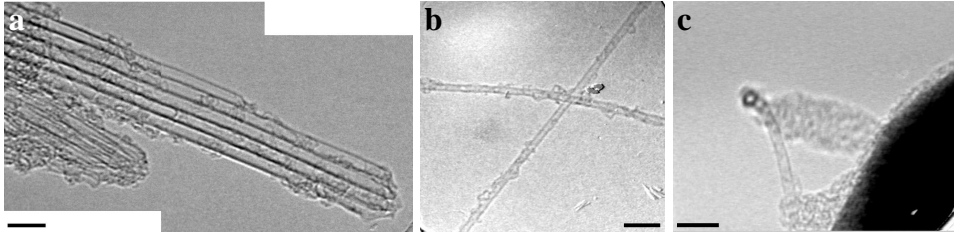
Figure 2.2: TEM images of SWNTs. (a) Short bundle of arc-grown SWNTs. (b) Small diameter CVD grown individual SWNTs. (c) SWNT oriented so that the direction of view is along the tube on a short segment of the curved nanotube. The images were obtained in a Philips CM200 microscope operated at 120kV. All scale bars are 5nm. The object near the crossing point of the tubes in (b) is a blind spot on the camera.

The structure of carbon nanotubes is confirmed by diffraction experiments (Chapter 4), atomic resolution STM imaging [3, 4, 5, 6], and atomic resolution TEM imaging [7, 8, 9].

As an alternative approach to the rolled-up graphene sheet, a carbon nanotube can be described as a set of helices, where each helix is a chain of carbon atoms (Fig. 2.3). This approach is useful for an analytic description of the carbon nanotube diffraction pattern [10, 11, 12, 13, 14] by using the same concepts as for DNA and other helical structures [15].
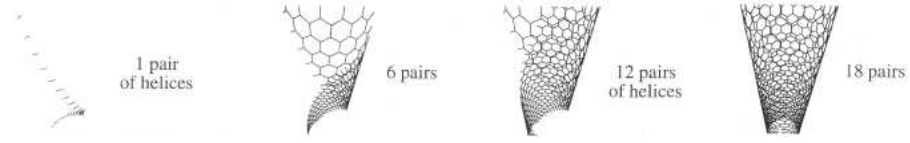
Figure 2.3: Building a carbon nanotube from a set of helices (from [12]).

2.2 Electronic properties

2.2.1 Prerequisites

2.2.1.1 One-dimensional systems

The properties of a physical system depend on its dimensionality. In a one-dimensional system, the electron is free to move in one direction, while it is confined in the other two directions. We choose the x-axis to be along the nanotube, and assume for the moment that the potential for the conduction electron only depends on the other two coordinates, y and z:

$$V = V(y, z) \tag{2.3}$$

With an ansatz $\Psi(x, y, z) = \Phi(y, z) \exp(ik_x x)$ for the Schrödinger equation we obtain the energy eigenvalues

$$E = \frac{\hbar^2 k_x^2}{2m} + E_j \tag{2.4}$$

where only the discrete values E_j depend on the shape of the potential. The density of states in one dimension is

$$D(E) \sim \frac{1}{\nabla_k E(k)} \tag{2.5}$$

so we obtain $D(E) \sim \frac{1}{\sqrt{E-E_j}}$ (Fig. 2.4)

We see that the density of states diverges for energies $E = E_j$. These points are the so-called Van Hove singularities. In reality the potential also depends on the coordinate along the tube axis. But the potential $V(x, y, z)$ must be a *periodic* function of the axis coordinate. As a result, the dispersion relation $E(k_x)$ and density of states $D(E)$ are different from that of a free electron. But in any case, in Eq. (2.5), a divergence in the density of states occurs where $\nabla_k E(k) = 0$, so we see that the Van Hove singularities are solely related to the dimensionality.

2.2.1.2 Charge transport

Each branch in the dispersion relation $E(k)$ contributes to the density of states as
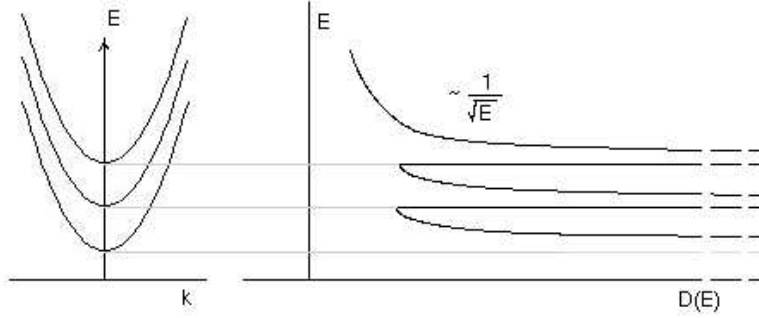
Figure 2.4: Dispersion relation and density of states in one dimension

$$D(E) = \frac{g_s}{\pi} \cdot \frac{1}{\nabla_k E(k)} \tag{2.6}$$

where g_s is the spin degeneracy factor (here $g_s = 2$). The velocity of an electron is

$$v = \frac{1}{\hbar} \nabla_k E(k). \tag{2.7}$$

The current can be calculated as

$$I_\pm = e \int_0^{\mu_\pm} D(E) v(E) = \frac{g_s e}{h} \mu_\pm \tag{2.8}$$

where we consider separately the contributions of electrons with negative '-' and positive '+' velocity. In an equilibrium $\mu_+ = \mu_-$ and the total current $I = I_+ - I_-$ is zero. However if there is a contact between two reservoirs with a potential difference $eU = \mu_+ - \mu_-$, we obtain a current

$$I = \frac{g_s e}{h} (\mu_+ - \mu_-) = \frac{g_s e^2}{h} U. \tag{2.9}$$

Equation 2.9 is derived for the idealized case of a point contact between two reservoirs. It is valid if the electron transport between the reservoirs occurs without scattering (Fig. 2.5). Note that Equation 2.9 is independent from the actual density of states. The ratio

$$G_0 = \frac{I}{U} = \frac{g_s e^2}{h} \tag{2.10}$$

is the *conductance quantum*. The inverse of G_0 corresponds to a resistance of

$$R_0 = \frac{1}{G_0} \approx 12.9 \text{k}\Omega \tag{2.11}$$
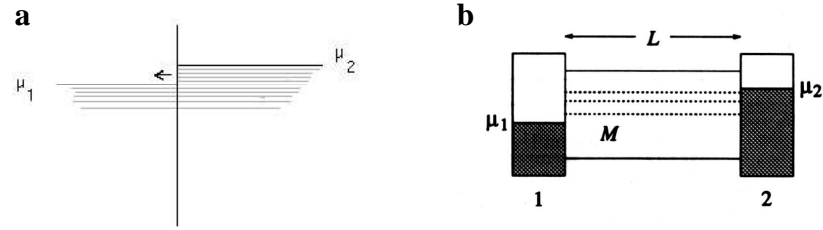
Figure 2.5: (a) Transport across a quantum point contact between two reservoirs at potentials μ_1 and μ_2. (b) Ballistic transport between two spatially separated reservoirs, at a distance L and connected via M conducting channels (from [16] with modifications).

The above considerations were made for a single branch in the dispersion relation. In the general case there are M occupied so-called *conduction channels* that contribute to the current. Thus, the conductance is a multiple of the conductance quantum:

$$G = M \cdot G_0 \tag{2.12}$$

A number of $M = 2$ channels are expected to contribute to the electronic transport in a carbon nanotube.

Ballistic transport is given if electron transport occurs without scattering, as described above, but between spatially separated reservoirs. The connection between the reservoirs is then called a ballistic conductor. In this case the conductivity is again expected to be a multiple of G_0. The entire energy is dissipated in the contacts.

Ballistic transport is possible if the length of a conductor L is smaller than the momentum and phase relaxation lengths L_m and L_ϕ.

2.2.2 Electronic structure of the carbon nanotube

The band structure of a carbon nanotube can be approximated by imposing cyclic boundary conditions on the band structure of planar graphene. The reciprocal lattice of the two-dimensional hexagonal structure is again a hexagonal lattice, but rotated by 90°. The dispersion relation of graphene is shown in Fig. 2.6. It is calculated in a tight binding approximation for the π electrons, which determine the transport properties because the σ orbitals are fully occupied [16]. The 2D graphene sheet is semi-metallic with a linear dispersion relation near the K point and the Fermi level crossing through the K points.

We can now consider the cyclic boundary condition imposed by wrapping the graphene sheet into a tubular structure. The electron wave vector along the tube
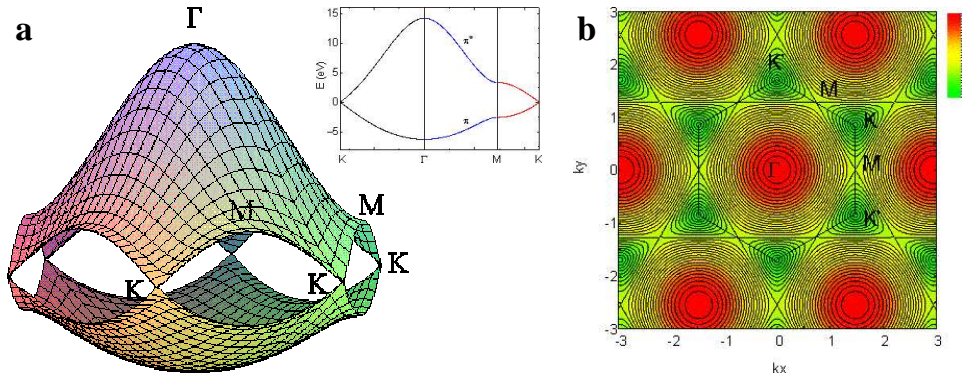
Figure 2.6: Dispersion relation in the first Brillouin zone for planar graphene. (a) A three-dimensional representation showing the conduction (upper) and valence (lower) band. The Fermi level crosses precisely through the K points. (b) Colour-coded representation of the conduction band Energy, with the first Brillouin zone indicated by the hexagon. Shown as inset is the dispersion relation along the high symmetry directions. Images are from [17].

axis $k_{\parallel}$ is not restricted. The wave vector on the circumference $k_{\perp}$ must now obey the relation

$$2\pi n = k_{\perp}\pi d$$

where d is the diameter of the nanotube. The remaining allowed wave vectors can be represented as a set of lines in the dispersion relation of graphene (Fig. 2.7).

In graphene, the conduction and valence band intersect only in the K points. If the graphene sheet is wrapped so that an allowed state remains on the K point, we obtain a metallic carbon nanotube. Otherwise, the nanotube is semiconducting. From these geometrical arguments it can be derived that nanotubes with indices (n,m) where $n - m$ can be divided by 3 will have an allowed state on the K point of the graphene sheet. Therefore, they are expected to be metallic. The remaining tubes are semiconducting, with a band gap proportional to the inverse of the diameter. More precise calculations [18] find that in reality most "metallic" nanotubes also have a tiny band gap induced by the curvature of the graphene sheet, and are in fact small band gap semiconductors. This has been confirmed by low temperature scanning tunnelling microscopy and spectroscopy measurements [19]. We conclude that the electronic properties of a carbon nanotube sensitively depend on the lattice structure. As a summary the following tube species are possible:

1. Semiconducting nanotubes, where $n - m$ is not an integer multiple of 3. The band gap is $\sim 1/d$, and in the order of 0.3-1.0 eV for common SWNT diameters.
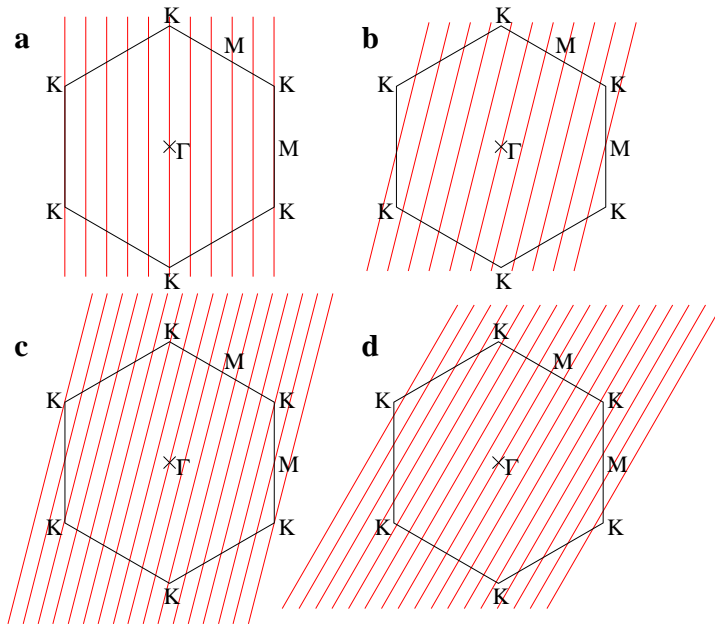
Figure 2.7: Allowed states in the 1st Brillouin zone of graphene, after imposing cyclic boundary conditions due to wrapping the graphene sheet into a cylinder. If there are allowed states on the K-point of the graphene reciprocal lattice, we obtain metallic carbon nanotubes, otherwise, the nanotube is a semiconductor. (a) is for an armchair nanotube (which is always metallic), (b) semiconducting chiral tube, (c) (quasi-) metallic chiral tube, (d) semiconducting zigzag tube.

2. Quasi-metallic (small band gap semiconducting) nanotubes. Here, $n - m$ is an integer multiple of 3, but $n \neq m$. The gap is $\sim 1/d^2$ and also angle dependent. It is <0.02 eV for typical SWNT diameters.

3. Metallic nanotubes (with no curvature-induced small band gap) are the "armchair" types ($n = m$).

Figure 2.8 shows calculated and measured electronic density of states (DOS) vs. energy for individual SWNTs. The Van Hove singularities, as expected for a one-dimensional system, are clearly observed. The semiconducting nanotubes have a vanishing DOS near the Fermi energy, and the band gap is given by the distance of the two nearest Van Hove singularities.

2.2.3 Transport properties

We have described above the expected behaviour for an ideal ballistic conductor. Ballistic transport has been shown in nanotubes [20, 21, 22], but the ideal behaviour is rarely observed. In most real devices the two-point transport charac-
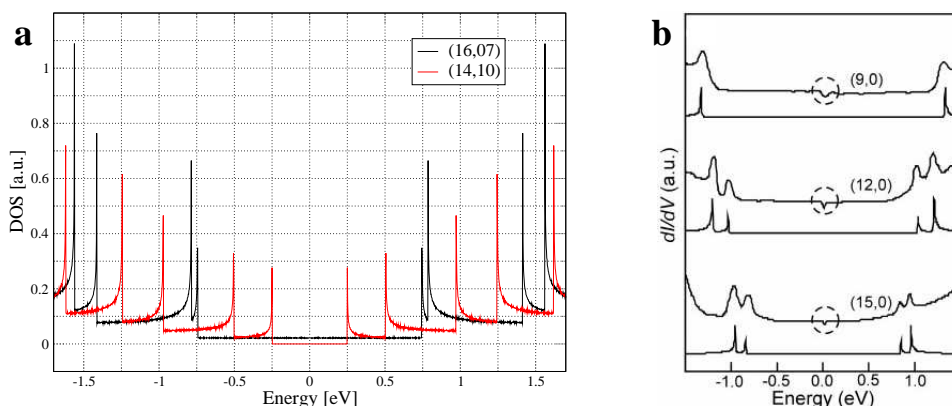
Figure 2.8: (a) Calculated density of states (DOS) for a (16,07) quasi-metallic and (14,10) semiconducting nanotube (data from [17]). The energy is given relative to the Fermi energy of the undoped tube. (b) DOS obtained from scanning tunnelling spectroscopy (STS) experiments after [19]. The STS data shows the curvature-induced band gap in metallic zigzag-type nanotubes. The Van Hove singularities are also clearly observed. The indices were derived from atomically resolved STM images on the same nanotube. Shown below each line is the calculated DOS for comparison.

teristic is dominated by the contact resistances. Also the nanotube itself can decay into several electronically separated or weakly coupled sections e.g. due to defects [23].

A measurement from [21], where an AFM tip is used as a local voltmeter, is shown in Fig. 2.9. This measurement confirms that the potential drop occurs primarily at the contacts, not along the nanotube bundle. With this method also the presence of isolated defects, leading to separated, weakly coupled tube segments, was observed [23].

Figure 2.10a shows the schematic of a carbon nanotube contacted in a widely used two-point probe / field effect transistor (FET) configuration. The nanotubes are either absorbed on the substrate from a suspension, or grown directly on the substrate. Metal contacts are fabricated by lithographic means, in our case by electron beam lithography. The highly doped substrate, separated from the nanotube by an insulating oxide layer, serves as gate electrode. An effective gate electrode is important for investigating the electronic properties of a SWNT. Figure 2.10d shows the transfer characteristic of this device. The red part of the curve is the p-conduction regime. As-prepared SWNTs are usually p-doped. If the coupling to the gate is weak, only the p-conduction regime is measured (which is very often the case). In this sample the tube can also be tuned to the n-type conduction regime (the green part of the curve in Fig. 2.10d).
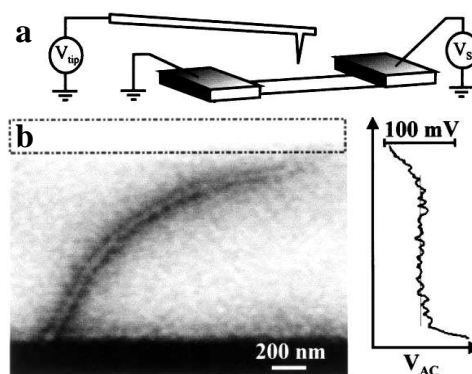
Figure 2.9: Scanned probe microscopy of the electric transport in a carbon nanotube, after [21]. (a) Schematic of the measurement. Electrostatic force microscopy is employed to use an AFM tip as local voltmeter. (b) The potential profile along the nanotube bundle is nearly constant, while the potential drops at the metal-nanotube interface.

2.2.4 Schottky barriers

At the interface between a semiconducting and a metallic region it is well known that a Schottky barrier is formed. The height of these barriers depend on the work function, and can be varied and minimized by an appropriate choice of materials. A Schottky barrier also forms at the interface between a semiconducting carbon nanotube and the metal contact.

The band bending for a carbon nanotube in a transistor configuration, with a bias between source and drain, is shown qualitatively in Fig. 2.11. Fig. 2.11a corresponds to the "off" state: The source and drain energy levels are within the band gap of the nanotube. In Fig. 2.11b the band edges of the nanotube are shifted by a negative gate voltage. The FET is in the "on" state, dominated by hole conduction. The Schottky barrier at the source and drain is overcome by tunnelling and thermal emission processes.

As shown in Fig. 2.10 it is sometimes also possible to reach an n-type electron conduction regime at positive gate voltages. However, this is not achieved regularly because most as-produced SWNTs are p-doped, probably by exposure to oxygen. It therefore requires much higher gate potentials to reach an n-conduction regime, and this is often outside the gate voltage limits given by the breakdown field of the insulators.

2.3 Vibrational properties and Raman spectroscopy

Vibrational properties of a molecule can be probed by Raman spectroscopy. When light is scattered from a molecule, a very small fraction of the light is scattered
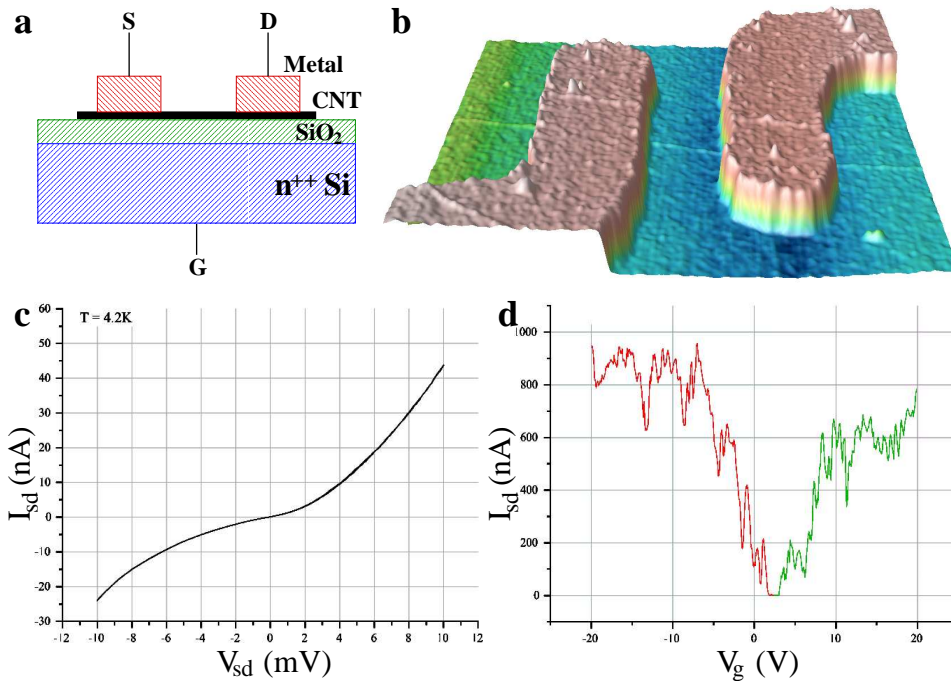
Figure 2.10: (a) Carbon nanotube contacted in a two-point probe configuration (schematic). The tube is absorbed or grown on a Si substrate with an isolating oxide layer. Metallic contacts are prepared by electron beam lithography. A field-effect transistor (FET) configuration is obtained e.g. by using a highly doped substrate as gate (G), and the metal contacts as drain (D) and source (S). (b) AFM image (3D representation) of a carbon nanotube with metal contact. The height of the metal is $\approx 25nm$, the contact distance (effective CNT length) $\approx 300nm$. (c) typical current-voltage characteristic and (d) FET transfer characteristic of the same device. The red part of the curve is the p-conduction regime, while the green curve is the n-type region. Our measurements on this device are discussed in section 6.1.2.

at optical frequencies different from that of the incident photons. This inelastic scattering process can occur with a change in vibrational, rotational or electronic energy of the molecule. Here we will only consider the scattering events associated with a vibrational mode of our molecules. The Raman process is a three-step process consisting of (i) an absorption of the photon into an electronic excitation of the molecule, (ii) generation or absorption of a phonon, (iii) emission of a photon (Fig. 2.12).

The probability for the above described process is very low ($\sim$ 1 in 10^7 photons) because it involves the excitation to a virtual level which is only allowed for a very short time within the uncertainty principle. The probability is strongly increased, typically by a factor of $10^2 - 10^4$, if the transition for either the absorbed or the emitted photon coincides with an electronic transition of the molecule. This
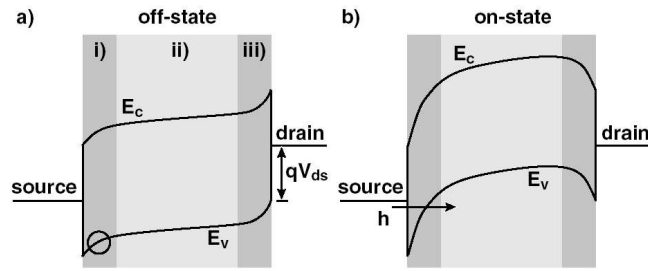
Figure 2.11: Band diagram for a semiconducting nanotube with metallic contacts and a finite bias V_{ds} between source and drain (from [24]). The gate voltage affects the energy levels in region (ii). (a) Current flow is suppressed for gate voltages corresponding to the "off" state of the field effect transistor. Depending on bias and gate voltage, the band bending in region (iii) could also be oriented as in (i), which would lead to an additional barrier at the drain. (b) Significant tunnelling of holes (h) through the Schottky barrier occurs at sufficiently high negative gate voltages, corresponding to the "on" state of the FET.

is called *resonant Raman* spectroscopy. In the case of carbon nanotubes the cross section for a resonant Raman process is so large that it is actually possible to analyse the vibrational modes of *individual* SWNTs in this way. Further, it is possible to obtain information about the electronic transitions from the photon energies at resonance.

Figure 2.13 shows two examples of Raman active vibrational modes in single-walled carbon nanotubes. The so-called radial breathing mode (RBM) is a fingerprint of single-walled carbon nanotubes. Then there is a set of modes called tangential modes (TM), which are also found in planar graphite, but which are diameter and angle dependent in the carbon nanotube. The Raman shift ν is given as

$$\nu = \frac{1}{\lambda_{incident}} - \frac{1}{\lambda_{scattered}} \tag{2.13}$$

and typical values are $100...300 \text{cm}^{-1}$ for the RBM (diameter dependent) and $1500 - 1600 \text{cm}^{-1}$ for the TM. Further, there is a feature between 1300 and 1350cm^{-1} called D-line which is associated with defects and amorphous carbon. A small D line is generally interpreted as indication of a good sample quality.

Figure 2.14 shows a typical Raman spectrum obtained from an individual single-walled carbon nanotube. Clearly visible is the RBM and two tangential modes, while the D mode is hardly visible. Just precisely how the Raman active vibrational modes depend on the nanotube structure is still a topic of discussion. In chapter 5 it will be addressed by a direct measurement of Raman modes on individual nanotubes with indices identified by electron diffraction.
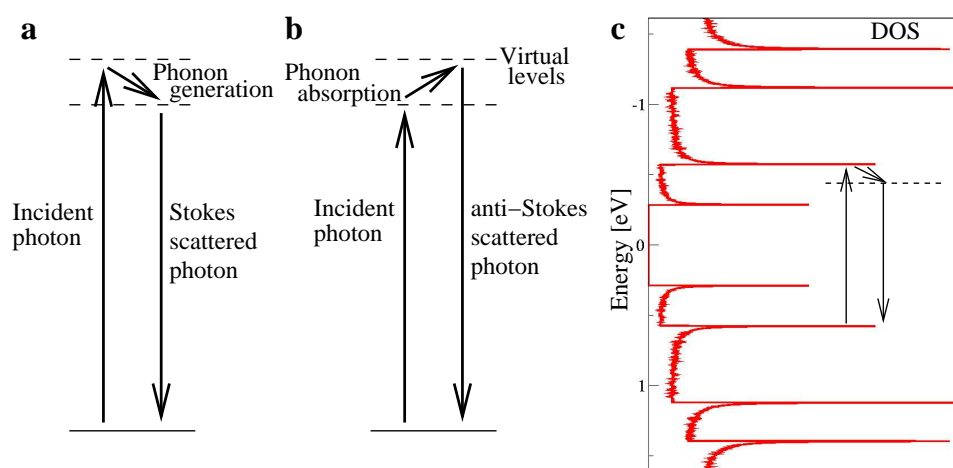
Figure 2.12: Energy level diagram for Raman scattering. The molecule is excited to a virtual state and almost immediately de-excited, with a small energy difference correspondig to a change in vibrational energy. In the Stokes process (a), the incident photon is absorbed, a phonon is generated, and the excitation relaxes (electron - hole pair recombines) by emission of another photon. In the anti-Stokes process (b) a thermally excited phonon is absorbed, and a photon with a slightly higher energy is emitted. The ratio of the anti-Stokes to Stokes intensity is a measure of the temperature. (c) If either the incident or the scattered photon energy matches an electronic transition, the Raman signal is strongly increased (resonant Raman scattering). Depicted in (c) is the DOS for a semiconducting nanotube and an incident photon matching the energy difference between the second Van Hove singularities.

a

b

RBM

TM
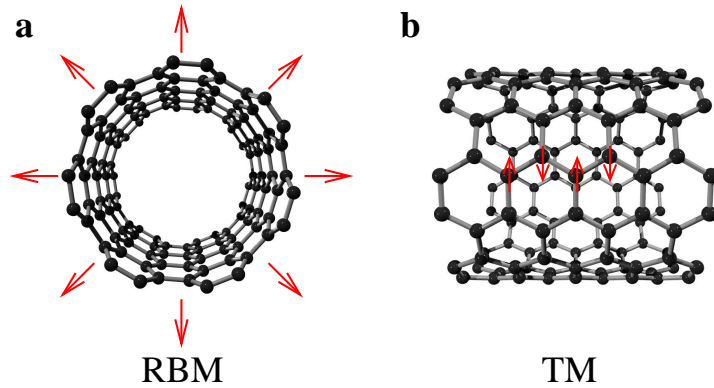
Figure 2.13: Raman-active vibrational modes of carbon nanotubes. (a) The so-called *radial breathing mode* (RBM) is a prominent feature of the tubular nano-structure, and not present in planar graphite. (b) is an example of a *tangential mode* (TM). In analogy to graphitic Raman modes it is often also called G-mode, or high-energy mode (HEM).

a

b
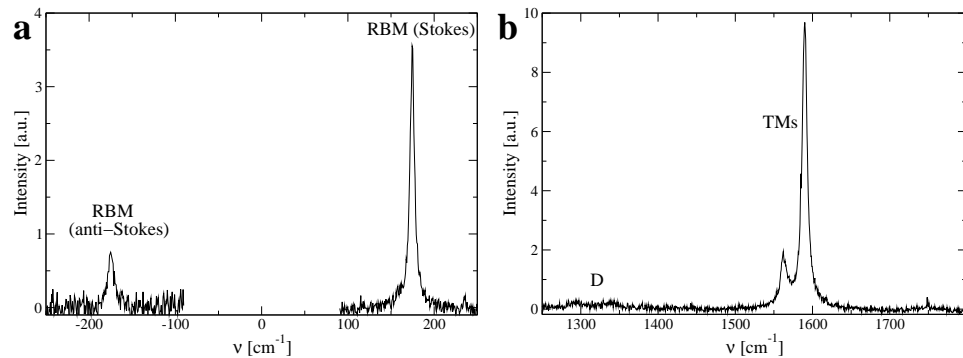
Figure 2.14: (a) Stokes and anti-Stokes spectra of the RBM measured on an in-dividual free-standing single-walled carbon nanotube. (b) TM range of the same nanotube. Two tangential modes are observed. The D mode is very small. The experimental procedure is described in chapter 5.

Chapter 3

Sample preparation

The experimental techniques developed within this work make it possible to perform various measurements on carbon nanotubes with identified structural indices (n,m). As described in the next chapter, the nanotube structure can be unambiguously identified by electron diffraction in a transmission electron microscope (TEM). In a TEM, as the name implies, the *transmitted* electrons have to reach the detector. Measurements on individual carbon nanotubes, however, are most commonly carried out on nanotubes lying on a substrate. Therefore, with the established techniques, TEM and Transport, Raman or AFM investigations on the same object are mutually exclusive. Further, the developed methods allow a preparation of novel devices for in-situ electrical and mechanical measurements.

3.1 Principle of sample preparation

The common principle behind all samples prepared for TEM and electron diffraction analysis in this work is a free-standing structure prepared on the edge or corner of a substrate. The structures are prepared by electron beam lithography and made free-standing in an etching process. Structures that reach out across the edge of the substrate can be investigated by TEM, while objects on a bulk substrate can not.

3.1.1 Underetching sideways from the cleaved edge

Underetching a metal structure from the side of the cleaved edge makes it possible to design almost arbitrary free-standing structures by electron beam lithography. It is therefore a highly versatile approach that facilitates many different types of experiments. Figure 3.2 illustrates the procedure. Before etching, the nanotube is on the substrate. At this point, transport measurements can be carried out in which the substrate (with insulating layer) serves as gate. After etching, the nanotube is free-standing, held in place by the metal structure. It can now be investigated by TEM. Also, it is possible to do transport measurements (without back-gate), or Raman spectroscopy on the free-standing nanotube.
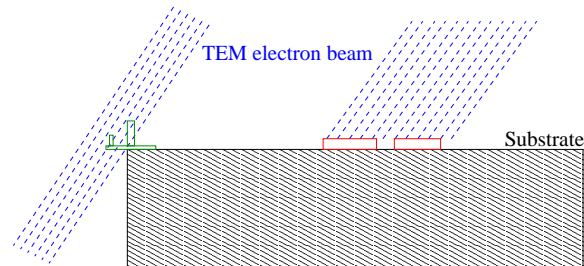
Figure 3.1: Idea behind the sample preparation: A structure on the edge or corner of a substrate can be investigated by TEM, but objects above the bulk substrate can not.
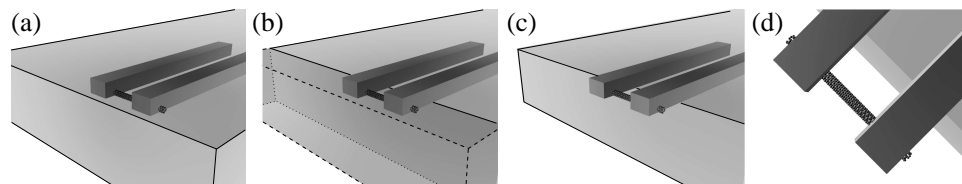
Figure 3.2: Principle of sample preparation: (a) The desired structure, here two contacts on a nanotube, is prepared close to a cleaved edge of the substrate. (b) An etching process removes the volume indicated by the dashed lines. (c) The result is a structure that reaches out across the side edge of the substrate. (d) Viewed from top, the contacts with the nanotube can be investigated in a transmission electron microscope since the substrate is no longer in the line of sight.
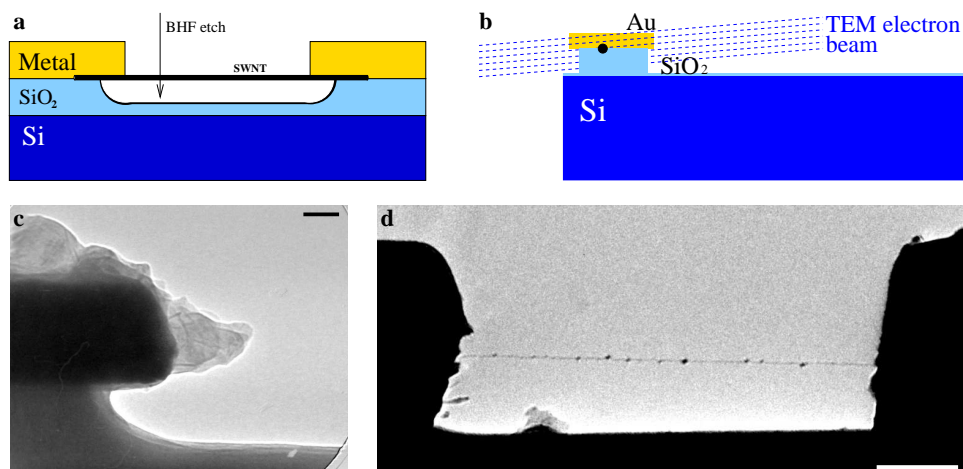
Figure 3.3: (a) Free-standing tubes above the substrate can be prepared by under-etching e.g. with buffered HF. (b) If they are prepared very close (1-2μm) to the edge of the substrate, they are accessible by TEM under a viewing angle nearly parallel to the substrate surface. The line of sight is now along the trench across which the nanotube is suspended. (c) TEM image of an underetched metal block close to the sample edge (with some debris on top). (d) TEM image of a free-standing individual SWNT prepared in this way. Scale bar 50nm (c) and 100nm (d).

This concept is used in the vast majority of experiments shown here, and will be described with experimental details in section 3.2. Figure 3.4 shows an example of a free-standing grid structure prepared in this way.

3.1.2 Isotropic underetching near the corner

Another approach is to prepare a free-standing nanotube, raised above the substrate level, very close to a corner of the substrate. In this way, the bulk substrate is still very close to the nanotube and may serve as a gate. However, only nanotubes very close to the edge (1-2μm) are visible. Although a promising solution, the aforementioned procedure turned out to be more practical and versatile, so that this method was only rarely used for actual measurements. Figure 3.3 shows the principle and example of these samples.

3.2 Experimental details

3.2.1 Nanotube growth and deposition on substrates

For most experiments shown here, the carbon nanotubes are grown by chemical vapour deposition on highly doped Si substrates with a 200nm oxide layer. One of the processes is described in detail in [25, 26]. Shortly, Ni nanoparticles with a diameter of $\approx 5nm$ are dispersed in ethanol and deposited on the substrate by spin

coating. Then, nanotube growth takes place at $850°$C in a flow of mostly H_2 and Ar, mixed with less than 1% of C_2H_4 or CH_4 as carbon feedstock. The density of the nanotube network obtained in this way can be varied within a wide range by adjusting the density of the catalyst particles, the feedstock gas, and growth time. We also used smaller diameter tubes grown at $600°$C (growth process described in [27]). In any case, we find that if the density of the grown nanotubes is low enough, a majority of *individual* nanotubes is obtained. At higher densities, nanotubes tend to combine into small bundles or ropes.

Alternatively, nanotubes can be deposited from a suspension. For this purpose, nanotubes are mixed with a 1% SDS (Sodium Dodecyl Sulphate) solution by ultrasonic agitation. The silicon dioxide surface of the substrate is modified by treatment with 3-aminopropyltriethoxysilane or N-[3-(trimethoxysilyl)propyl]ethylenediamene, leading to a surface terminated by long chain molecules with ammonium groups. The thus modified substrate is dipped into the nanotube SDS suspension for a few minutes. Afterwards, it is thoroughly washed with deionized water. This wet processing clearly leads to more bundles than CVD growth. Also, the chemical treatment, and SDS remains after rinsing, lead to an undesired layer of dirt on the substrates. However, a pre-treatment of the raw material is possible. It can be purified by oxidization and acid treatment, or the nanotube can be filled with fullerenes for transport measurements on hybrid structures (so-called "peapods").

3.2.2   Lithography on the edge

All structures were prepared by standard electron beam lithography, thermal evaporation and a lift-off process. The substrate is coated with a double-layer polymethylmethacrylate (PMMA) resist system consisting of 300nm 200K and 80nm 950K PMMA. After exposure and development, metal is deposited by thermal evaporation. Finally, the excess metal and resist is removed by a lift-off process in methylpyrrolidone.

Depending on the type of experiment, up to three lithography steps are carried out. The first step is the preparation of alignment markers. After locating potentially interesting nanotubes by AFM, contacts for transport measurements are made in a second step. After the transport measurement, a support structure is formed in a third lithography step before the sample can be etched for TEM investigations.

The main obstacle is to obtain a structure like shown in Fig. 3.4a close to the cleaved edge of a substrate. By ordinary spin coating, a well-defined resist layer is formed only in the center of the substrate, but it has an undefined thickness closer to the edges. We have found three different solutions to this problem:

1. In some cases it is sufficient to prepare a grid structure in the central region of the substrate, and then cleave the substrate through this grid (Fig. 3.5). The line of cleavage can be controlled within $\pm 20 \mu$m. In this case an ordinary
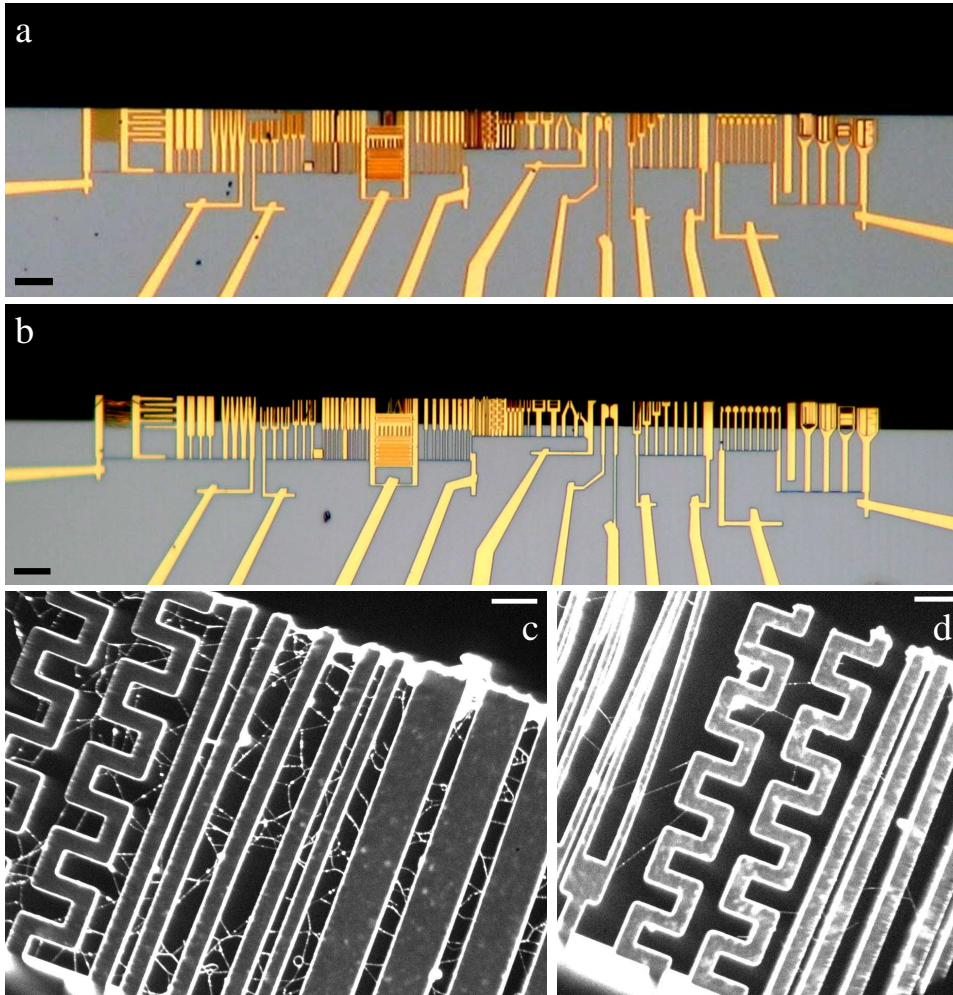
Figure 3.4: Sample preparation. (a) The grid structure, prepared by electron beam lithography on top of the nanotube network, close to the cleaved edge of the substrate. (b) After etching, part of the grid is free-standing. This free-standing part can be observed by TEM. (c) shows a dark-field mode TEM image of a high-density sample, (d) a low-density sample. Especially in lower-density samples, long straight individual SWNTs of high purity (depending on CVD conditions) are obtained. The dark-field mode is used here since the clean SWNTs are not seen in bright-field mode at lower magnifications. Scale bars are 10μm in (a) and (b), and 1μm in (c) and (d).
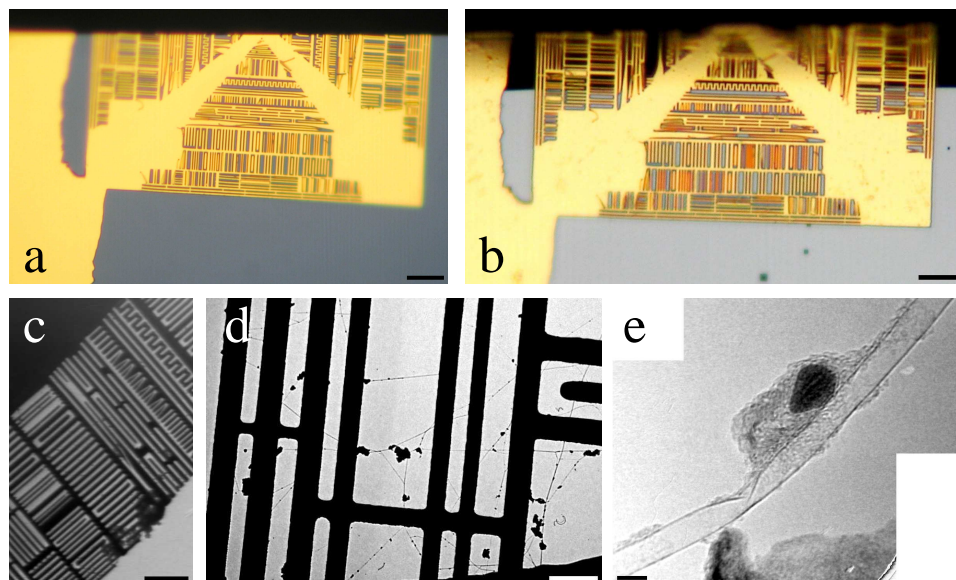
Figure 3.5: (a) A metal grid structure prepared by electron beam lithography. The sample was cleaved through the grid structure. (b) After etching, part of the metal grid is free-standing and reaching out across the side edge of the substrate. (c) Low magnification TEM image showing part of a free-standing structure. (d) Carbon nanotubes suspended within the grid. (e) High-resolution image of a nanotube with a kink, and a catalyst particle that failed to form a nanotube. Scale bar 10μm (a+b), 5μm (c), 1μm (d), 5nm (e).

electron beam lithography process is carried out, followed by a carefully prepared cleaving step.

2. If only one lithography step is needed, but the distance to the edge must be controlled with a higher precision, the substrate is cleaved after spin-coating with PMMA but before lithography. The structure to be written can now be aligned with the cleaved edge.

3. For multiple lithography steps close to the edge, the substrate is cleaved, and afterwards the two pieces are glued together again. In this way, a sufficiently smooth surface is obtained for spin-coating the resist. During lift-off, the two pieces fall apart again, and have to be glued together once more for the next step.

3.2.3 Etching

Different etching parameters were found for obtaining free-standing lithographic structures:

1. The more simple process for silicon substrates is a 6 hours etch in 30% KOH at 60°C. The KOH removes the bulk Si, and slowly the oxide layer. Thus, the structure is undercut mostly from the side. The etching process has to be stopped when the oxide layer is completely removed in the free-standing part, but still present on the substrate. The etch rate of the bulk Si can be controlled by electrically biasing the substrate with respect to the etching solution. The etch process is monitored with an optical microscope, and the bias is switched to a positive potential on the bulk Si as soon as the free-standing part has the desired width. This stops the etching on the bulk Si, while the etching on the oxide layer continues. The surface tension of small hydrogen bubbles formed on the Si surfaces creates significant mechanical stress on the free-standing structures.

2. A two-step etch process for silicon substrates consists of a TMAH etch (15%, 60°C) to under-etch the structure and oxide layer from the side of the cleaved edge, followed by a buffered HF etch (6.5%, 2min) to remove the oxide layer. The width of the free-standing part can be controlled by the time of the TMAH etch (typically 1-3 hours). This process allows the preparation of more "fragile" structures, like large free-standing patterns, very long suspended nanotubes, or lithographically defined metal objects suspended on carbon nanotubes. The TMAH etch step is monitored with an optical microscope, and stopped when the free-standing part has reached a sufficient width.

3. Some of the samples were prepared on a GaAs substrate. These are coated with a protective resist (e.g. S1805 photoresist) on top of the metal structure. Etching is done in a mixture of water, citric acid and H_2O_2 at room temperature. A mixture of monohydrated citric acid with water (1:2) is prepared. To 1ml of this mixture, 150μl of H_2O_2 is added just before usage. This etching mixture is not stable, and may have to be replaced during the etching process (after a few hours). The process is monitored with an optical microscope, and stopped if the free-standing part is sufficiently wide. The resist is then removed in methylpyrrolidon and aceton (each for several hours at 55°C). This process allows the preparation of the most fragile structures, e.g. the largest objects suspended on individual SWNTs.

The etching is followed by transferring the sample into water, then into isopropanol, and finally acetone. A specially designed sample holder prevents the edge of the sample from drying. Finally, a critical point drying step with carbon dioxide is carried out. The substrates are small enough to be glued into conventional TEM rings (Fig. 3.6).
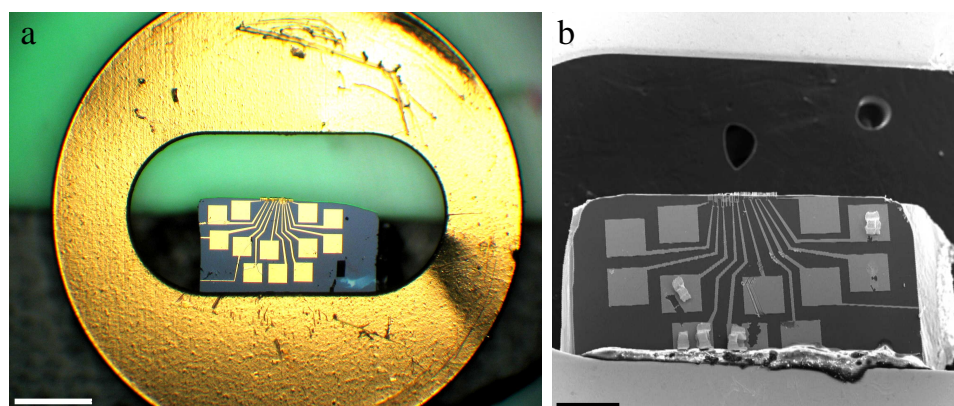
Figure 3.6: A substrate with a lithographically prepared structure glued into a conventional 3.05mm TEM ring. (a) optical microscope image and (b) low-magnification SEM image. There is just enough space for bond pads. Scale bar is 0.5mm in (a) and 0.2mm in (b).

3.2.4   TEM samples

As a result of this procedure, we obtain well-defined nanotube samples with nano-tubes nearly orthogonal to the beam. In low-density samples (Fig. 3.4d), approxi-mately 50% of the nanotubes are individual and well stretched between the contacts for a diffraction analysis. In higher-density samples (Fig. 3.4c), bundling occurs more frequently, and curved free-standing bundles appear. Individual tubes appear to be stretched by van der Waals attraction towards the contacts. Especially if they are not ending orthogonal to the contact, they curve towards a parallel alignment with the contact edge. Similarly, stretching is observed in small bundles (which are most likely formed after etching, when the tubes are free to move). An example is shown in Fig. 3.7.

We point out that carbon nanotubes, grown by CVD directly on a bulk sub-strate, can not usually be investigated by TEM and electron diffraction. They become accessible only due to our sample preparation procedure. This permits a quality control of CVD grown nanotubes, and provides information not avail-able from AFM or SEM investigations about bundling, precise diameters, number of shells, and amorphous carbon coating from TEM, and index distribution from diffraction analysis.
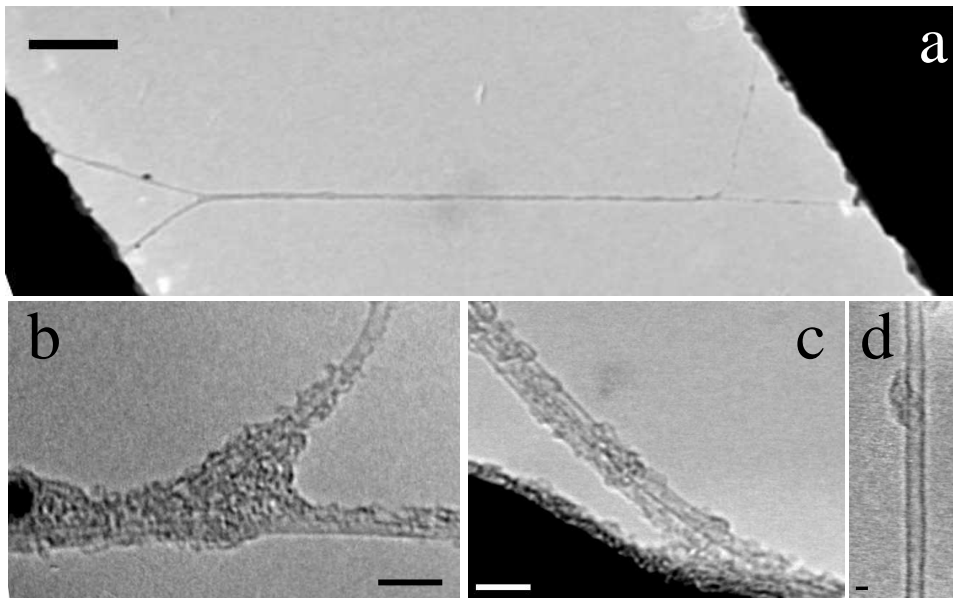
Figure 3.7: (a) Stretching of a small bundle by coalescence of the two nanotubes. We often observe small bundles splitting near the contact structure. These nanotubes were most likely separated before the etching process, but close together. They are fixed at the contacts, but the central part is free to move after etching. Due to van der Waals attraction the central sections have formed a bundle. As a result, the tube sections are straightened. (b) is a close-up on the right splitting point in (a). (c) shows a nanotube end (a bundle in this case) close to the contact. Tubes often appear curved just at the ends, suggesting that they are stretched by an attractive force towards the contacts. Most of the amorphous carbon is deposited during the TEM analysis: (d) shows a nanotube section after quickly zooming in to a high magnification. Scale bars are 100nm (a), 5nm (b+c) and 1nm (d).

Chapter 4

Transmission electron microscopy and electron diffraction

Transmission electron microscopy (TEM) and Electron Diffraction (ED) of individual carbon nanotubes is the one aspect of this work which is an essential part of all experiments. It is the combination with the electron microscopic analysis that allows us a better understanding of the devices we investigate. In the case of carbon nanotubes, TEM provides crucial information about the diameter and filling of a nanotube, or whether we are dealing with a bundle or a single tube.

From the diffraction analysis, it is possible to derive the exact structure of an individual carbon nanotube. The single-walled nanotube sections used for electron diffraction experiments in a transmission electron microscope contain only a small number of identical atoms that interact weakly with the electron beam. Therefore the diffraction patterns can be easily understood and simulated by simple approximations. For the same reasons, obtaining a diffraction pattern is an experimental challenge. Both the simulation of diffraction patterns, and diffraction experiments at acceleration voltages below the knock-on damage threshold are described. The latter is important for non-destructive determination of the nanotube structure, required for electron diffraction experiments in combination with other single-tube measurements on the same nanotube.

Other techniques for identifying the structural indices are atomic-resolution TEM imaging [7, 8, 9], Raman spectroscopy [28, 29], fluorescence spectroscopy [30, 31, 32], and scanning tunnelling microscopy and spectroscopy (STM/STS) [3, 4, 5, 6]. Electron diffraction and high-resolution images can be directly related to a pair of carbon nanotube structural indices (n,m), while spectroscopic techniques rely on a modelization of electronic and vibrational properties of carbon nanotubes. A quantitative analysis of the index distribution is complicated by a different response for different nanotubes both in Raman [33] and fluorescence spectroscopy. Further, fluorescence spectroscopy detects only semiconducting nanotubes.

In section 4.1 I will briefly describe the electron microscope. An important

aspect is then the interpretation of high-resolution images and diffraction patterns of carbon nanotubes. This requires understanding the interaction of the electron wave with the sample (Section 4.2) and the image formation due to the evolution of the wave function in the imaging system (4.3). Some example images are shown in this chapter, while most electron microscopic results will be presented in following chapters where appropriate in combination with other experiments on the same nanotube.

For the simulated diffraction and high-resolution images, I have written a computer program which produces the nanotube structure for given indices, and then calculates the interaction of the electron wave with the tube, and the image formation, using the principles and equations given in this chapter.

We use non-relativistic quantum mechanics with relativistically corrected values for the electron mass and wavelength. It has been shown that electron microscopic problems are well described in this way [34, 35, 36]. The crystallographic sign convention is used, where a plane wave has the form $e^{-i\mathbf{kr}}$.

4.1   The transmission electron microscope

Transmission electron microscopy has become a highly versatile tool for the investigation of materials down to the atomic scale. In today's transmission electron microscopes, a wide range of imaging techniques and contrast mechanisms is used. In this work, high-resolution bright field imaging and nanoarea electron diffraction is mostly employed and will be explained in this chapter.

Figure 4.1 shows ray diagrams for these two modes of operation. For bright-field imaging, the lenses are adjusted so that an image of the sample on the screen, CCD camera, or film is obtained. To be precise, the imaging system must be slightly defocused to produce contrast from a phase object - so in fact a sharp image of the electron wave slightly above or below the sample (few tens of nm) is obtained on the detector. This will be explained in section 4.3. For diffraction analysis, the projector lenses are focused on the back focal plane of the objective lens. The image produced in this way is equivalent to the intensity in the far-field behind the sample, at a distance given as *camera length* (typically 0.3 to 1.5m).

A major obstacle for TEM analysis of any specimen is the proper sample preparation for the desired analysis. As the name implies, TEM requires that the *transmitted* electrons can reach the detector. It is a major achievement of this work to prepare samples of individual single-walled carbon nanotubes in such way that investigations in a transmission electron microscope can be combined with transport, Raman or AFM investigations on the exact same object, with the "object" being a single molecule on which a TEM and especially diffraction analysis is in itself not trivial.

In this work, a Philips CM200 microscope operated at 120kV was used to obtain high-resolution images, and a Zeiss 912Ω operated at 60kV was used to obtain diffraction patterns of individual carbon nanotubes. Due to the sample structure,
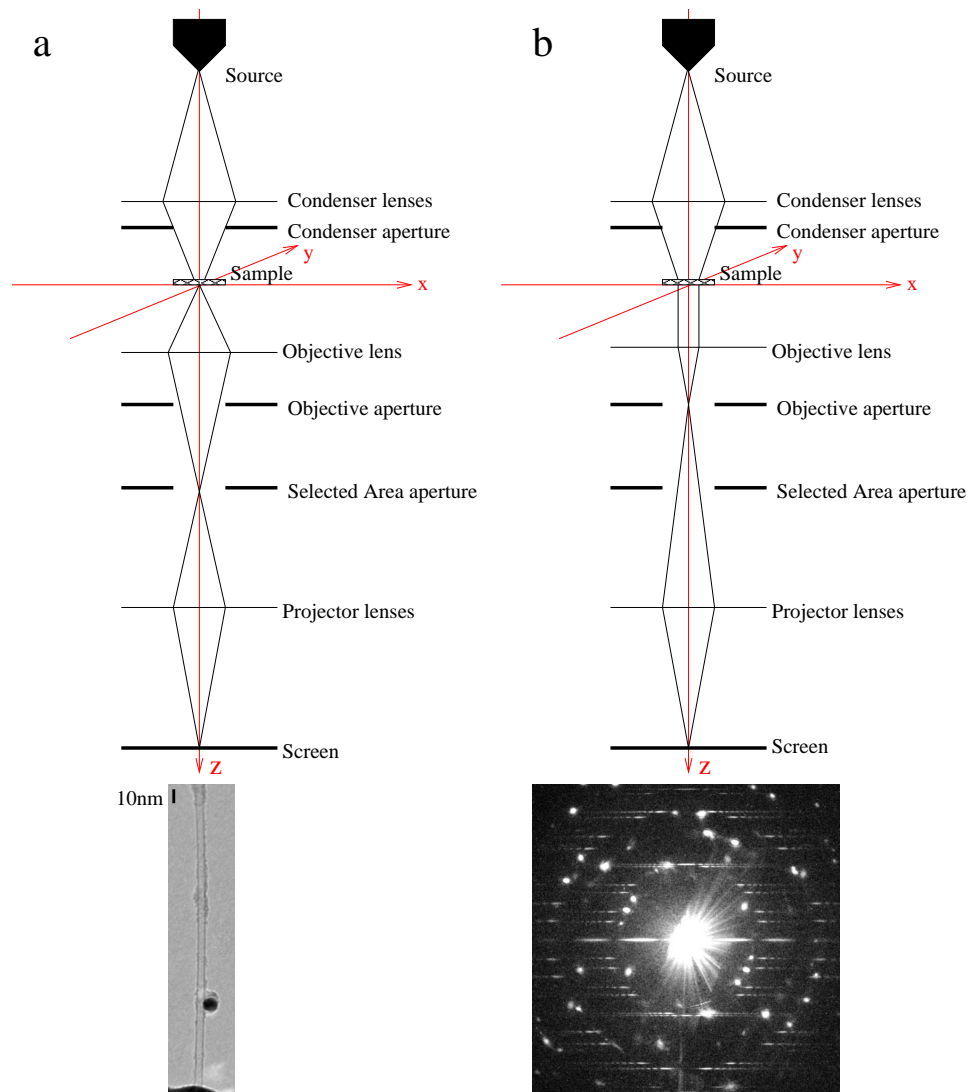
Figure 4.1: Simplified ray diagram of a transmission electron microscope, showing operation in bright-field imaging mode (a) and electron diffraction mode (b). Also indicated is the coordinate system (x,y,z) used in the following sections of this chapter.

a specific carbon nanotube can be easily found again and thus be analysed in both microscopes. Not shown in the ray diagram in Figure 4.1 is the energy filter which is available in the Zeiss 912Ω. It is used to reduce the diffuse background from inelastically scattered electrons in the diffraction experiments. The illuminated region in the diffraction experiment is limited to the sample area of interest (a section of the nanotube) using the condenser aperture. In this way, a structural analysis by diffraction of a region as small as 130nm in diameter is possible, providing, as I will show, without ambiguity the lattice structure of the nanotube segment.

4.2   Interaction of the electron wave with the specimen

This section deals with the simulation of high-resolution TEM images and electron diffraction patterns. Two different ways to calculate the diffraction pattern of a SWNT are presented. The real-space path summation approach is computationally more expensive but easy to understand and implement. It produces the correct peak positions, but not the right intensities. Our determination of the nanotube structure only depends on the position of the diffraction peaks. The alternative is computing the Fourier transform of the projected atomic potentials. This is the standard approach for thin objects that do not require multi-slice algorithms. However, peak positions deviate slightly from the correct values because the curvature of the Ewald sphere is not taken into account. The projected atomic potentials are also the basis for simulating high-resolution TEM images. Therefore, the simulation of diffraction and high-resolution images is not strictly separated in the description.

4.2.1   The Born approximation

We consider the time-independent Schrödinger equation for an electron wave in the specimen

$$\left[-\frac{\hbar^2}{2m}\nabla^2 - eV(\mathbf{r}) \right] \Psi(\mathbf{r}) = E\Psi(\mathbf{r}) \tag{4.1}$$

where the interaction with the sample is described by the electrostatic potential $V(\mathbf{r})$ inside the specimen. Using the time-independent Schrödinger equation is valid as long as we exclude inelastic scattering. We aim to find solutions with an electron energy $E = eU$, where U is the acceleration voltage. Equation 4.1 can be rewritten as

$$\nabla^2\Psi(\mathbf{r}) + \frac{2m}{\hbar^2}\left[E + eV(\mathbf{r}) \right] \Psi(\mathbf{r}) = 0 \tag{4.2}$$

For vanishing potential $V(\mathbf{r}) \equiv 0$, plane waves are solutions to 4.2. In particular, the incident wave

$$\Psi_0(\mathbf{r}) = C_0 \cdot \exp(-i\mathbf{k_0}\mathbf{r}) \tag{4.3}$$

is a solution outside the sample. Also, spherical waves $\Psi(\mathbf{r}) = |\mathbf{r}|^{-1} \exp(-i\mathbf{kr})$ are solutions. The integral form of the wave equation,

$$\Psi(\mathbf{r}) = \Psi_0(\mathbf{r}) + \frac{me}{2\pi\hbar^2} \int \frac{\exp(-i\mathbf{k}(\mathbf{r}-\mathbf{r}'))}{|\mathbf{r}-\mathbf{r}'|} V(\mathbf{r}')\Psi(\mathbf{r}')d^3r' \qquad (4.4)$$

(with $|k| = \sqrt{\frac{2meU}{\hbar^2}}$) is difficult to solve because $\Psi(\mathbf{r})$ appears within the integral. It can be interpreted in the way that spherical waves are added to the incident wave from each point of the specimen.

In the Born approximation, the wave function $\Psi(\mathbf{r})$ is approximated by the incident wave $\Psi_0(\mathbf{r})$. It assumes that the modification by the object is small, so that

$$\Psi(\mathbf{r}) = \Psi_0(\mathbf{r}) + \Psi_1(\mathbf{r}) \qquad (4.5)$$

and we obtain

$$\Psi_1(\mathbf{r}) = \frac{me}{2\pi\hbar^2} \int \frac{\exp(-i\mathbf{k}(\mathbf{r}-\mathbf{r}'))}{|\mathbf{r}-\mathbf{r}'|} V(\mathbf{r}')\Psi_0(\mathbf{r}')d^3r' . \qquad (4.6)$$

The second approximation would be $\Psi(\mathbf{r}) = \Psi_0(\mathbf{r}) + \Psi_1(\mathbf{r}) + \Psi_2(\mathbf{r})$, and so on. The first Born approximation is valid for a weakly scattering object. For an observation at a large distance $\mathbf{R}$ from the object we obtain:

$$\Psi_1(\mathbf{R}) = \frac{me}{2\pi\hbar^2} \cdot \frac{\exp(-i\mathbf{kR})}{|\mathbf{R}|} \int V(\mathbf{r}) \exp(i(\mathbf{k}-\mathbf{k_0})\mathbf{r}')d^3r' \qquad (4.7)$$

Equation 4.7 shows the important result that, in the 1st Born approximation, the scattered wave is the Fourier transform of the scattering potential. The difference between the incident wave and the scattered wave is

$$\mathbf{q} = \mathbf{k} - \mathbf{k_0} \qquad (4.8)$$

and the momentum is conserved for elastic scattering so that:

$$|\mathbf{k}| = |\mathbf{k_0}| \qquad (4.9)$$

Thus, the points in reciprocal space observed in a diffraction experiment fall on a sphere, called Ewald sphere, described by (4.8) and (4.9). Since the momentum transfer in an electron diffraction experiment is small so that $|\mathbf{q}| \ll |\mathbf{k_0}|$, the section of the Ewald sphere observed in such an experiment can be approximated as a plane.

In Figure 4.2 the three-dimensional Fourier transformation of a carbon nanotube was calculated, and a planar cut corresponding to an observable section of the Ewald sphere is shown. Since the nanotube is a periodic one-dimensional structure, the intensity in reciprocal space is cumulated on discs orthogonal to the tube axis. The spacing of these discs correspond to the periodicities along the tube
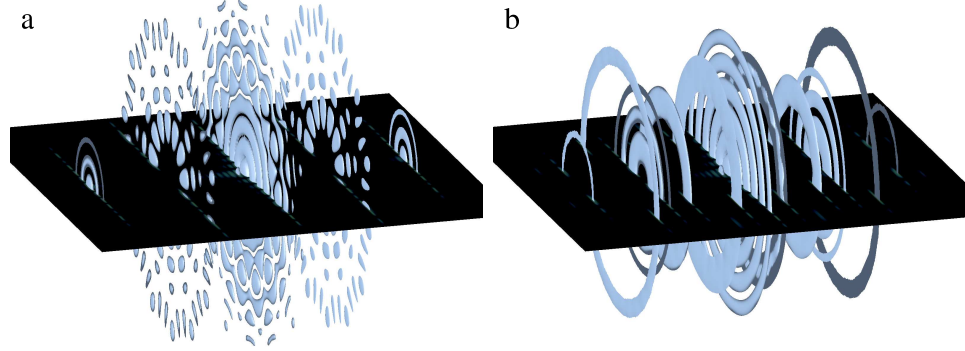
Figure 4.2: Three-dimensional Fourier transformation of a (7,7) nanotube (a) and an (8,3) nanotube (b). An isosurface is drawn around the higher intensity volume elements, shown in a perspective view. For a bulk crystal, this image would show the reciprocal lattice points. But since we have a one-dimensional structure, we obtain features that are extended in two dimensions: The diffraction intensities are cumulated on discs orthogonal to the tube axis. The planar section corresponds to the section of the Ewald sphere that would be observed in an electron diffraction experiment with normal incidence on the tube. For the (7,7) nanotube, a discrete 14-fold rotational symmetry around the tube axis is present in the Fourier transform.

axis, while the radial intensity distribution is determined by the tube diameter. The higher-symmetry armchair and zigzag nanotubes exhibit a discrete rotational symmetry, which is also present in the Fourier transform. Therefore, the diffraction pattern would change if the tube is rotated around its axis. This is not the case for chiral tubes.

4.2.2   Projected potential

In the case of small momentum transfer $|\mathbf{q}| \ll |\mathbf{k_0}|$, we can approximate the observed section of the Ewald sphere by a planar section. In the 1st Born approximation, we thus observe a planar section through the Fourier transform of the potential $V(\mathbf{r})$. We choose the coordinate system so that the incident wave is along z (with x and y orthogonal) to it. The corresponding coordinates in reciprocal space are q_x, q_y and q_z. Given the planar approximation for the Ewald sphere, it is sufficient to evaluate the Fourier transform (4.7) for $q_z = 0$. This corresponds to just the D.C. component of the Fourier transform in the z-direction. We rewrite (4.7) with $\mathbf{q} = \mathbf{k} - \mathbf{k_0}$ for $q_z = 0$ as:

$$\Psi_1(\mathbf{q}) = \text{const.} \cdot \int dx dy \exp(i(xq_x + yq_y)) \cdot \int dz V(x,y,z) \qquad (4.10)$$

We immediately see in (4.10) that our scattered amplitude is the 2D-Fourier transformation of the *projection* along z of the potential $V(\mathbf{r})$: The projection is

calculated as $\int dz V(x, y, z)$, and the remainder of (4.10) is a 2D Fourier transform with respect to x and y.

With only the first Born approximation and the planar approximation to the Ewald sphere we have directly arrived at the scattering amplitude as 2D-Fourier transform of the projected atomic potential. We note that it is more common to consider the projected potential via the object transfer function [37]

$$T(x, y) = \exp(-i\frac{ek_0}{2E} \int dz V(x, y, z)) \tag{4.11}$$

which describes the phase shift introduced by the object in the exit plane wave function. We will derive this expression later, since we need it for simulating high-resolution images.

4.2.3 Path summation approach

We consider an electron propagating from $(\mathbf{r_0}, t_0)$ to $(\mathbf{r_1}, t_1)$ through empty space, or through an object described by the electrostatic potential $V(\mathbf{r})$. In the most general case, the complex probability amplitude $\Psi(\mathbf{r_1}, t_1)$ is given by a summation over all paths starting from $\Psi(\mathbf{r_0}, t_0)$ [38, 39]:

$$\Psi(\mathbf{r_1}, t_1) = \Psi(\mathbf{r_0}, t_0) \cdot \sum_{\text{paths}} e^{-\frac{i}{\hbar}S} \tag{4.12}$$

S is the *action* along the path, given by

$$S = \int_0^T dt \cdot L(\mathbf{r}, \dot{\mathbf{r}}, t) \tag{4.13}$$

with the integration along the path from $(\mathbf{r_0}, 0)$ to $(\mathbf{r_1}, T)$. $L(\mathbf{r}, \dot{\mathbf{r}}, t)$ is the Lagrangian. Note that in order to obtain the crystallographic sign convention (where a plane wave is $e^{-i\mathbf{k}\mathbf{r}}$), we use $\sum_{\text{paths}} e^{-\frac{i}{\hbar}S}$, although this expression is more commonly found with the quantum mechanical sign convention ($\sum_{\text{paths}} e^{\frac{i}{\hbar}S}$, leading to a plane wave $e^{i\mathbf{k}\mathbf{r}}$).

For propagation in free space, the summation can be replaced by the term for the classical path [39], multiplied with a constant c_1' or c_1 (and $r = |\mathbf{r_1} - \mathbf{r_0}|$, $k = |\mathbf{k}|$):

$$\sum_{\text{paths}} e^{-\frac{i}{\hbar}S} = c_1' \cdot e^{-\frac{i}{\hbar}S_{cl.}} = c_1 \cdot \frac{1}{r} e^{-i(kr - \omega t)} \tag{4.14}$$

Using the classical action is exactly valid for a particle in any quadratic potential. As expected, we obtain the spherical wave for propagation in free space.

If we idealize the atoms in an object as point scatterers, we can divide the summation into the scattering events and piecewise propagation in free space. This is illustrated in Figure 4.3. We consider the propagation from the source to the
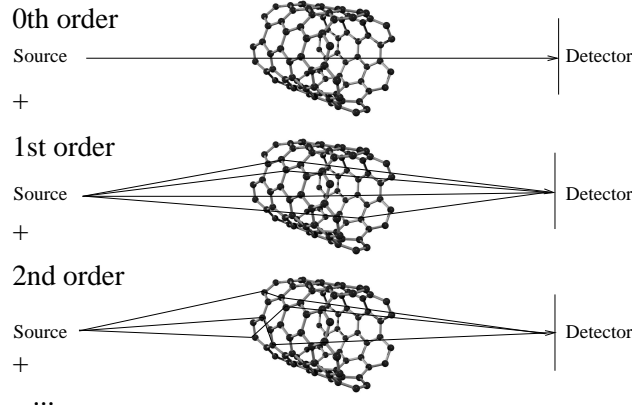
Figure 4.3: Contributions to the path summation, sorted by the number of interactions. It is equivalent to the 1st Born approximation to consider only 0th and 1st order contributions.

detector as the sum of the direct contribution, plus the paths including a single scattering event, two events and so on. The sum is thus written as:

$$
\sum_{\text{paths}} e^{-\frac{i}{\hbar}S} = c_1 \cdot \frac{1}{|r_{SD}|} e^{-ikr_{SD}}
$$

$$
+ \; c_1^2 \cdot \sum_n \frac{1}{|r_{SA_n}| \, |r_{A_nD}|} e^{-ikr_{SA_n}} f_n e^{-ikr_{A_nD}}
$$

$$
+ \; c_1^3 \cdot \sum_n \sum_m \; ...
\tag{4.15}
$$

Here, r_{SD} is the distance from the source to the detector, r_{SA_n} the distance from the source to atom n, and r_{A_nD} the distance from atom n to the detector. The summations are over all atoms of the object, f_n is the factor describing the scattering event at atom n, and the time dependence $\exp(i\omega t)$ as overall phase factor is omitted. For a set of identical atoms, the actual value of the scattering factor f_n is not important. The above summation represents Huygens principle of a spherical wave originating from every atom in the sample. Considering only the 0th and 1st order contributions, i.e. lines 1 and 2 in the above summation, is the equivalent of the 1st Born approximation for atoms idealized as point scatterers.

For objects containing a small number of atoms, the above summation can be carried out numerically. Given the small number of light (i.e., weakly scattering) atoms in an individual single-walled carbon nanotube, the 1st order approximation is reasonable. Assuming a detector at a large distance from the nanotube, diffraction patterns can be calculated numerically directly from 4.15. Figure 4.4 shows an example of such a diffraction pattern calculated for a (16,5) nanotube. Although reciprocal-space approaches for image simulation (shown below) are usually more
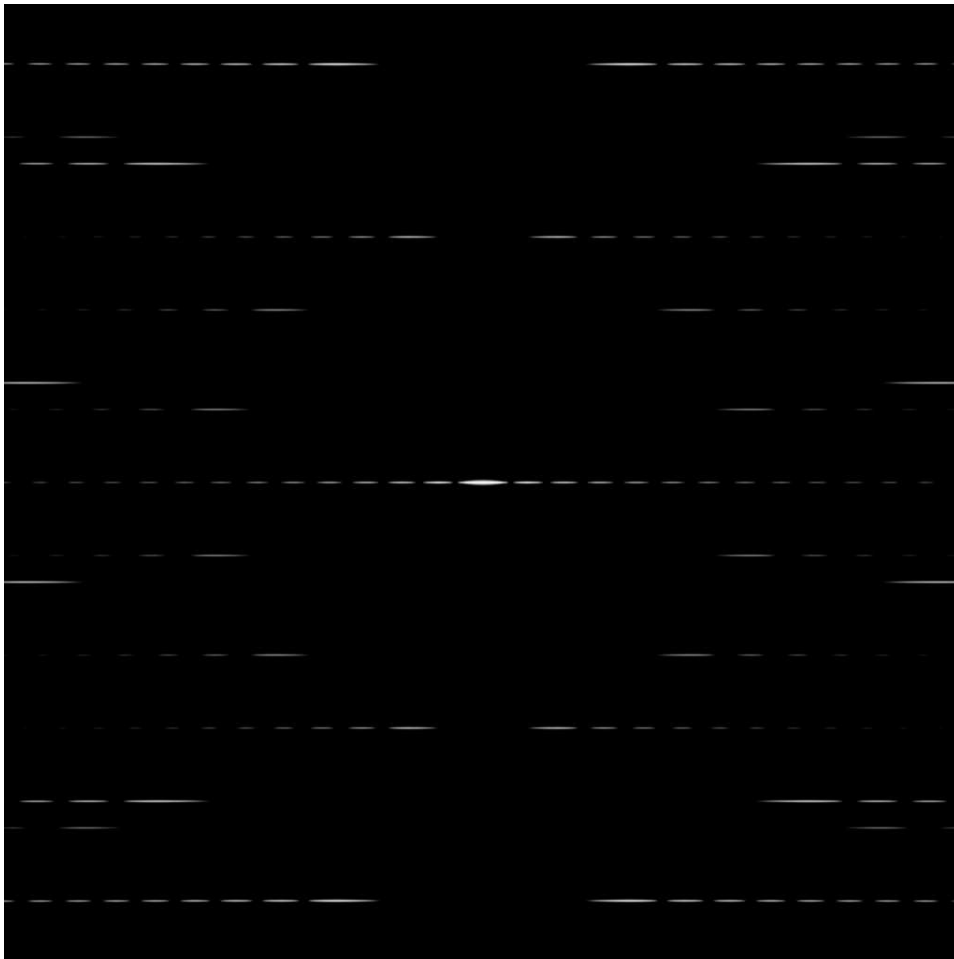
Figure 4.4: Diffraction pattern of a (16,05) carbon nanotube calculated by a path summation over all atoms of the nanotube. The summation has to be carried out for each point in the image. The vertical width of the peaks is determined by the length of the simulated nanotube.

efficient in terms of required computing time, the real-space summation can conveniently be carried out on a standard PC due to the small number of atoms in a carbon nanotube. A 50 nm long simulated nanotube section is sufficient for calculating a high-quality diffraction image.

4.2.4   Object transfer function in the phase object approximation

We will now derive an expression for the exit plane wave function for a thin and weakly scattering sample. We reconsider the propagation in free space,

$$\sum_{\text{paths}} e^{-\frac{i}{\hbar}S} = c_1' \cdot e^{-\frac{i}{\hbar}S_{cl.}} = c_1 \frac{1}{r} \cdot e^{-i(kr-\omega t)} \tag{4.16}$$

where the summation is replaced by the contribution of only the classical path. We now make the following *approximation*: We consider the *phase shift* introduced by the potential $V(r)$, but, as for the free particle, only *along the classical path*. This is valid if the deviation of the electron from the classical path is sufficiently small. For the validity of this approximation, such deviations must be smaller than the desired resolution at the exit plane of the sample.

In presence of the potential $V(\mathbf{r})$ of the object, the wave number is:

$$k = \sqrt{\frac{2m(E + eV(\mathbf{r}))}{\hbar^2}} \tag{4.17}$$

Note that e is defined as a positive number, and the charge of the electron would be $-e$. If $|eV(\mathbf{r})| \ll E$, we can approximate (4.17) as

$$k \approx \sqrt{\frac{2mE}{\hbar^2}} \cdot \left(1 + \frac{eV(\mathbf{r})}{2E}\right) = k_0 \cdot \left(1 + \frac{eV(\mathbf{r})}{2E}\right) \tag{4.18}$$

with k_0 being the vacuum wave number. We define:

$$\delta(\mathbf{r}) = \frac{eV(\mathbf{r})}{2E} \tag{4.19}$$

An electron travelling in a constant potential V from $\mathbf{r_0}$ to $\mathbf{r_1}$ over a distance $r = |\mathbf{r}| = |\mathbf{r_1} - \mathbf{r_0}|$ accumulates a phase shift in the complex wave amplitude $\psi(\mathbf{r_1})$ according to

$$\psi(\mathbf{r_1}) = \psi(\mathbf{r_0})\frac{c}{r}e^{-i(k_0(1+\delta)r)} = \psi(\mathbf{r_0}) \cdot \frac{c}{r}e^{-i(k_0 r)} \cdot e^{-i\delta k_0 r} \tag{4.20}$$

We introduce the transmission function $T(\mathbf{r_1})$ as the quotient of the amplitude for the transmitted wave (interacting with the object, equation 4.20) to the amplitude for the free space (if the object were not there, equation 4.16), as:

$$T(\mathbf{r_1}) := \frac{\psi(\mathbf{r_1})}{\psi_{\text{free}}(\mathbf{r_1})} = e^{-i\delta k_0 r} \tag{4.21}$$

For an inhomogeneous object, $\delta(\mathbf{r})$ is a local property of the object. The total phase shift accumulated along the classical path is given by the integral over δ, integrated along the straight line from $\mathbf{r_0}$ to $\mathbf{r_1}$:

$$T(\mathbf{r_1}) = \exp(-ik_0 \int_{\mathbf{r_0}}^{\mathbf{r_1}} d\mathbf{r}' \delta(\mathbf{r}')) \tag{4.22}$$

Generally, T is the effect of the object on the amplitude in free space:

$$\psi = T_{\text{obj}} \cdot \psi_{\text{free}} \tag{4.23}$$

We can rewrite (4.22) as:

$$T(\mathbf{r_1}) = \exp(-i\sigma \int_{\mathbf{r_0}}^{\mathbf{r_1}} d\mathbf{r}' V(\mathbf{r}')) \tag{4.24}$$

$$\sigma = \frac{ek_0}{2E} \tag{4.25}$$

The above approximation, leading to equation (4.24), is known as the *phase object approximation* (POA): It results in a phase shift proportional to the projected potential along the classical paths of the electrons. It neglects the lateral spread of the wave function. It is valid only for very thin objects and/or high energies. Individual single-walled carbon nanotubes are one of the few systems where this approach is a good approximation.

The concept of a transfer function for describing the electron-sample interaction breaks down for larger objects. However, a larger object can be described by a series of thin slices, and for each slice the transmitted electron wave can be calculated as described above. Lateral spread is then included in the propagation *between* the slices. This leads to the multi-slice approach, which is widely used for simulating electron micrographs of thicker samples.

The POA (4.24) includes multiple scattering, while the 1st Born approximation (4.10) does not. However in the limit of a *small* phase shift in (4.24), the 1st Born approximation is satisfied. This is called *weak phase object approximation* (WPOA). It leads to equivalent expressions for the diffraction intensities in the Fourier transform of (4.24) compared to (4.10).

In analogy to the phase shift, absorption can be included in the object transmission function. The absorption is described by a local property $\beta(\mathbf{r})$ of the object, and the absorption is again calculated as a projection along the classical path of the electron. The total transmission function including absorption is then

$$T(\mathbf{r_1}, \mathbf{r_0}) = e^{-ik_0 \int_{\mathbf{r_0}}^{\mathbf{r_1}} d\mathbf{r}' \delta(\mathbf{r}')} \cdot e^{-k \int_{\mathbf{r_0}}^{\mathbf{r_1}} d\mathbf{r}' \beta(\mathbf{r}')} \tag{4.26}$$

As several mechanisms contribute to the absorption, it is not as straightforward to calculate as the phase shift. For thin samples, most of the absorption is due to electrons scattered in such a way that they no longer contribute to the image: This includes various inelastic scattering mechanisms, or elastic scattering to high

angles. Thus, the effective absorption depends on settings of the microscope (e.g. objective aperture, energy filter) that determine which electrons contribute to the final image. Since the images and diffraction patterns of light objects are dominated by phase contrast, we neglect the absorption.

To actually calculate a simulated image of a carbon nanotube from the phase shifts, we will now consider the actual shape of the scattering potential $V(\mathbf{r})$ for use in equation 4.24.

4.2.5   Scattering potential

For an isolated atom, the potential $V(\mathbf{r})$ has spherical symmetry. We have seen in the Born approximation (eq. (4.7)) that the far-field scattered amplitude is proportional to the Fourier transform of the potential $V(\mathbf{r})$. The electronic scattering amplitude is commonly defined as the Fourier transform of the atomic potential [40]:

$$f^{(e)}(\mathbf{s}) = \frac{m_0 e}{2\pi\hbar^2} \int d^3 r\, V(\mathbf{r}) e^{-i\mathbf{q}\mathbf{r}} \qquad (4.27)$$

where $\mathbf{q} = 4\pi\mathbf{s}$, $s = |\mathbf{s}| = sin(\theta)/\lambda$, and θ is half of the scattering angle. For the spherically symmetric potential, it can be expressed as:

$$f^{(e)}(s) = \frac{2m_0 e}{\hbar^2} \int_0^\infty r^2 dr V(r) \frac{sin(4\pi s r)}{(4\pi s r)} dr \qquad (4.28)$$

A widely used analytical approximation to $f^{(e)}(s)$ is the approximation to a sum of N Gaussians:

$$f^{(e)}(s) = \sum_{i=1}^N a_i \exp(-b_i s^2) \qquad (4.29)$$

Tabularized values for a_i and b_i can be found e.g. in [41], where they are calculated from relativistic Hartree-Fock calculations and fitted to a sum of $N = 4$ Gaussians. In a realistic situation the atoms oscillate about their equilibrium position. This is taken into account to a good approximation by an additional spread function, the Debye-Waller Factor. It describes the *time-averaged* effective atomic potential, which is in reciprocal space simply expressed by the multiplication with e^{-Bs^2}, where $B = 4\pi^2 a^2$ and a the root mean square deviation of the atom from its lattice site. The resulting scattering amplitude is then

$$f^{(e)}(s) = \exp(-Bs^2) \cdot \sum_{i=1}^N a_i \exp(-b_i s^2) \qquad (4.30)$$

The electrostatic atomic potential can now be obtained by inverse Fourier transformation of the scattering amplitude:

$$V(\mathbf{r}) = \frac{2\pi\hbar^2}{m_0 e} \frac{1}{(2\pi)^3} \int f^{(e)}(\mathbf{s}) \exp(i\mathbf{qr}) d^3q \tag{4.31}$$

For the sum of Gaussians in (4.30) the inverse Fourier transformation (4.31) can be done analytically, resulting in another sum of Gaussians in real space for the electrostatic atomic potential of an atom at $\mathbf{r} = 0$:

$$V(r) = \frac{2\pi\hbar^2}{m_0 e} \sum_{i=1}^{N} a_i \left(\frac{4\pi}{b_i + B}\right)^{\frac{3}{2}} \exp\left(-\frac{4\pi^2 r^2}{b_i + B}\right) \tag{4.32}$$

For an object composed of many atoms, we approximate the total potential as the sum of the individual atomic potentials:

$$V_{total}(\mathbf{r}) = \sum_{n} V_n(\mathbf{r} - \mathbf{R_n}) \tag{4.33}$$

where atom n is at position $\mathbf{R_n}$. This approximation neglects the overlap and the changes in the electronic structure due to bonds in the solid.

4.2.6 Projected atomic potentials

For evaluating the exit plane wave function of the sample, we have to evaluate in equation (4.24) the *projection* of the atomic potential (4.32). We have $\mathbf{r} = (x, y, z)$ and we choose the frame of reference so that the propagation is along the direction z with (x, y) as constant. We obtain

$$
\begin{aligned}
\int_{\mathbf{r_0}}^{\mathbf{r_1}} d\mathbf{r}' V(\mathbf{r}') &= \int_{-\infty}^{\infty} dz V(x, y, z) \\
&= \frac{2\pi\hbar^2}{m_0 e} \sum_{i=1}^{N} a_i \left(\frac{4\pi}{b_i + B}\right)^{\frac{3}{2}} \int_{-\infty}^{\infty} dz \exp\left(-\frac{4\pi^2(x^2 + y^2 + z^2)}{b_i + B}\right) \\
&= \frac{2\pi\hbar^2}{m_0 e} \sum_{i=1}^{N} a_i \frac{4\pi}{b_i + B} \exp\left(-\frac{4\pi^2(x^2 + y^2)}{b_i + B}\right) \tag{4.34}
\end{aligned}
$$

This is the projection along z of the atomic potential for an atom at $(x, y) = (0, 0)$. The resulting transmission function is found by substituting (4.34) into (4.24):

$$T(x, y) = \exp\left[-i\frac{k_0 4\pi^2 \hbar^2}{E m_0} \sum_{i=1}^{N} \frac{a_i}{b_i + B} \exp\left(-\frac{4\pi^2(x^2 + y^2)}{b_i + B}\right)\right] \tag{4.35}$$

The phase shift for a carbon nanotube, calculated from the projected potential using the above equation, is shown in Figure 4.5. It can be used for the exit plane wave function for simulating images as shown in the next section. Further, it is the
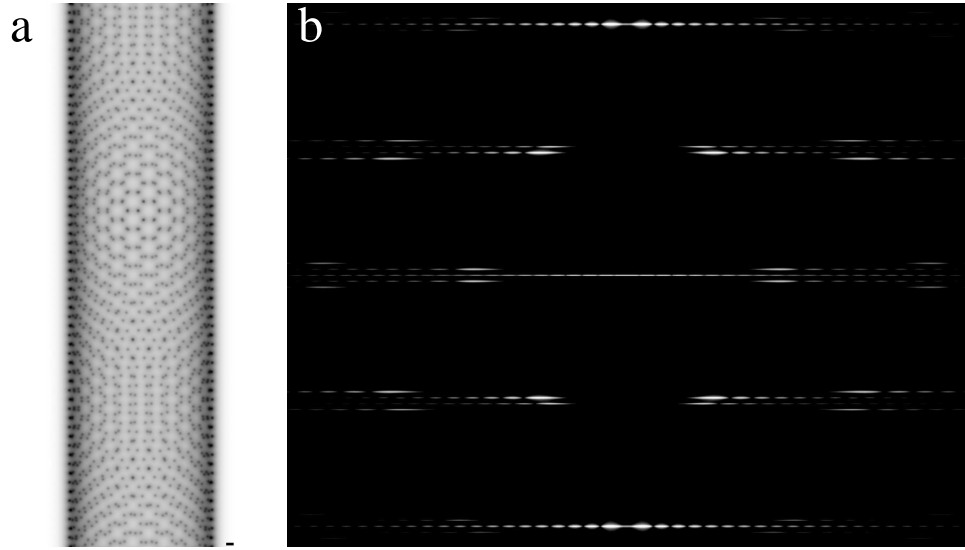
Figure 4.5: (a) Phase shift calculated from the projected potential of a (15,13) carbon nanotube for a Debye-waller factor $B = 0$ and an electron energy of 60keV. White corresponds to zero phase shift, while black corresponds to a phase shift of 0.44π. Scale bar is 1Å. (b) Fourier transformation of the exit plane wave function. Displayed is the square modulus, which corresponds to the intensities observed in a diffraction pattern.

Fourier transform of the exit plane wave function that is observed in a diffraction pattern. Computing diffraction patterns by a fast Fourier transformation of the exit plane wave function is much faster than the path summation calculation shown in section 4.2.3. However, it implies approximating a section of the Ewald sphere as a plane.

4.3   Image formation

4.3.1   Propagation

The evolution of the wavefunction for propagation through empty space can be calculated exactly. From the amplitude $\psi(x, y, z = 0)$ in the plane $z = 0$ behind the sample, it is possible to calculate $\psi(x, y, z)$ for arbitrary positions z downstream of the sample. In the above sections, we have calculated the propagation of the electron from the source through the sample to all points in the reference plane, resulting in the probability amplitude $\psi(x, y, z = 0)$. We now have to calculate the summation from all points in the reference plane to the arbitrary detector position (x, y, z):

$$\psi(x, y, z) = \int dx' dy' \psi(x', y', 0) \frac{c_1}{R} e^{-ikR} \qquad (4.36)$$

$$R = \sqrt{(x - x')^2 + (y - y')^2 + z^2}$$

The integration is over the reference plane at $z = 0$. The above expression is a convolution of the wave amplitude $\psi(x, y, 0)$ with the propagator $\frac{c_1}{R}e^{-ikR}$. It is therefore advantageous to express (4.36) in reciprocal space, so that the convolution becomes a simple multiplication. For this purpose we consider $\psi(x, y, z)$ as a 2D-Fourier transformation only with respect to x and y (while z is the direction of propagation) of a function $\phi(\rho, z)$. We use from now on $\mathbf{r} = (x, y)$ as the vector in the plane orthogonal to the direction of propagation z. The relation for the inverse 2D Fourier transformation is

$$\psi(x, y, z) = \int d^2\rho \exp(2\pi i \rho \mathbf{r})\phi(\rho, z) \tag{4.37}$$

where $\rho = (\rho_x, \rho_y)$ is the reciprocal vector in the plane orthogonal to the z-axis, corresponding to $\mathbf{r} = (x, y)$ in real space. Note that ψ is the *inverse* Fourier transform of ϕ. The propagation can now be written as a multiplication with the propagator $G(\rho, z)$:

$$\phi(\rho, z) = \phi(\rho, 0) \cdot G(\rho, z) \tag{4.38}$$

$$G(\rho, z) = \exp(-ikz(1 + \lambda^2\rho^2)^{\frac{1}{2}}) \tag{4.39}$$

If the spectrum vanishes for spatial frequencies $|\rho| \ll \frac{1}{\lambda}$, the propagation factor can be approximated by the *Fresnel propagator P*:

$$P(\rho, z) = \exp(-ikz)\exp(i\pi\lambda z\rho^2) \tag{4.40}$$

For the electron energies commonly used in transmission electron microscopy the relation $|\rho| \ll \frac{1}{\lambda}$ is usually fulfilled since the electron wavelengths are already much smaller than the smallest features, the interatomic distances. Thus, in reciprocal space, the propagation is a multiplication with the Fresnel propagation factor (4.40):

$$\phi(\rho, z) = \phi(\rho, 0) \cdot \exp(-ikz) \cdot \exp(i\pi\lambda z\rho^2) \tag{4.41}$$

The resulting wavefunction at distance z is

$$\psi(\mathbf{r}, z) = \int d^2\rho \exp(2\pi i \rho \mathbf{r})\phi(\rho, 0)\exp(-ikz)\exp(i\pi\lambda z\rho^2) \tag{4.42}$$

The intensity measured at a detector distance z is $I_z(x, y) = I_z(\mathbf{r}) = |\psi_z(\mathbf{r})|^2$. The resulting intensity is:
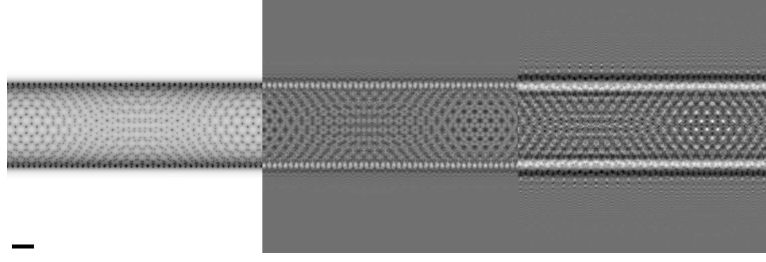
Figure 4.6: Projected atomic potentials of a (15,13) carbon nanotube at 120kV (left), and Intensities calculated 6nm and 18nm behind the nanotube. The Debye-Waller factor is $B = 0$. The maximum phase change in the projected potential corresponds to 0.34π. Scale bar is 5Å.

$$I(\mathbf{r}, z) = \left| \int d^2\rho \exp(2\pi i\rho r)\phi(\rho, 0) \exp(i\pi\lambda z\rho^2) \right|^2 \qquad (4.43)$$

With the calculated wavefunction at the exit plane of the sample as shown in the previous section we can now calculate the intensity at an arbitrary distance from the sample. Since the nanotube was approximated as a pure phase object (no absorption), no contrast is visible directly at the sample (for $z = 0$). Also in a real TEM image the nanotube is not visible if the focus is exactly on the tube (there is some contrast due to spherical aberration, as described below). Only by *defocusing* the imaging lenses it is possible to have a contrast from a pure phase object. The focus is typically several tens of nanometers away from the nanotube position for a high-resolution image.

While Figure 4.6 shows the intensity a few nm behind the sample, this is not the image we see in the TEM. The TEM image is affected by the spherical aberration, and the resolution is limited by the finite temporal and spatial coherence and by instrument instabilities.

4.3.2   Microscope specific transfer function

The spherical aberration and the resolution limits of the microscope are taken into account by a modification of the Fresnel propagator (4.40). The Fresnel propagator can be understood as the transfer function for empty space (i.e., also free of fields). For the imaging system in the electron microscope, the transfer function is approximated as:

$$\phi(\rho, z_{Det.}) = \phi(\rho, 0) \cdot \exp\left[i(\pi\lambda z\rho^2 + \frac{1}{2}\pi\lambda^3\rho^4 C_s) \right] \cdot [E_t(\rho) \cdot E_s(\rho) \cdot E_i(\rho) \cdot A(\rho)]^{\frac{1}{2}}$$

$$(4.44)$$

Here, $\phi(\rho, 0)$ is the complex wave amplitude at the exit plane of the sample. $\phi(\rho, z_{Det.})$ describes our image at the Detector: The absolute square after an inverse Fourier transform of $\phi(\rho, z_{Det.})$, rescaled by the appropriate magnification, is the image we obtain on the CCD camera, screen, or film. The distance z is now our defocus value, and C_s the spherical aberration coefficient. E_t and E_s are the envelope functions for the temporal and spatial coherence. Instrumental instabilities are summarized in the envelope function E_i, and the aperture function A describes the effect of the objective aperture. Equation (4.44) can readily be used to simulate high-resolution images.

The temporal envelope is determined by the energy spread of the incident beam $\Delta E / E_0$, current fluctuations in the objective lens $\Delta I / I_0$, and the chromatic aberration coefficient of the objective lens C_C [37]:

$$E_t(\rho) = \exp\left[-\frac{1}{16\ln 2}(\pi\lambda\rho^2\delta^2)^2\right] \tag{4.45}$$

where

$$\delta = C_C\left[(\frac{\Delta E}{E})^2 + (2\frac{\Delta I}{I})^2\right]^{-\frac{1}{2}}. \tag{4.46}$$

The spatial envelope is determined by the illumination angle α_0. This envelope accounts for the fact that the incident electron beam is not a plane wave, but a convergent beam modelled as an incoherent superposition of planar waves. It is given by [37]

$$E_s(\rho) = \exp\left[-\frac{1}{4\ln 2}(\pi\alpha_0(z\rho + C_s\lambda^2\rho^3))^2\right]. \tag{4.47}$$

The instrumental envelope summarizes the remaining instabilities (e.g. vibrations) in a Gaussian envelope

$$E_i = \exp(-\frac{\rho^2}{\rho_{max}^2}). \tag{4.48}$$

Finally, the objective aperture limits the spatial frequencies contributing to the final image. It is characterized by the cut-off frequency ρ_{max} and aperture center ρ_{ap}:

$$\begin{aligned} A(\rho) &= 1 \quad \text{for} \quad |\rho - \rho_{ap}| < \rho_{max} \\ &\quad\; 0 \quad \text{elsewhere} \end{aligned} \tag{4.49}$$

An objective aperture not centered on the primary beam ($\rho_{ap} \neq 0$) is used e.g. to describe dark-field imaging (although it is usually the primary beam which is tilted for this purpose, while the aperture remains on the optical axis of the microscope).
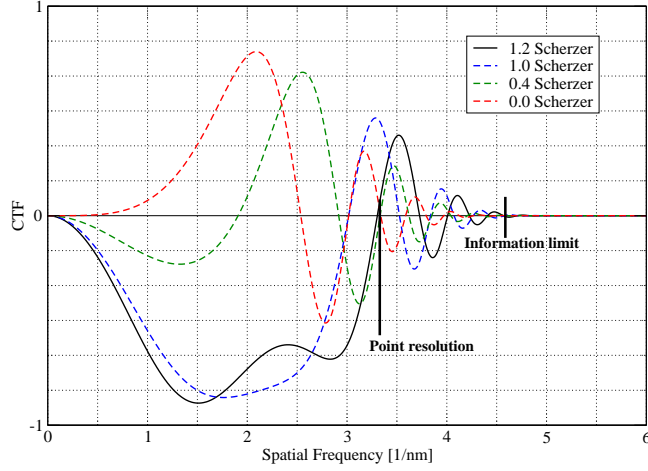
Figure 4.7: Contrast transfer function for different defocus values, for 120kV, $C_s = 1.3$mm and an illumination angle of 1mrad. 1.0 Scherzer defocus is -66nm. The point resolution is the first zero crossing of the CTF at a defocus value of 1.2 Scherzer (solid black line). For the other defocus values, the first zero crossing of the CTF occurs already at lower spatial frequencies. Minimum contrast is at 0.4 Scherzer (green), not at zero defocus. The information limit is given by the point where the CTF reaches zero.

For a pure phase object, we can derive the contrast obtained in the final image as a function of spatial frequency from equation (4.44): A phase grating with a periodicity $\frac{1}{\rho_0}$, described by

$$\phi(\rho, 0) = \frac{1}{2}(\delta(\rho - \rho_0) + \delta(\rho + \rho_0)) \tag{4.50}$$

produces a contrast proportional to

$$Q(\rho) = \sin(\pi \lambda z \rho^2 + \frac{1}{2}\pi \lambda^3 \rho^4 C_s) \cdot E_t(\rho) \cdot E_s(\rho) \cdot E_i(\rho) \cdot A(\rho) \tag{4.51}$$

$Q(\rho)$ is the *Contrast Transfer Function* (CTF) for a phase object. It is an important and widely used expression in high-resolution transmission electron microscopy. The *point resolution* and *information limit* of the microscope can be defined from this function.

The CTF oscillates between -1 and +1, damped by the envelopes. This implies that some spatial frequencies, where the CTF is zero, are missing in the final image. Obviously, the optimum CTF has the fewest zeroes. Scherzer [42] suggested an optimum defocus value of
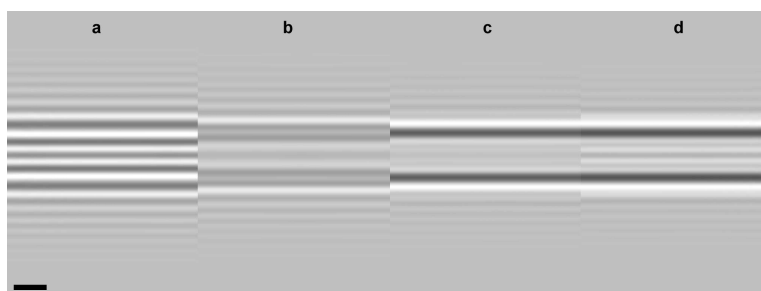
$$z_S = -(C_s \lambda)^{\frac{1}{2}} \tag{4.52}$$

Figure 4.8: High-resolution images simulated for a (12,10) nanotube at four different defocus values, for 120kV, $C_s = 1.3$mm and an illumination angle of 1mrad. Section (a) is for zero defocus, producing a reverse contrast ("white atoms"). Section (b) is at a defocus of 0.4 Scherzer (26nm), the minimum contrast condition. The nanotube walls are clearly visible as black lines at 1.0 (c) and 1.2 (d) Scherzer defocus (66 and 79nm). Scale bar is 1nm.

where the CTF has a broad maximum. The CTF is plotted for a several defocus values in Figure 4.7. At zero defocus, some contrast is already obtained only due to the spherical aberration. Minimum contrast is obtained at $z = 0.4z_S$. The optimum condition is $z = 1.2z_S$, a value also named *extended Scherzer defocus*, while $z = z_S$ is called "true" Scherzer defocus. The first zero-crossing of the CTF at the extended Scherzer defocus is defined as the *point resolution* of the microscope. Images can be directly interpreted up to the point resolution. The information limit is the point where the CTF reaches zero. If the information limit is higher than the point resolution, image simulations are needed to interpret features smaller than the point resolution.

In Figure 4.8, high-resolution images are simulated for different defocus values for a (12,10) carbon nanotube. It is important to note that the nanotube diameter can not simply be measured from the distance of the black lines. In this example, at 1.2 Scherzer defocus (Figure 4.8d), the distance between the minima of the black lines is 1.35nm, while the true diameter of this nanotube is 1.5nm. Therefore, comparison with image simulations can provide a better estimate of the nanotube diameter. However, it is difficult to determine the actual defocus value: The minimum contrast defocus can provide a reference, but again with limited precision since there is also not much contrast slightly above and below the minimum contrast.

High-resolution images of carbon nanotubes with very different diameters are shown in Figure 4.9. These, and most high-resolution images shown in this work, were obtained in a Philips CM200 transmission electron microscopes operated at 120kV.
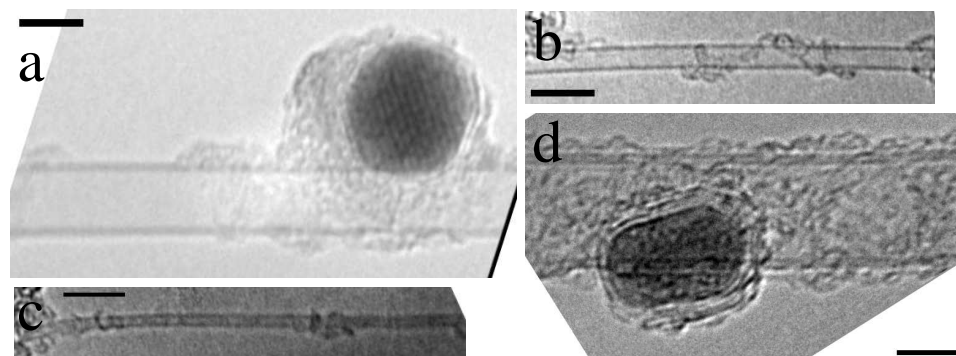
Figure 4.9: High-resolution TEM images of different nanotubes, with very different diameters, displayed at the same scale. CVD-grown SWNTs with an estimated diameter of 5.3nm (a), 1.7nm (b), and 0.9nm (c), and a DWNT with an outer diameter of 8.8nm (d). Inactive catalyst particles are stuck to the tubes in (a) and (d). All scale bars are 5nm.

4.4   Diffraction analysis

A diffraction pattern of a SWNT provides the full structural information about the nanotube molecule, apart from its handedness. The structure of the nanotube is defined by the nanotube indices (n,m). We recall that in the Born approximation (section 4.2.1) the diffraction pattern is a two-dimensional section from the Fourier transform of the nanotube structure. It can also be calculated by a path summation (section 4.2.3). The spherical section of the Ewald sphere is well approximated by a planar section. Given this approximation, we can compute the diffraction intensities also from a two-dimensional Fourier transform of the exit plane wave function (section 4.2.6). In this section I will give a qualitative interpretation of the diffraction peaks in dependence of the nanotube diameter and rolling angle, compare the calculation algorithms, and show examples of experimentally obtained single-tube diffraction images.

Detailed diffraction studies exist on multi-walled carbon nanotubes [43, 44, 12, 45] and bundles of single-walled carbon nanotubes [46, 47, 48, 11, 49, 50, 51, 52, 53, 54, 55]. Diffraction experiments on *individual* SWNTs are an experimental challenge also for the sample preparation because they require finding sufficiently long, straight sections of individual nanotubes (raw material is mostly bundled) that are stable throughout the exposure. Nanotubes with more than one shell are usually stiff enough to exhibit long, straight sections with standard sample preparation procedures. SWNTs, on the other hand, tend to curve, and to combine into bundles. A curved nanotube is not a periodic one-dimensional structure. Few examples of sharp diffraction patterns from SWNTs exist in the literature [1, 56, 57]. However with the sample preparation procedure shown in this work, long straight sections of individual SWNTs are easily obtained. We have developed a way to suspend nanotubes in a metal grid that provides long and straight tube sections. In
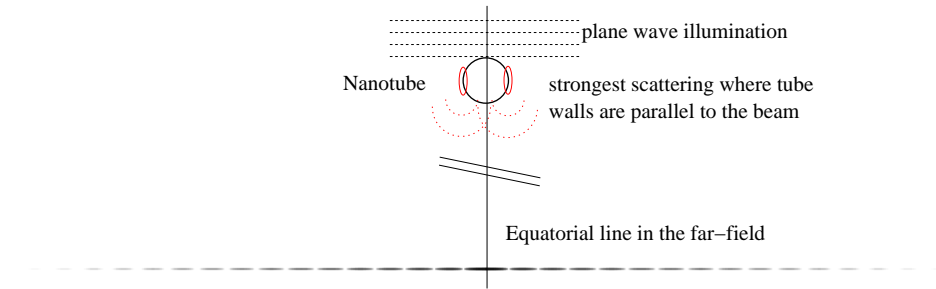
Figure 4.10: Qualitative analogy between the equatorial line in a nanotube diffraction pattern and a double slit interference pattern.

the resulting samples, tubes suitable for diffraction are easily found and reliably produce a diffraction pattern with a close to normal incidence. With the given conditions, more than 50% of the diffraction exposures result in a pattern that can be uniquely assigned to a nanotube structure. The "failed" exposures are attributed to curved or strongly vibrating tubes, or to objects other than the tube illuminated by the beam. Indices for more than 50 nanotubes were determined so far. It is a reliable procedure, which is a prerequisite for the combination with other experiments on the same tube.

4.4.1 Qualitative description of the diffraction pattern

The diffraction pattern of a single-walled carbon nanotube can be well separated into features that depend on the nanotube diameter, and others which depend on the rolling angle of the graphene sheet. The most prominent feature is the *equatorial line*, which is similar to a double-slit interference pattern (Figure 4.10). The periodicity of this line is related to the nanotube diameter.

From further peaks in the pattern we can determine the orientation of the (reciprocal) graphene hexagonal lattice. A simulated diffraction pattern for a (15,06) nanotube, and a part of the reciprocal graphene lattice, is shown in Figure 4.11.

The orientation of the graphene lattice, i.e. the rolling angle of the nanotube, can be calculated independent of the incidence angle from the relative distances of the peaks from the equatorial line. This measure is also independent of the scale (camera length) or a diffraction astigmatism. Thus, the rolling angle can be reliably and precisely measured with a precision of up to $0.1°$. Using e.g. the distances $d_1 - d_3$ in Figure 4.11, the rolling vector is [57]:

$$\alpha = \arctan\left(\frac{1}{\sqrt{3}} \cdot \frac{d_2 - d_1}{d_3}\right) = \arctan\left(\frac{1}{\sqrt{3}} \cdot \frac{2d_2 - d_3}{d3}\right) \tag{4.53}$$

The reason why the ratios of the peak distances remain constant even if the tube is not orthogonal to the beam is obvious if we recall that the diffraction intensities are lying on planar discs in reciprocal space. This is illustrated in Figure 4.12.
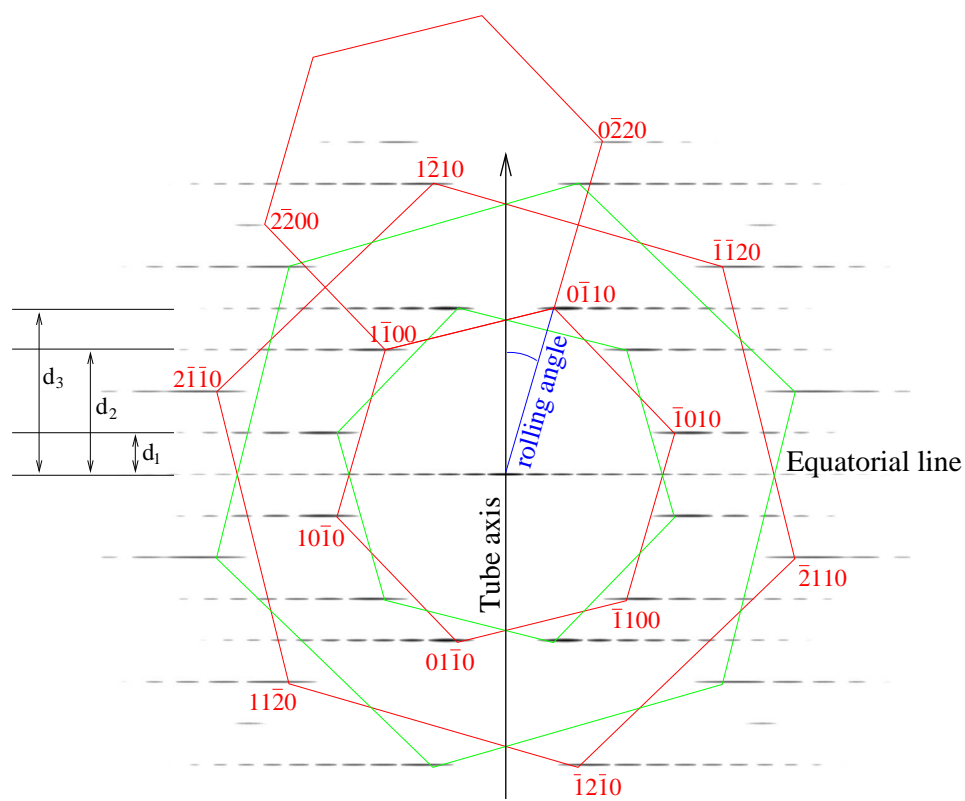
Figure 4.11: Orientation of the reciprocal graphene lattice in the SWNT diffraction pattern. Two sets of peaks that correspond to the top and bottom graphene layer in the nanotube are visible. The Miller-Bravais indices for one of the two hexagonal lattices are given. A rolling angle of $0°$ corresponds to a zig-zag nanotube, $30°$ represents an armchair tube. It is not recommended to measure the angle as indicated in the diagram, since the indicated angle is only true for an exactly normal incidence of the beam on the tube. Instead, the angle can be reliably calculated from the relative distances of the peaks to the equatorial line, indicated by d_1, d_2 and d_3. The streaked shape of the diffraction peaks is due to the curvature and finite size of the graphene sheet.
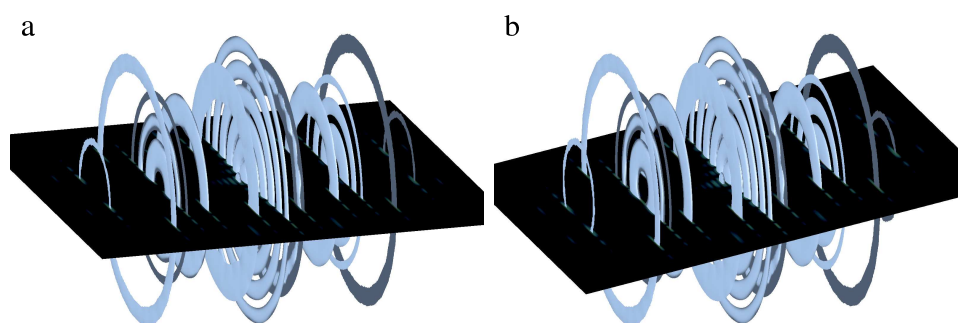
Figure 4.12: Three-dimensional Fourier transform of the (8,3) carbon nanotube, and a section of the Ewald sphere (the diffraction pattern) observed for normal incidence (a) and a sample tilt of 10° (b). The discs intersect with the Ewald sphere on lines orthogonal to the tube axis. If the sample is tilted, the intensities along the lines change, but the ratios of the line distances ($d_1 - d_3$ in Fig. 4.11) do not change.

We can therefore determine the rolling angle independent of the sample tilt. Also the diameter determination from the equatorial line is independent of the angle of the incident beam. The angle between the beam and the tube can be measured by comparing the experimental pattern with simulated ones.

For identifying the indices of a nanotube from a diffraction pattern, a measurement of the diameter and angle from the pattern as described above can be used as a starting point. Then, the simulated images are needed. Once a matching structure is found, the most important aspect for an unambiguous identification is to *exclude* all other possible nanotube structures (within a reasonable range of angle and diameter). For a sufficiently sharp diffraction pattern, there is usually only one set of indices (n,m) for which the simulated diffraction pattern matches the experimental data. Only for very large diameter nanotubes, the parameters (diameter and angle) of the different candidates are spaced so close together that they can not be distinguished.

4.4.2 Experimental procedure

All SWNT diffraction patterns were obtained using a Zeiss 912Ω transmission electron microscope. It is equipped with a (thermal) LaB_6 electron gun, a Köhler illumination system, and an energy filter. Images can be taken on two CCD cameras with different fields of views. The diffraction patterns are recorded on image plates. The image plates provide a very high sensitivity and dynamic range, which is not matched by film or any CCD camera. CCD cameras, and (to some extent) conventional film, suffer from a "blooming" effect: Intensity from strongly excited, saturated pixels spreads out into the nearby regions, occulting weak intensity diffraction peaks.

Unless noted otherwise, the following procedure and conditions ("standard conditions") are used for obtaining diffraction patterns. The microscope is operated at an acceleration voltage of only 60kV, below the threshold for knock-on damage in carbon nanotubes which is 87kV [58]. The Köhler illumination condition is used with an illumination angle between 0.1 and 0.2 mrad. The illumination is limited to a straight section of the carbon nanotube using the condenser aperture. The smallest condenser aperture, which has a diameter of 5μm, produces an illuminated region (demagnified image of the aperture) with a diameter of approximately 130nm. An image of a carbon nanotube illuminated under these conditions is shown in Figure 4.13. Before switching to diffraction mode, the focus is tuned to the minimum contrast condition. The energy filter is set to a width of $15-20$eV. The diffraction image is recorded on image plates with a camera length of 450mm or 580mm and exposure times of 4 or 5 minutes.

As a reference, diffraction images are recorded under the same conditions, except for a shorter exposure time, from the metal contacts. These contacts are polycrystalline, producing Debye-Scherrer ring type of diffraction patterns. From these, a precise scale is obtained. More important, any diffraction astigmatism remaining after alignment can be detected and compensated. Figure 4.14 shows two such reference images.

4.4.3   Discussion of experimental parameters

Previous diffraction work on individual single-walled carbon nanotubes [57] was performed in transmission electron microscopes equipped with a field-emission electron source, resulting in highly coherent illumination. Therefore, diffraction images could be recorded with short exposure times, probably before significant damage to the nanotubes occurred. However, it can not be excluded that surface reconstruction and dimensional changes due to the electron irradiation [59] change the nanotube structure during the exposure.

Using a thermal emitter, we need longer exposure times. Operation below the threshold for knock-on damage makes it possible to have stable conditions throughout the long exposure times. It is possible to obtain several diffraction images from the same nanotube section without loss of quality. Further, minimizing damage is important if transport or Raman investigations are to be carried out later on the same nanotube.

Figure 4.15 shows three diffraction patterns obtained on the same nanotube with different settings. It clearly shows the effect of the energy filter and the selected-area aperture. The energy filter strongly reduces the diffuse background. The selected area aperture is used in combination with the smallest condenser aperture, and it does not further limit the sample area contributing to the diffraction pattern (the selected-area aperture here is larger than the smallest condenser aperture). The selected-area aperture is not well aligned on the back focal plane: It cuts off a significant part of the diffraction pattern. Alignment is difficult, since the weak
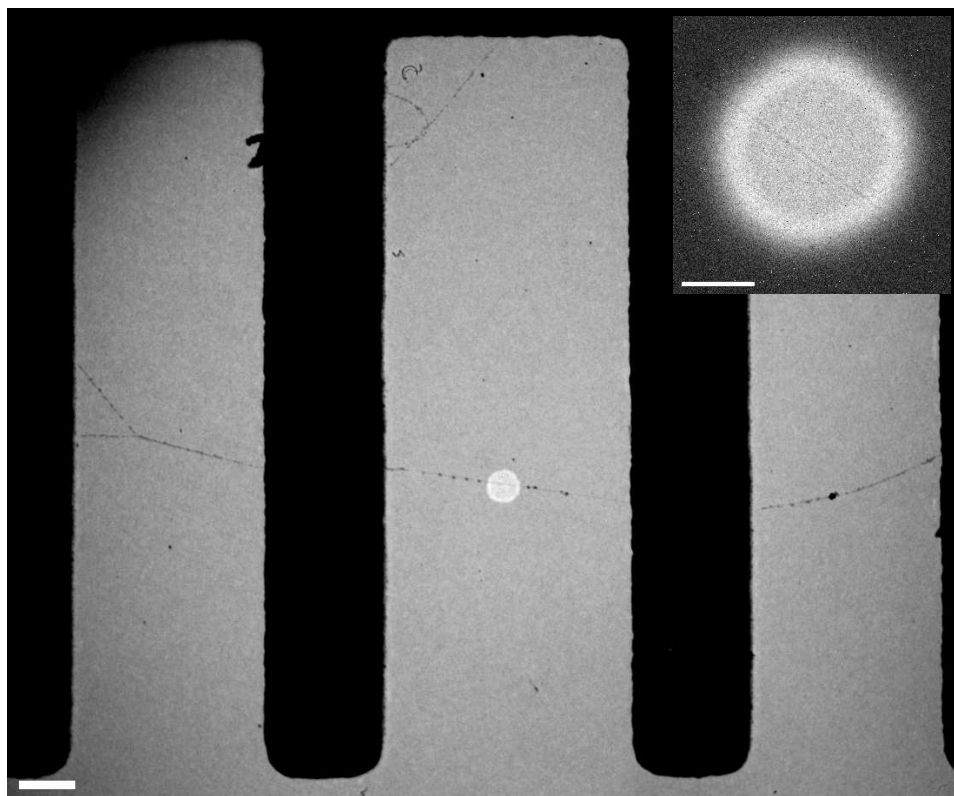
Figure 4.13: Inset: An individual SWNT within the illuminated region of the smallest condenser aperture. Main image: Overlay of a TEM image of the fully illuminated sample with an image of smallest condenser aperture (bright spot in the center). This overlay shows the illuminated section of the nanotube (for a diffraction pattern) in relation to the sample structure. The illuminated region for the smallest condenser aperture has a diameter of 130nm. Scale bar is 200nm, and 50nm for the inset.

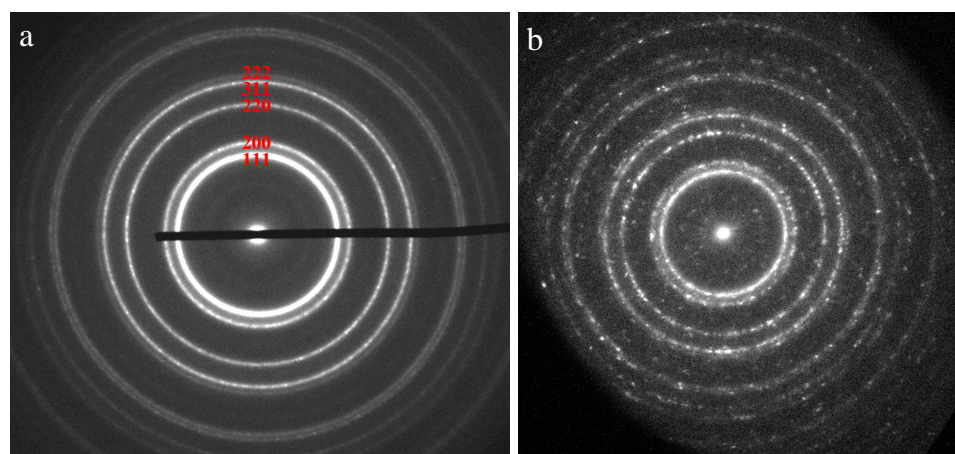Figure 4.14: Diffraction patterns obtained from the contact regions, showing Debye-Scherrer rings. For a large illuminated region continuous rings are obtained (a). For a small illuminated area, the granular structure due to the small number of illuminated domains is visible (b). The gold contacts are polycrystalline with fcc structure. These diffraction images serve as reference for the camera length and to measure astigmatism in diffraction mode. A small astigmatism (slightly elongated circles) is visible in (a).

diffraction intensities can not be seen on the viewing screen or CCD camera. It is therefore preferable to use only a sufficiently small condenser aperture.

All diffraction images obtained in this way (e.g. Fig. 4.15 a+b, Fig. 4.16a-c, and Fig. 4.18 a+c) show intense radial lines starting from the central peak. These are due to electrons scattered into high angles at the condenser aperture. They are partially shadowed by the structure of the sample. A shadow of the sample structure is visible in the diffraction pattern due to this effect, quite clearly seen in Fig. 4.15a.

With a sufficiently sharp diffraction pattern, an unambiguous assignment of the nanotube structure, or nanotube indices (n,m), is possible. A straight, clean nanotube is required - a curved nanotube is not a 1D periodic structure. In the high-resolution images of suspended nanotubes we were able to obtain a sharp image only from the ends, due to vibrations of the central part. Such vibrations are not a problem for diffraction analysis: A *translation* of the nanotube does not change the diffraction pattern. Only if the vibrations are so large that the *orientation* of the tube varies, it leads to a blurred diffraction image. Fig. 4.16 shows three examples of sharp diffraction patterns.

Although all diffraction images were recorded at the same microscope, it seems that the key ingredients for a single-tube diffraction analysis are the small condenser aperture, image plates for recording of the diffraction patterns, and very straight nanotubes. The condenser aperture limits the illumination to the region of interest (the nanotube section). Selecting the area downstream of the sample (using
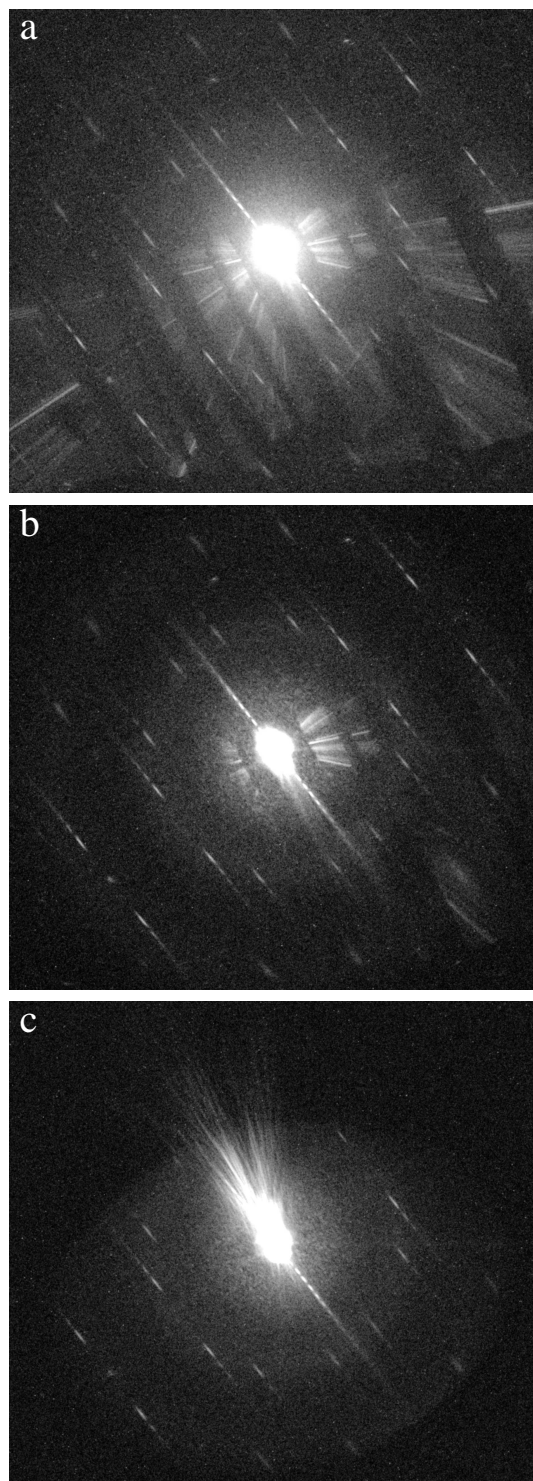
Figure 4.15: Diffraction patterns of the same nanotube, without energy filter (a), with energy filter (b), and with the selected-area aperture inserted in addition to the condenser aperture (c). The energy filter reduces the diffuse background. The selected-area aperture removes the shadow image of the structure, but also cuts off significant parts of the diffraction pattern.

Figure 4.16: Examples of diffraction patterns. (a) (16,09) nanotube, (b) (13,13) "armchair" nanotube. (c) Diffraction pattern obtained on the intersection of a (16,05) and (18,02) nanotube. A background subtraction was done on images (a) and (b).

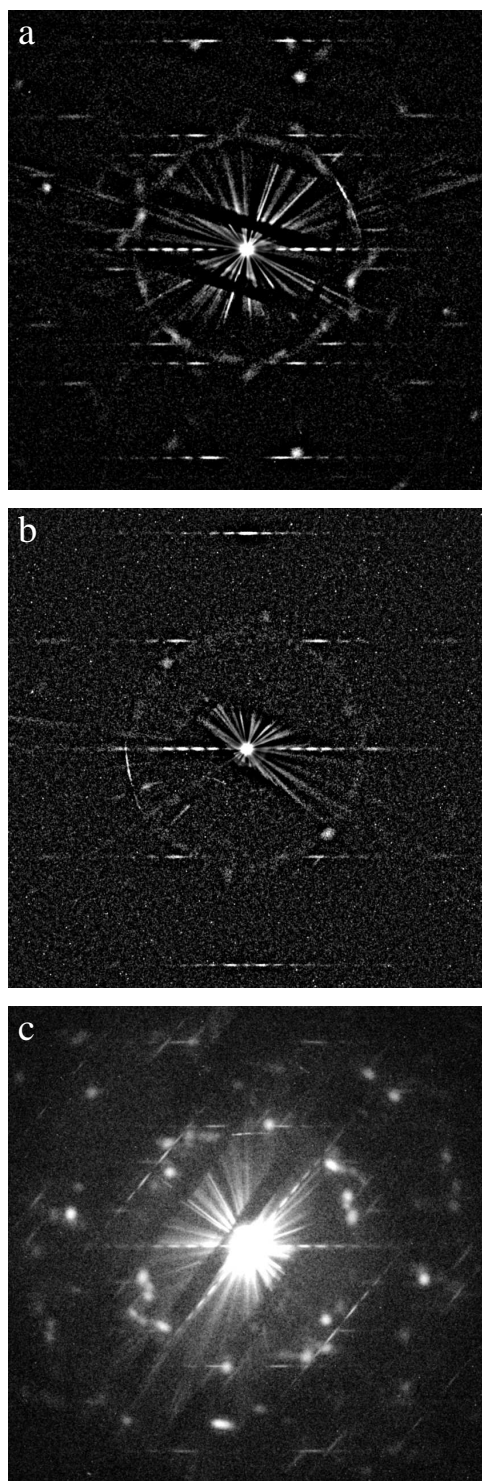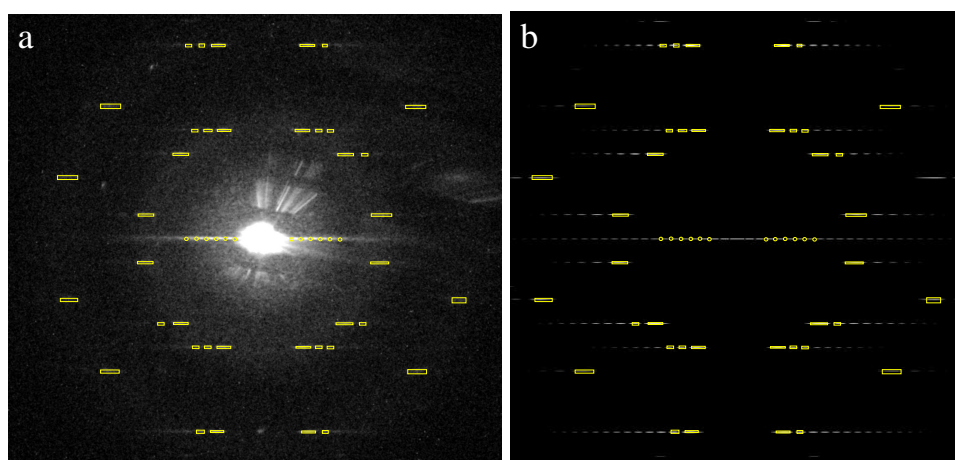Figure 4.17: Index assignment: (a) The peaks in the experimental diffraction pattern (from figure 4.15b) are marked. A box is drawn around the streaked graphene peaks, and in the equatorial line the minima are marked. In (b), the experimental image is replaced by a simulated one, without change in the marks. The indices and incidence angle in the simulation are changed until the pattern matches. Here, the pattern matches only one pair of indices (n,m)=(24,11). The incidence angle is within 3° of normal incidence. We verify that all nearby indices clearly deviate from the experimental pattern.

only the selected area aperture) fails, since many other contributions (e.g. reflections from the metal contact, inelastic contributions) still reach the detector. The smallest unwanted contributions will occult the very weak diffraction intensities from the small number of atoms in our nanotube. We have seen that the energy filter is not necessary, but improves the image quality. The Köhler illumination condition provides a homogeneous incident beam; however, convergent-beam electron diffraction (shown below) is also possible on individual nanotubes.

4.4.4 Index assignment

For the analysis, the diffraction images are rotated to have the equatorial line in a horizontal direction. If any astigmatism is found in the reference patterns, it is compensated by rescaling and shearing the images by the appropriate amount. In some cases a background subtraction is useful (Figure 4.18). The above steps can be done with the ImageJ software and The Gimp (there is a version capable of manipulating 16 and 32-bit images, called FilmGimp).

The rotated, background subtracted and rescaled images are then imported in xfig. Here, the features in the image are marked (Figure 4.17). Then, simulated images are placed instead of the experimental underneath the marks, to find those which match. We find that for a sharp diffraction pattern there is exactly one set of indices (n,m) for which the simulated image matches the experimental one. The
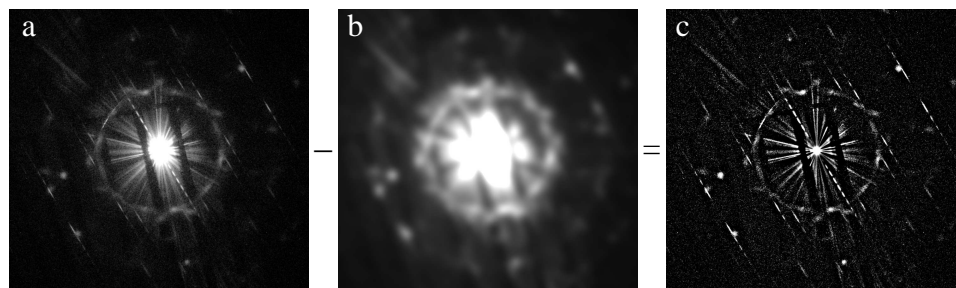
Figure 4.18: Background subtraction: The image before (a), and and after a large Gaussian blur is applied (b). Subtracting (b) from (a) yields the background subtracted image (c). This is equivalent to high-pass filtering.

smallest individual carbon nanotube that was identified is a (7,7) nanotube, which has a diameter of 0.94nm. One of the largest identified nanotubes is (39,26) which has a diameter of 4.44nm.

Figure 4.19 shows the statistics of indices obtained from nanotubes all grown in the same CVD process, using methane as carbon feedstock with Ni nanoparticle catalyst. It clearly shows that the rolling angle is not randomly distributed, but is biased towards the armchair orientation.

4.4.5   Discussion of the index distribution

Figure 4.19 clearly shows that the rolling angle is not randomly distributed, but is grouped towards the armchair orientation in this material. This is a direct measurement and it includes metallic nanotubes. Fluorescence spectroscopic results [31, 32] show a similar trend, but are limited to semiconducting tubes and are biased by a structure-dependent fluorescence quantum yield. The Raman study in Ref. [28] finds a more or less random distribution of nanotube indices in HiPCO nanotubes. Note that all these index distributions are obtained from nanotubes grown with different methods and parameters. As demonstrated in [32] the index distribution strongly depends on growth conditions. We can compare the angular selectivity in our material with fluorescence studies of nanotubes produced by alcohol catalytic CVD (ACCVD) under optimized conditions [32] and of nanotubes grown from solid-supported Mo/Co catalyst (MoCo) [31], under the assumption of a structure-independent fluorescence yield. An angle of 30° represents armchair nanotubes, 0° a zigzag tube, and an average of 15° is expected for a random distribution. The average angle in the MoCo material, calculated from the fractional intensities listed in [31], is 22.8°. The optimized ACCVD appears to yield predominantly (6,5) (27°) and (7,5) (24.5°), but also significant amounts of (8,3) (15,3°) and (8,4) (19.1°). The intensities in [32] are given only in a graphical representation, from which we estimate an average angle of ≈23°. In our sample the mean angle is 25° if we include all nanotubes, and 24° if we exclude the metallic tubes for a better comparison with the fluorescence spectroscopic results. Due to the
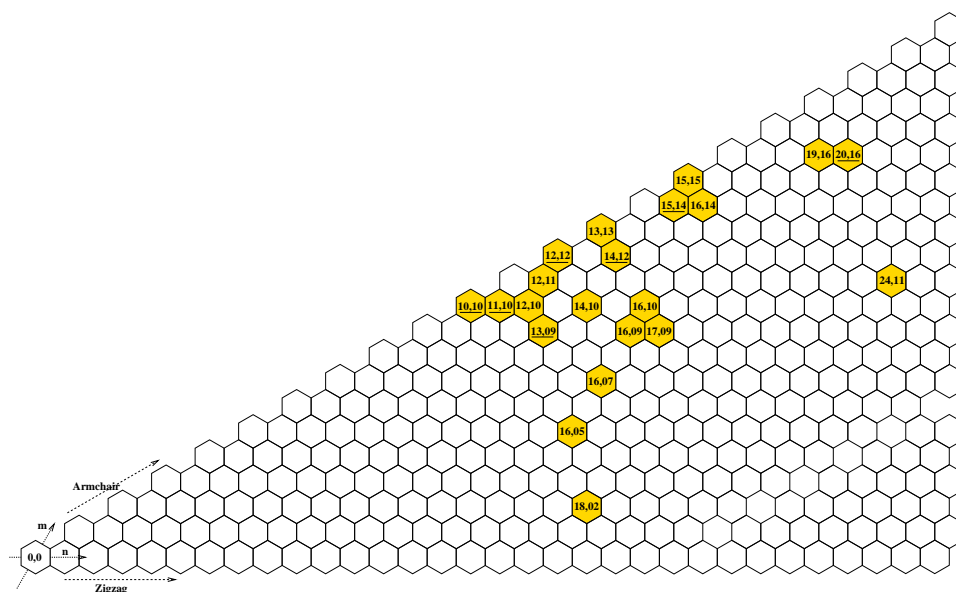
Figure 4.19: Nanotube indices of tubes grown in the same CVD process. The underlined indices were encountered more than once. The rolling angle is not randomly distributed, but is close to the armchair direction (30°) in the majority of the nanotubes in this material.

much larger diameters obtained in our CVD process, there are many more different nanotube species possible within a given angle interval. The angular selectivity towards armchair tubes, however, is comparable or stronger than in [31] or [32].

4.4.6 Accuracy of the simulation methods

The single-walled carbon nanotube is one of the few systems well described by the weak phase object approximation (WPOA). In addition to calculations [12], the validity of the WPOA is demonstrated in an impressive way by the oversampling and iterative phase retrieval for a nanotube from diffraction intensities [60]. The reconstruction in [60] is based on the WPOA, and has worked for the large double-walled carbon nanotube. However the iterative phase retrieval is not possible from our diffraction data, because it requires the fully coherent illumination of a short nanotube section which is available only with field-emission electron sources.

From a Fourier transformation of the projected potential (Figure 4.5), one can quickly calculate a simulated diffraction pattern (e.g. Figure 4.11). This approach approximates the visible section of the Ewald sphere as a plane. The computationally more expensive path summation approach (section 4.2.3) naturally includes the curvature. Although the difference is small, it can be detected in the simulated images, and in experimental diffraction patterns for non-normal incidence. The effect of the curvature is illustrated in Figure 4.20: The peak positions are slightly
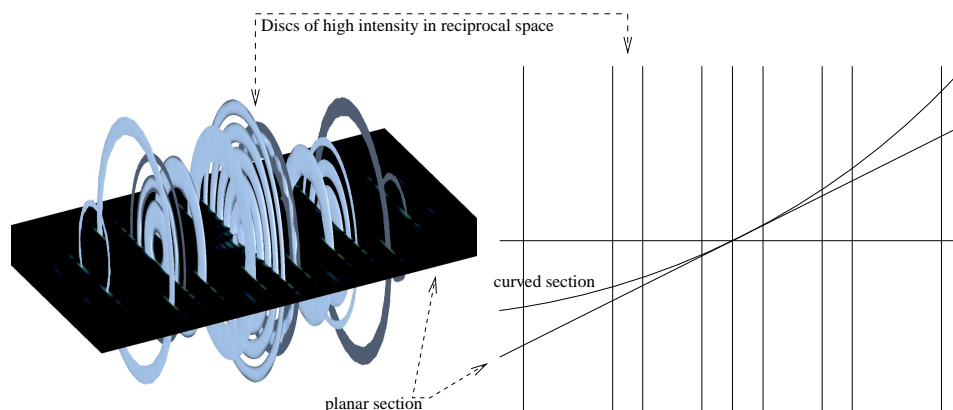
Figure 4.20: Effect of curvature of the Ewald sphere. 3D view of a planar section through the reciprocal space of an (8,3) nanotube for a non-normal incidence (left). Illustration of the planar section vs. curved section in Fourier space (right). The vertical lines correspond to the discs. The curvature is exaggerated for clarity.

changed, and for non-normal incidence, they are no longer symmetric with respect to the origin. This asymmetry can be seen in experimental diffraction patterns where the tube is not orthogonal to the beam, as shown in Figure 4.21.

As a conclusion, the planar approximation for the Ewald sphere in the simulation is sufficient for an index assignment for a close to normal incidence in the diffraction pattern. If the tube is tilted, the curvature of the Ewald sphere has a larger effect and has to be taken into account.

4.4.7   Convergent-beam electron diffraction

Although nanoarea electron diffraction using the Köhler illumination condition with a small condenser aperture has proven to be very reliable, we would like to show also the possibility of convergent-beam electron diffraction (CBED) on individual single-walled carbon nanotubes. Here, the illuminating electron beam converges to form a small probe of a few nm on a straight nanotube section. Consequently, the diffraction pattern consists of extended discs instead of sharp points. It is possible to investigate even smaller nanotube sections in this way. An unambiguous nanotube index assignment, however, is not possible (it could be possible in combination with a very accurate diameter estimate from a high-resolution image). The image is again recorded on image plates with an exposure time of five minutes.

A convergent beam electron diffraction pattern of an individual single walled nanotube is shown in Figure 4.22. A distorted image of the tube is visible in each spot (in fact the tube is straight). In this way the rolling angle of a short segment can be detected. Unfortunately, the periodicity in the equatorial line can not be seen in this image. Even if the indices can not be determined, CBED may be useful for
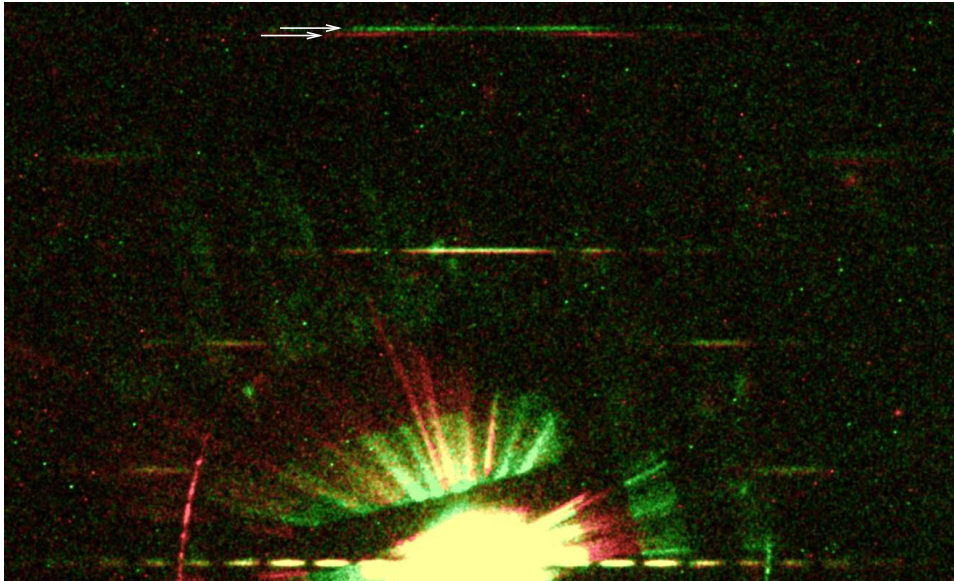
Figure 4.21: The curvature of the Ewald sphere leads to an asymmetry in the diffraction pattern for non-normal incidence. This pattern is obtained from a nanotube identified as (16,05), with an incidence angle of 17° with respect to normal incidence. The lower half of the diffraction pattern is rotated by 180° and overlayed onto the top half with a different colour. In this way the asymmetry is visible, clearly at the point indicated by the white arrows, where the red and green coloured peaks do not coincide.

Figure 4.22: Convergent beam electron diffraction (CBED) image of an individual single-walled carbon nanotube. Original (a) and background subtracted image (b). The orientation of the graphene lattice is visible, but the equatorial line is not. The illuminated nanotube section is visible in each of the diffraction spots. In (b) part of the reciprocal graphene l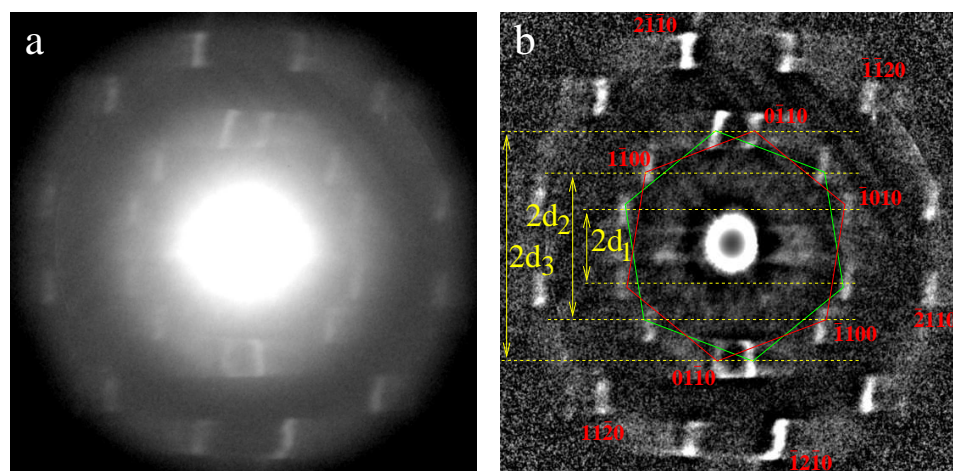attice and indices according to Fig. 4.11 are shown. The hexagons do not precisely match the peaks due to non-normal incidence. The rolling angle of the nanotube can be calculated from the distances $d_1 - d_3$ according to equation (4.53), and in this example we obtain $12.5 \pm 0.5°$.

an analysis of the rolling angles of carbon nanotubes, which can be measured from the relative distances as indicated in Fig. 4.11.

4.4.8   Diffraction on MWNTs and peapods

Diffraction is possible on a wide range of nanotube structures, from small to large single-walled carbon nanotubes, double-walled nanotubes (DWNTs), multi-walled nanotubes and filled tubes. In double-walled nanotubes, multi-walled nanotubes, and nanotube bundles, multiple orientations of the graphene lattice are visible in a diffraction image. An index assignment is usually not unique, as it is not clear which tube diameter belongs to a specific orientation. Detailed considerations for assigning the indices of DWNTs can be found in [61].

A Diffraction pattern of a multi-walled carbon nanotube (MWNT) is shown in Figure 4.23. A large number of different orientations of the graphene sheets are visible. There are approximately as many different orientations of the graphene lattice present as there are nanotube shells. This shows that, unlike graphite, each graphene layer in a MWNT exhibits a different orientation.

A very interesting hybrid nanotube structure are endohedral metallofullerene peapods ($Dy@C_{82}@SWNT$) (see chapter 6). It is possible to observe the periodicity of the filling in a diffraction pattern obtained from a small bundle. This image is shown in Figure 4.24, and the arrows indicate the features attributed to the peapod
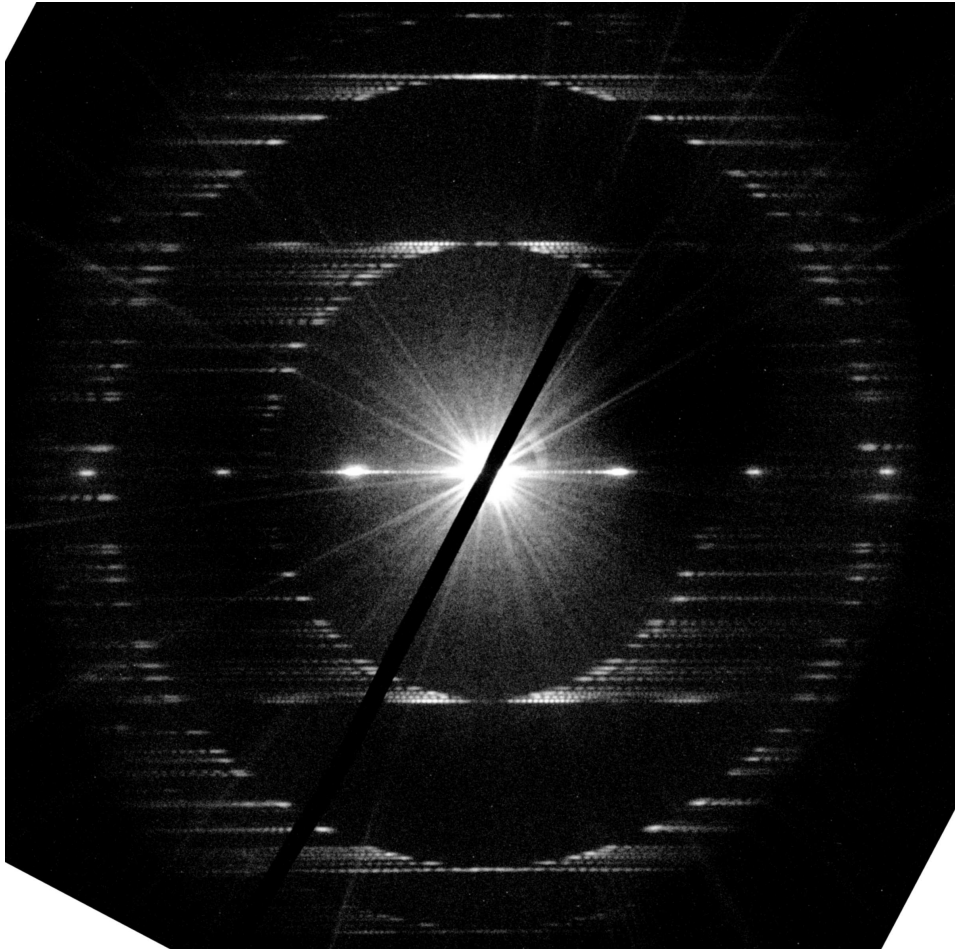
Figure 4.23: Diffraction pattern of a multi-walled carbon nanotube (MWNT). There are approximately as many different orientations of the graphene lattice present as there are nanotube shells.

structure. The periodicity of the fullerenes is found to be 10.8 ± 0.4Å, in agreement with values found by high-resolution TEM and diffraction in [62] and [63]. Due to the bundling, the indices of the many different host tubes can not be separately determined.

Figure 4.24: (a) Diffraction pattern obtained from a bundle of Dy@C_{82}@SWNT endohedral metallofullerene peapods. The 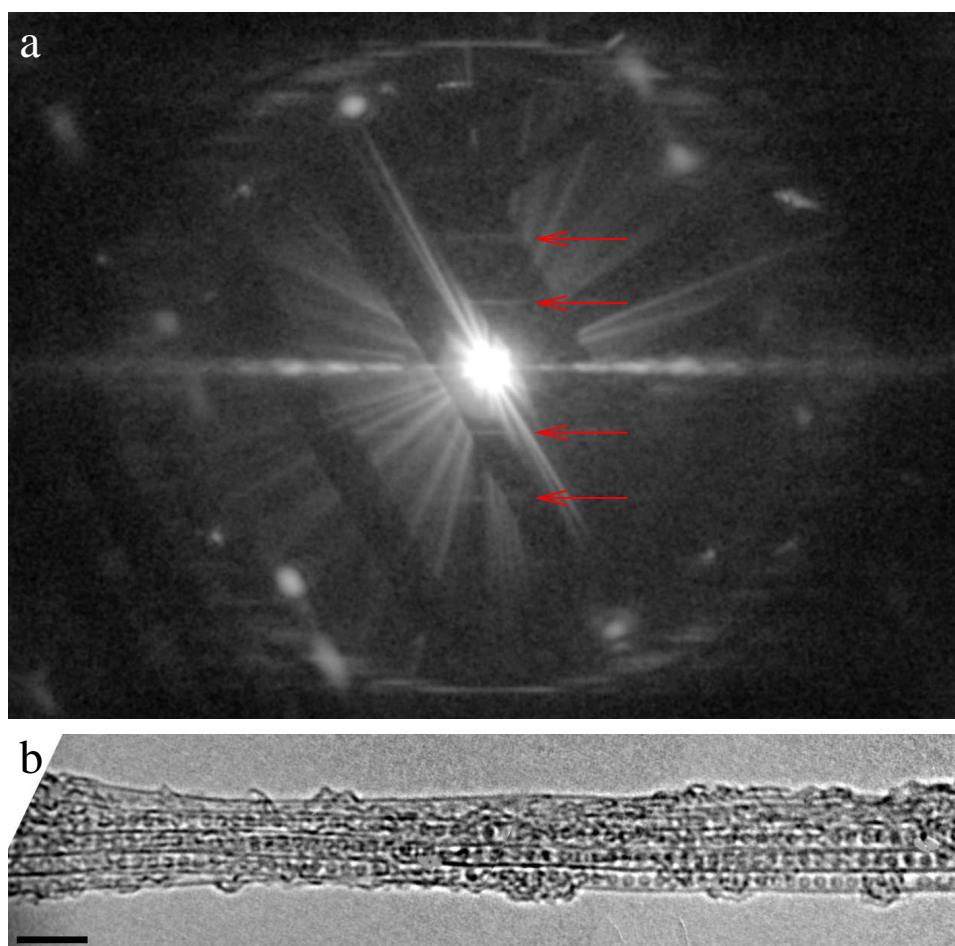arrows indicate the features attributed to the periodic fullerene structure inside the nanotubes. The periodicity of the filling is 10.8 ± 0.4Å. (b) High-resolution images of a bundle of similar size in the same sample. Scale bar in (b) is 5nm.

Chapter 5

Raman spectroscopy on Index-assigned nanotubes

Raman spectroscopy is an important technique in the characterization of carbon nanotubes [16, 64]. As explained in the introduction, Raman spectroscopy probes vibrational modes of carbon nanotubes, and information about electronic transitions can be obtained from the laser energy. The characteristic features of the Raman spectrum of single-walled carbon nanotubes (SWNTs) depend on the nanotube structure, defined by the indices (n,m) [65]. However, there is so far no independent determination of a nanotube structure in combination with its Raman modes. All previous assignments of Raman modes to specific nanotube indices are based on a modelisation of the vibrational and electronic properties. We present the first Raman spectroscopic studies on individual nanotubes in combination with an independent identification of the tube structure by electron diffraction.

The so-called radial breathing mode (RBM) is a fingerprint of single-walled nanotubes, and its frequency is related to the nanotube diameter. From the RBM frequencies measured on precisely identified nanotube structures, we obtain an RBM vs. diameter relationship that does not depend on any modelisation of nanotube electronic or mechanical properties. The relation of the RBM frequency ω_{RBM} to the inverse nanotube diameter $1/d$ is often given as a linear relation with two parameters A and B:

$$\omega_{RBM} = \frac{A}{d} + B \tag{5.1}$$

This relation agrees well with various calculations and experiments [16, 64, 66, 67, 65, 68, 28, 29, 69], however, the actual values found for A and B vary significantly. While the parameter A is interpreted as a "spring constant" for the C-C bond, the value B is commonly attributed to an interaction with the environment (substrate, nanotube bundle, or detergent). It is therefore expected to be zero in this interpretation for a perfectly isolated nanotube .

Although our nanotubes are freely suspended, we find a non-zero value for B. Further, we obtain the precisely same RBM frequencies as found for nanotubes
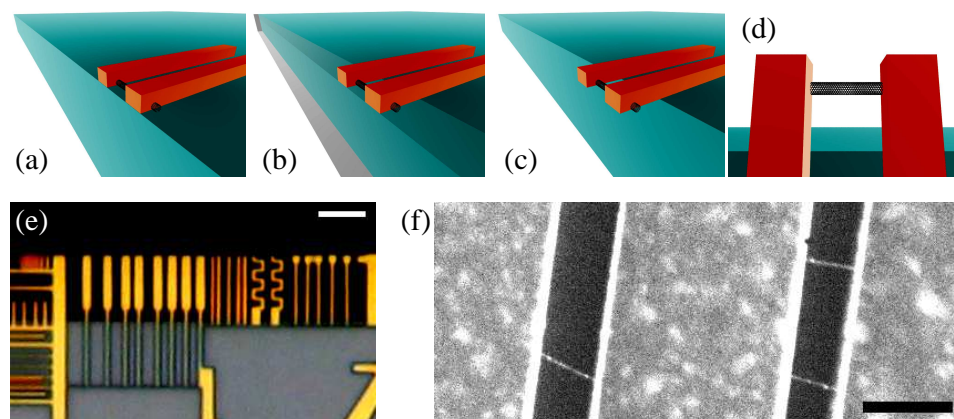
Figure 5.1: Sample preparation procedure: (a) The substrate is cleaved through a metallic grid which is on top of the carbon nanotubes. (b) The sample is etched so that the structure is mainly undercut from the side, removing the shaded volume. The resulting structure (c) reaches out across the side edge of the substrate. Since the nanotube is still held by the metal contacts, and the substrate is no longer in the way, it is accessible for TEM investigations (d), viewed from top. (e) is an optical microscope image of a free-standing structure (scale bar 5μm). The location of carbon nanotubes within the structure is known from overview TEM images (f), so that micro-Raman measurements are possible on precisely located nanotubes. (f) is a dark-field mode TEM image. Scale bar is 1μm.

on a substrate in previous works. This agreement in spite of the very different environment shows that the influence of the environment on the RBM frequency can not explain the experimentally found values for B.

This combined Raman study was done in a collaboration: Raman spectra were measured by M. Paillet and T. Michel at the University of Montpellier, France. Additional Raman measurements were done by A. Neumann and G. S. Duesberg at Infineon technologies, Munich. Further, the individual single-walled carbon nanotubes used in these and several other experiments were grown by CVD by M. Paillet and G. S. Duesberg.

5.1   Experimental procedure

As described before, structures with carbon nanotubes are created on the edge of a cleaved substrate and made free-standing with an etching process. The single-walled carbon nanotubes are grown by chemical vapour deposition (CVD) on highly doped silicon substrates with a 200 nm Silicon dioxide layer [25]. A metal structure consisting of 3 nm Cr and 110 nm Au is created by electron beam lithography on top of the as-grown carbon nanotubes. The substrate is then cleaved

through the metal grid structure. An etching process, as described before, is used to obtain free-standing nanotubes.

On half of the free-standing nanotube samples, a tiny amount of silver is deposited by thermal evaporation. The amount corresponding to a 1 nm thick layer forms separated silver particles with a few nm in diameter along the nanotube [70, 71]. Two small particles are visible in Fig. 5.3d. We find that the silver deposition on the nanotubes can lead to an increase of the Raman intensity.

Since the substrate is no longer in the way, TEM is possible on the free-standing part of the structure on the edge of the substrate. The carbon nanotubes are held in place by the metal structure. Before the micro-Raman experiments, overview TEM images are obtained at low dose and voltage (60 kV) to get the position and orientation of carbon nanotubes with respect to the metal structure.

The metal structure is visible in the optical microscope, and the overview images show the nanotube location and their orientation with respect to the metal grid. It is now possible to carry out micro-Raman experiments on a perfectly localized and oriented single tube. A first series of room-temperature Raman spectra were measured using the Ar/Kr laser lines at 488 nm (2.54 eV), 514.5 nm (2.41 eV) and 647.1 nm (1.92 eV) in the back-scattering geometry on a triple subtractive Jobin-Yvon T64000 spectrometer equipped with a liquid nitrogen cooled charge coupled device (CCD) detector. Another series of spectra were collected using a tunable laser (1.57 eV-1.7 eV) with a Dilor XY800 spectrometer. In all the experiments the instrumental resolution was 2 cm^{-1}. A precise positioning of the tubes under the laser spot (1 μm laser spot) was monitored with a piezoelectric nano-positioner. In our experimental configuration, the incident light polarization is along the SWNT axis (the Z axis), and no analysis of the polarization of the scattered light is done.

After measuring the Raman spectra, diffraction patterns and high-resolution TEM images of the same nanotubes that were investigated by Raman spectroscopy are obtained. We record diffraction patterns on image plates in a Zeiss 912Ω microscope operated at 60 kV as described in Chapter 4. With an electron diffraction pattern that matches only a single pair of indices (n,m), the diameter is precisely known given the length of the carbon-carbon bond. Our diameter values are based on a C-C distance of 1.42 Å.

5.2 Results

After the Raman measurements, we have analyzed by electron diffraction all the nanotubes that showed a Raman signal. Among these tubes, three times the (11,10) nanotube was found. On the whole, we have obtained spectra from 10 unambiguously identified nanotubes: (11,10) (3 times), (15,6), (16,7), (12,12), (17,9), (15,14), (27,4) and (23,21). Furthermore, we measured the spectra from two other tubes that could not be fully identified, but of which diameters were quite precisely determined from the equatorial lines of their diffraction patterns, i.e. 1.64 ± 0.05 nm and 2.3 ± 0.05 nm.
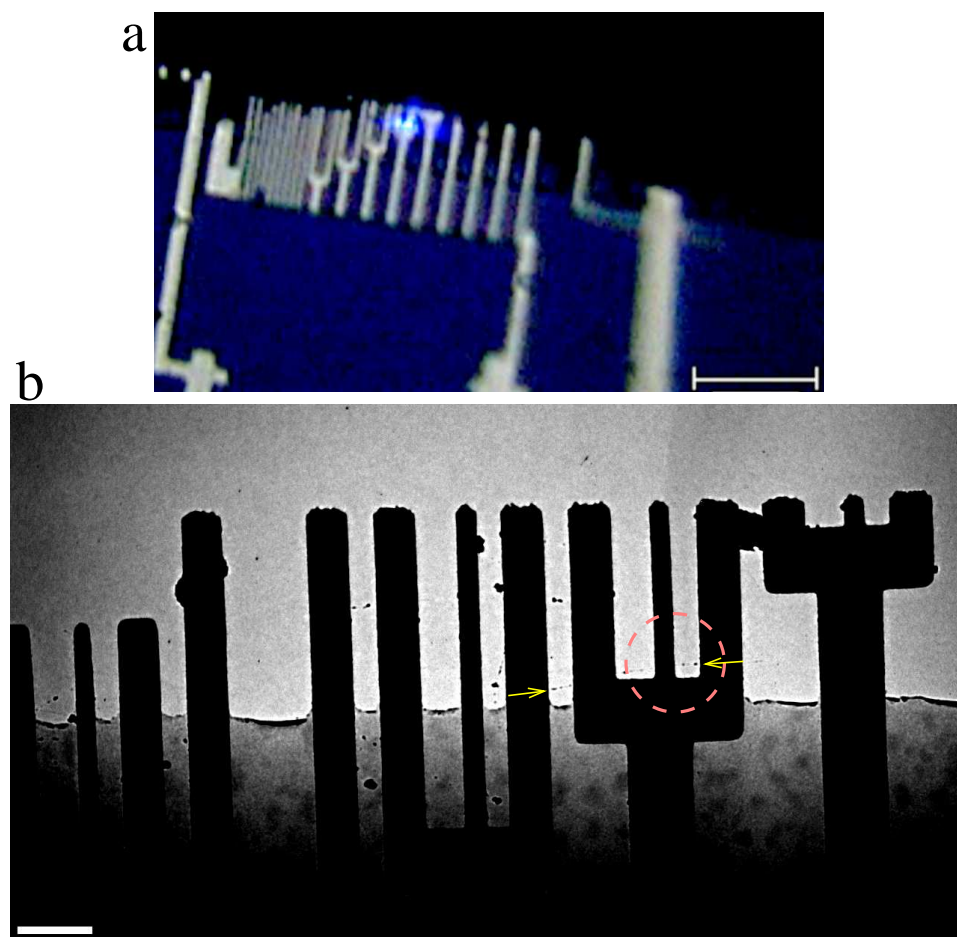
Figure 5.2: (a) Optical microscope image of a free-standing structure, taken through the microscope of the Raman spectrometer. The blue laser spot is visible. (b) Low magnification TEM image of the same free-standing structure with suspended carbon nanotubes. Since the location of the nanotubes is known, Raman spectroscopy can be carried out on precisely located and oriented nanotubes. Indicated by the dashed circle in (b) is the region where the spot of the Raman laser is focused. The arrows point at a nanotube bridging several contacts and crossing the laser spot. Scale bar is 20μm (a) and 1μm (b).
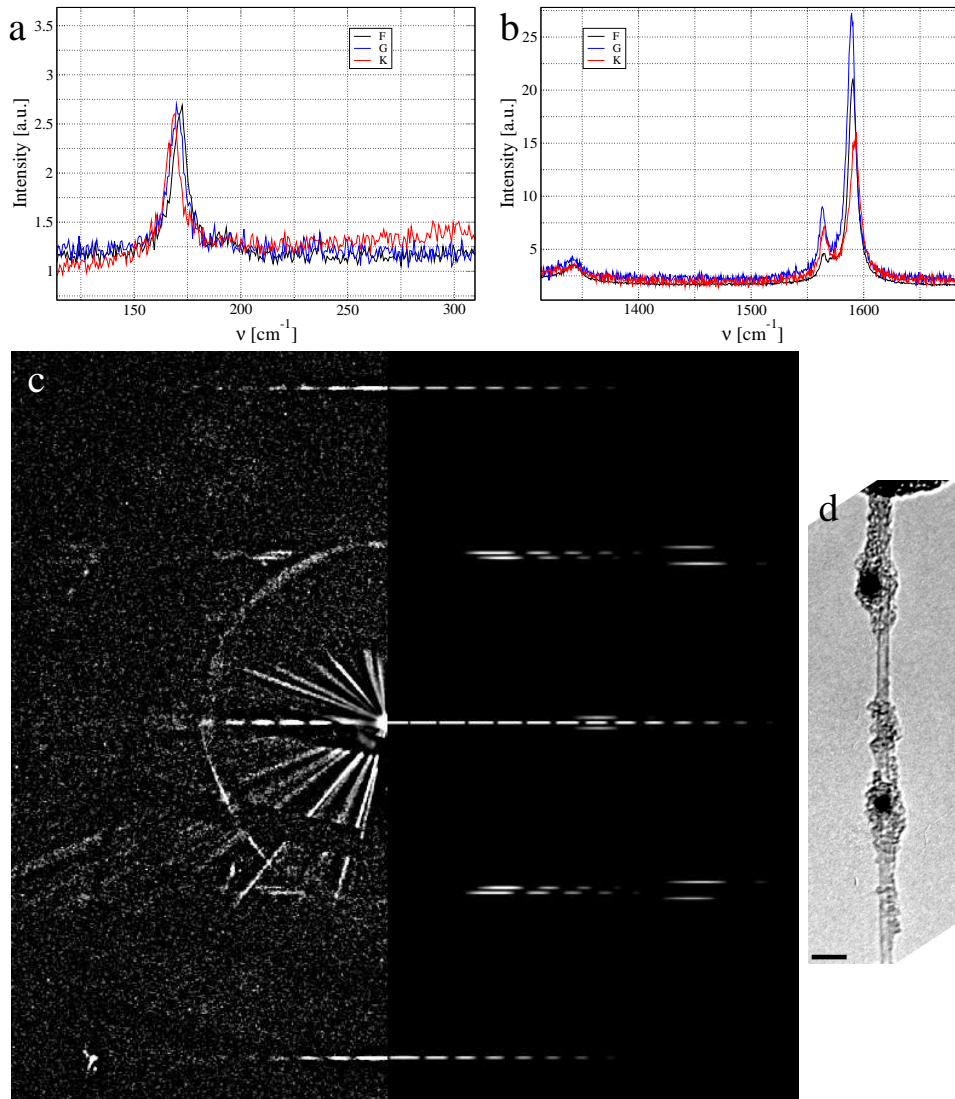
Figure 5.3: (a) RBM and (b) TM ranges of the three different (11,10) SWNTs (E_{Laser}=2.41 eV). The features are well reproduced and the differences are within the experimental error. Only a small D line is visible at $1341cm^{-1}$. (c) Diffraction pattern from one of the (11,10) nanotubes (left: experimental, right: simulated image). (d) High-resolution TEM image of the same nanotube. Two small silver particles are visible, and at the upper end is one of the contacts. Most of the amorphous carbon is deposited during the TEM analysis.

n	m	d [nm]	(°)	E [eV]	RBM	HWHM
11	10	1.42	28.4	2.41	169.5	3.5
15	6	1.47	16.1	1.7	166	3
16	7	1.6	17.3	1.574	154	4
12	12	1.63	30	1.63	151	3.5
17	9	1.79	19.9	2.41	140.5	3.5
15	14	1.97	28.9	1.92	129	3.5
27	4	2.29	6.8	1.92	119	5.5
23	21	2.98	28.5	1.6	95	6.5

Table 5.1: Structural indices (n,m) determined by electron diffraction, RBM frequencies and their Half Width at Half Maximum (HWHM) [1/cm] measured by Raman spectroscopy with a laser energy E on each nanotube.

Tube	d [nm]	E [eV]	RBM	HWHM
(18,02) or (16,05)	1.494 or 1.488	2.41	165	3.5
-	1.59...1.69	2.41	153	3.5
-	2.25...3.35	1.92	116	7

Table 5.2: Additional data for the dependence of the RBM on the diameter from tubes that could not be identified. In one case there are two tubes (18,02) and (16,05) under the laser spot; in the other two cases only a diameter estimate was possible from the equatorial line of the diffraction pattern.

Figure 5.3 shows the Raman spectra (using a 2.41 eV excitation) and the diffraction pattern of one (11,10) SWNT. We have measured nearly identical spectra for the three different (11,10) nanotubes. The single RBM and the two dominant modes in the TM range are reproduced within the experimental error. The reproduction of the Raman spectra validates that the Raman spectra and diffraction patterns were indeed obtained from the very same object.

The exact determination of the transition energy of a SWNT requires the measurement of the resonance profiles with a broad set of laser lines [28, 68]. However, the measurement of a detectable signal for the 2.41 eV incident energy means that one transition energy of the (11,10) SWNT is close to 2.41 eV. As expected for an individual SWNT, the Raman spectrum is featured by a single narrow RBM located at 169.5 cm^{-1} (FWHM = 7 cm^{-1}). The profile of the (11,10) TM bunch, displayed in Fig. 5.3b, is well fitted by using two lorentzian components located at 1593.5 cm^{-1} (FWHM = 6 cm^{-1}), and 1566 cm^{-1} (FWHM = 7 cm^{-1}). This TM profile is in agreement with ab initio calculations [72].

Raman data of further identified nanotubes is shown in table 5.1. The index assignment is solely based on the electron diffraction analysis, and not on the Raman data. The majority of the Raman spectra are recorded on regions of micrometric
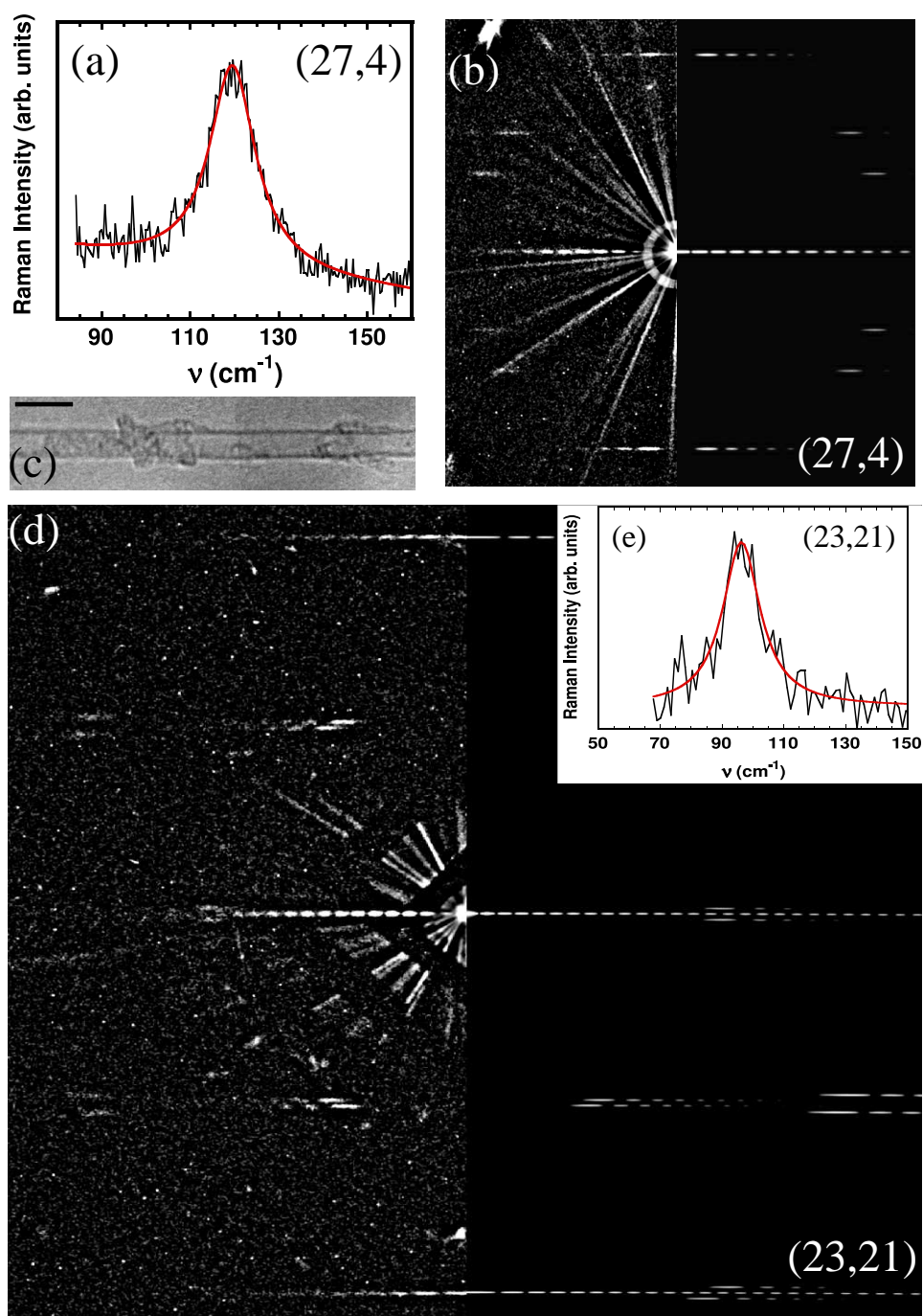
Figure 5.4: (a) RBM of the (27,4) SWNT (E$_{Laser}$=1.92 eV), (b) electron diffraction pattern and (c) high-resolution TEM image of the (27,4) SWNT (scale bar 5nm). (d) Electron diffraction pattern of the (23,21) nanotube, and (e) RBM (E$_{Laser}$=1.6 eV) of the (23,21) SWNT. The red line is a Lorentzian fit. In each electron diffraction pattern the left half is the experimental image, while the right half is the simulated one for comparison.

size where only a single nanotube is detected by electron microscopy. In some cases, there are two nanotubes within or near the laser spot. We identify both of them and often find two very different diameters, so that only one of them is reasonable for the measured RBM frequency. For example, the (17,9) SWNT (1.79 nm) is partly bundled with another tube with diameter >2.2 nm, which cannot exhibit the measured 140 cm^{-1} RBM frequency. We will also use one data point where two tubes with nearly identical diameter were under the laser spot, and data from two tubes for which only a diameter estimate was possible (table 5.2).

Figure 5.4 shows the Raman spectra and diffraction patterns of the two tubes with the largest diameters of our data set, respectively the (27,4) and the (23,21) SWNTs. The diameters of these semiconducting nanotubes are 2.287 and 2.984 nm (with a$_{C-C}$ = 0.142 nm) and their chiral angles are 6.8° and 28.5° respectively. The RBM are located at 119 cm^{-1} (FWHM = 11 cm^{-1}) and 95 cm^{-1} (FWHM = 13 cm^{-1}) for the (27,4) and (23,21) tubes, respectively (Fig. 5.4a and e).

5.3   Discussion

5.3.1   RBM range

A huge number of experiments and modelisation efforts were made to relate the radial breathing mode (RBM) frequency to the nanotube structure. A review and summary of various models and experiments is given in [64]. Our experimental approach provides the first accurate and independent determination of the lattice structure of the tubes, (n,m) indices and then the diameters and chiral angles, with their RBM frequencies. Figure 5.5 plots the experimental relation between the RBM frequencies and the nanotube diameters obtained in this way. We point out that these results are covering an unprecedented diameter range (1.4 nm to 3 nm).

On Figure 5.5, the measured points agree with a line obeying the relation ω_{RBM} = A$/d$ + B, with A=204 cm^{-1}nm and B=27 cm^{-1}. This RBM vs. diameter relation is measured on individual free-standing tubes, while in previously established relations the individual nanotubes were lying on a substrate [29] or encapsulated in SDS micelles [28, 68, 69]. Further, we have investigated a diameter range that was never studied before. We find a good agreement in the diameter range between 1.4 and 1.7 nm where our diameter range overlaps with the previous works. However, an extrapolation of the previously established relationships to the larger diameter tubes (dashed lines in Fig. 5.5) does not agree with our data. Therefore, with the relations from [28, 69] for smaller diameters, the agreement in the overlapping diameter range, and our new data on large diameter nanotubes, the relationship between the RBM frequency and the inverse diameter is evidently non-linear.

Our results allow to discuss the structural (n,m) determination of the Ref. [29] which is only based on resonant Raman scattering data obtained by using the 1.58 eV laser excitation. We have measured the RBM frequencies of the (16,7) and (15,6) metallic tubes, and the RBM frequencies of these same tubes are given in
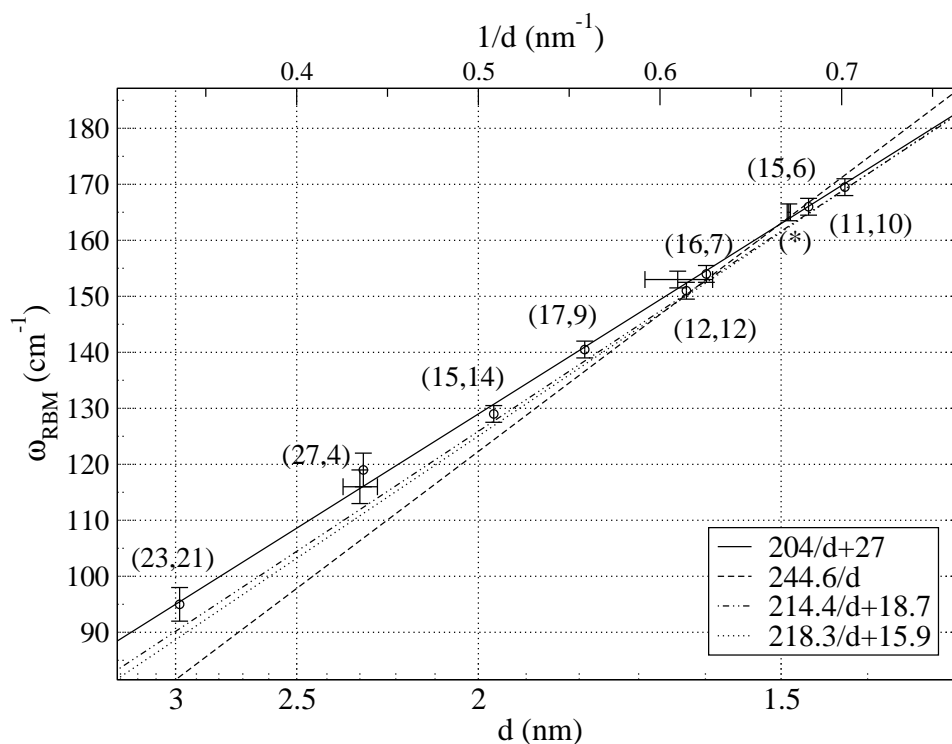
Figure 5.5: RBM frequencies vs. nanotube diameter for nanotubes identified by electron diffraction. Data points marked with a circle are from unambiguously identified nanotubes, and the indices are given in the diagram. For the data points with a horizontal error bar, only a diameter estimate was possible. The data point marked with a star is either from a (16,5) or (18,2), which have almost the same diameter (two tubes under the laser spot). Drawn as dashed lines are selected RBM vs. diameter relationships from literature [28, 29, 69] (the values from [29] are modified for a C-C bond length of 1.42Å instead of 1.44Å). The solid line best matches our data.

Table I of the Ref. [29]. A comparison between the two data sets shows a complete agreement for the (16,7), since we found $\omega_{RBM} = 154$ cm^{-1} ($E_{laser} = 1.57$ eV excitation). Concerning the (15,6), the RBM is located in our case at 166 cm^{-1} (165 cm^{-1} in Ref. [29]). However, our spectrum is recorded by using the 1.7 eV laser excitation and at 1.58 eV in Ref. [29]. Once more, an exact determination of the resonant energies would however require a full set of laser lines [28, 68, 69]. But the precise agreement between RBM frequencies for identified tubes in SDS or on a substrate with our data on free-standing tubes shows that the influence of the environment is small, at least in the diameter range where our data overlaps with the previous work. This raises questions on the interpretation of the B parameter as an environmental constant. We have so far no explanation for this experimental result.

The present combined electron diffraction and Raman scattering experiments on the same free-standing SWNT is a direct measurement of the relation between the RBM frequency and the tube diameter without modelisations of the vibrational and electronic properties. The main point of discussion concerns the dependence of the RBM frequency versus the tube diameter. For isolated tubes, the models predict a $\omega_{RBM} = A/d$ relation [64]. From the Raman experiments performed on SDS wrapped individual SWNTs [28, 68, 69], a $\omega_{RBM} = A/d + B$ relation was found. The non-zero value of the B parameter is commonly attributed to the effect of the environment. Again, most of the environmental influences are absent for the free-standing SWNTs investigated here. Thus, also the experimentally obtained RBM frequency vs. diameter relationship shows that the large value of B can not be attributed to the environment.

To elucidate more completely this point, investigations on well characterized (n,m) free-standing nanotubes of smaller diameter are required. The expected results will allow a direct comparison with more of the experimental results obtained from SDS wrapped individual SWNTs [68, 28, 69] and *ab initio* calculations [72].

5.3.2   TM range

It was shown by Cronin et al. [73, 74] that uniaxial strain has a significant influence on the TM frequencies, while no change is detected in the RBM frequencies. Strain could reasonably occur in some of our suspended nanotubes, by a small deformation of the free-standing structure. From our TM frequencies we conclude that uniaxial strain (if present) is much smaller in our samples than in [73, 74].

Figure 5.6 shows the TM features of several identified single-walled carbon nanotubes. All curves are well fitted by two lorentzian lines (one is sufficient for the (23,21)). The highest frequency ω_G^+ peaks for most of the nanotubes are grouped close to 1591cm^{-1}, which is the expected value for an unstrained tube. According to Cronin et al. [74], the slightly shifted peak for the (23,21) (at 1585cm^{-1}) corresponds to an uniaxial strain of 0.28%.

The separation between the two observed tangential mode frequencies ω_G^+ and ω_G^- decreases with increasing diameter. In Fig. 5.6 this trend is seen in the in-
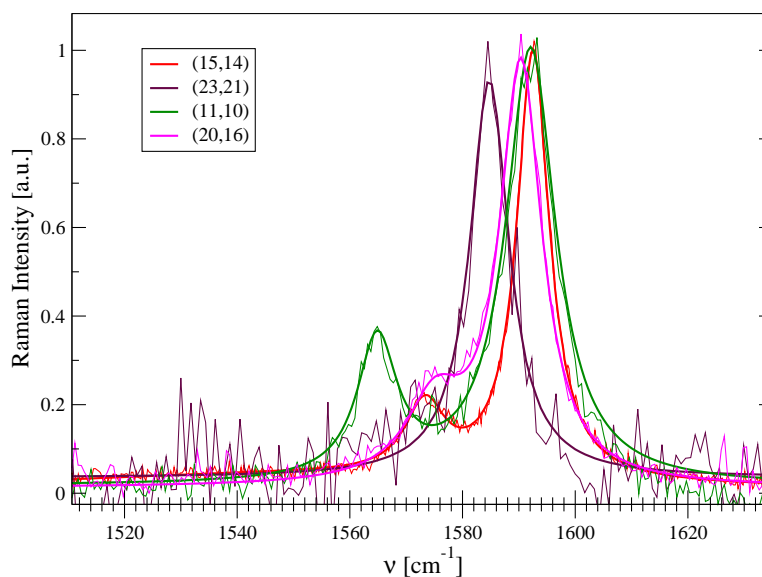
Figure 5.6: TM range of several identified SWNTs. The curves are normalized to the maximum peak height. All curves are well fitted by two lorentzian components. Shown in the indicated colour for each tube is the raw data (thin line) and the fit to two lorentzians (bold line).

creasing diameter sequence (11,10), (15,14), (20,16), and the two lines might not be separated any more in the single peak observed for the large (23,21) tube. This trend is in qualitative agreement with the G-band study of smaller diameter nanotubes in Ref. [75].

5.3.3   Transition energies

Although the transition energies can not be precisely determined with a small number of fixed laser lines, the observation of a detectable signal means that a transition energy of the nanotube is close to the laser energy. We can compare our excitation energies with calculated values. Fig. 5.7 shows the so-called Kataura plot together with the data collected on identified single-walled carbon nanotubes. This representation of the transition energies was first introduced by Kataura et al. for the interpretation of resonant Raman spectra [76]. Detailed calculations of the 1D electronic DOS are found in [77]. Tabulated data from these calculations can be found in [17]. The plot in Figure 5.7 is generated from this data. Highlighted in the plot are the calculated transition energies for the nanotubes in our data set. Given for comparison is the laser energy at which we obtained a signal. It appears that the laser energy is often slightly higher than a calculated transition. In all cases a calculated transition is present within 0.25eV below the experimental laser energy.

This systematic deviation of the transition energies from those calculated by
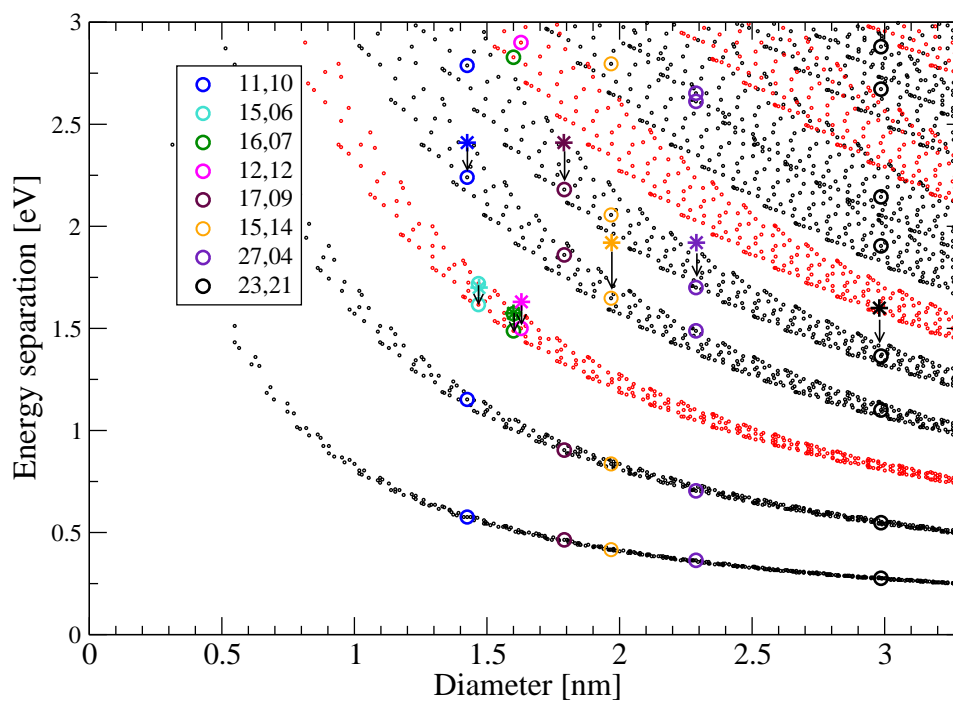
Figure 5.7: Comparison of our data with the Kataura plot. The small black and red points are the calculated transition energies respectively for semiconducting and metallic nanotubes. Marked with a circle are the calculated transition energies for the carbon nanotubes we have measured and identified. Given as star (*) in the same colour for each tube is the laser energy at which a Raman signal was observed. In all cases a calculated transition is found slightly below the laser excitation energy (within 0.25eV) as indicated by the arrow.

Kataura et al. confirms previous findings, e.g. by Telg et al. [28]. The index assignment in [28] is done by matching the Raman spectra to calculated transition energies and RBM frequencies via a pattern recognition approach. Although Telg et al. have investigated smaller diameter nanotubes, they found a similar systematic deviation from the calculated energies.

5.4 Conclusions

We have obtained Raman spectra of carbon nanotubes of which the structure was independently and unambiguously identified by electron diffraction. In this way we have directly measured the relation between the radial breathing mode frequency and the diameter of carbon nanotubes, while all previous measurements of this relation had relied on a modelization of vibrational and electronic properties of the carbon nanotubes.

Our measurements cover an unprecedented diameter range from 1.4 nm up to 3 nm, and confirm previously established more or less model dependent laws in the range 1.4-1.7 nm (which is the overlap with previous work). Indeed, it is surprising that we obtain the same radial breathing mode frequency for free-standing nanotubes as compared to nanotubes of the same diameter on a substrate or encapsulated in SDS micelles. This shows that the influence of the environment on the RBM frequency is much smaller than previously assumed.

Further, the diameter dependence of the tangential mode frequencies, and the deviations between measured and calculated transition energies, are in agreement with previous work. Since previous investigations were mostly done on nanotubes with smaller diameters than in this work, additional measurements on precisely identified smaller diameter nanotubes will allow a more quantitative comparison.

Chapter 6

Transport measurements in combination with electron microscopic analysis

The electronic characterization of an individual carbon nanotube is usually carried out by placing two lithographic contacts onto a nanotube which is adsorbed on a substrate. The diameter of the nanotube is estimated by Atomic Force Microscopy (AFM), but this technique does not allow to tell whether the measurement is performed on a small bundle or a single tube. If the true nature of the object under investigation is not known, the interpretation of such measurements has to depend on assumptions.

Recently, carbon nanotubes encapsulating fullerenes or endohedral metallofullerenes, so-called peapods, have attracted considerable interest. In the case of filled nanotubes, there is no way to know (with the previous methods) whether the particular nanotube on which the electronic transport measurements are performed is filled or not.

Therefore, it is highly desirable to obtain a Transmission Electron Microscope (TEM) image of the very same carbon nanotube on which the transport measurement has been carried out. A TEM image shows whether there is a single nanotube or a bundle, and it reveals the diameter and filling of the tube. The electron diffraction analysis yields the precise structure of the SWNT. Transmission Electron Microscopy, however, is not possible on objects on a bulk substrate.

None of the previous approaches for combining TEM and transport [78, 79] allowed for an electronic characterization of the nanotube in field-effect transistor (FET) configuration. However, it is the dependence of the current on the gate voltage that provides crucial information about the electronic structure of the carbon nanotube.

One major achievement presented in this chapter is the combination of a transport measurement in a transistor configuration with high-resolution images obtained from the same object. The transport measurement is done first, in a "stan-
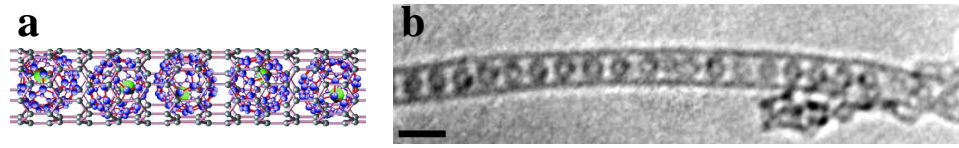
Figure 6.1: (a) Model of the endohedral peapod $Dy@C_{82}@SWNT$. The SWNT is filled with C_{82} fullerenes, each of which encapsulate a Dysprosium (Dy) atom. (b) High resolution TEM image of a $Dy@C_{82}@SWNT$ hybrid structure. The heavy Dy atoms are visible in several of the fullerene cages as dark spots. Scale bar 2nm.

dard" configuration with a back-gate and at liquid helium temperatures. After the transport measurement, the samples are processed further to facilitate a TEM investigation of the same object. In this way a complete electronic characterization can be combined with the detailed structural analysis from the electron microscopic investigation.

Another, more simple sample preparation is shown which does not provide the well-defined back-gate, but allows transport and electron diffraction on free-standing nanotubes. These samples also allow *in-situ* transport experiments in the transmission electron microscope. In this way we examine the influence of the electron beam on the tube and the contacts, and finally observe the failure of the nanotubes by high currents.

6.1   TEM and transport in a transistor configuration

The goal of this part was to measure the transport properties of nanotubes filled with fullerenes, so-called peapods. High-resolution TEM is a sure way to determine whether a measurement was performed on an empty nanotube or a filled one.

Here we are interested in transport measurements on nanotubes filled with endohedral metallofullerenes, annotated as $Dy@C_{82}@SWNT$. A charge transfer from the fullerene to the nanotube is expected to provide a "doping from the inside". A modulation of the band structure due to the fullerenes was clearly shown in scanning tunnelling microscopy and spectroscopy experiments [80]. The effect on the transport properties remains an open question. Previous transport measurements on this type of material [81] could not provide evidence that the measured nanotube was indeed filled. A TEM image as shown in Fig. 6.1b, if obtained from the same nanotube as the transport data, would be conclusive evidence that the measurement is indeed done on nanotube filled with fullerenes.

6.1.1   Experimental procedure

The transport investigations are carried out on highly doped ($\rho \leq 6m\Omega cm$) silicon substrates with a 200nm thermally grown silicon dioxide layer. A marker system,

consisting of 5nm Cr and 20nm Au is prepared by electron beam lithography on each sample. Laser-ablation SWNTs are purified by repeated oxidization and subsequent HCl treatment and filled with $Dy@C_{82}$ endohedral metallofullerenes [82], yielding so-called metallofullerene peapods [83, 84]. From TEM investigations, we estimate that 50% of the nanotubes are filled with fullerenes. The majority of the nanotubes is either completely filled or empty, but partly filled nanotubes were also observed. These SWNTs are suspended in a 1% aqueous solution of sodium dodecyl sulphate and adsorbed onto the substrates with the marker system. Atomic Force Microscopy (AFM) is used to locate potentially single nanotubes with respect to the marker system.

Now that the location of the nanotubes is known, a contact structure is designed for each nanotube. The contact structure is prepared on top of the carbon nanotubes in a second lithography step. Now the transport measurement is done, using the substrate as back-gate. Afterwards, a supporting metal structure is created in a third lithography step. It keeps the contacts in a fixed position relative to each other during the etching process. The free-standing structure is prepared using the previously described etching processes. Now the same nanotube can be investigated by high-resolution TEM. An example is given in Figure 6.2 which shows the AFM image, a TEM image of the suspended nanotube between its contacts, and SEM images of the etched structure.

6.1.2   Results

Figure 6.3 shows AFM and transport data of a carbon nanotube from (partially filled) nanotube material. From the AFM data, the tube diameter was measured as 1.5nm, and a single tube was expected. The transfer characteristic in Figure 6.3 was measured at 4.2K for $V_{sd} = +5mV$. We observe so-called ambipolar transport, i.e. the current I_{sd} through the bundle is suppressed for intermediate values of the gate voltage V_g, whereas large currents are flowing both for high positive and high negative values of V_g. The regime of suppressed current is $\Delta V_g \approx 2.0V$. This behaviour is similar to the previously reported measurement on (possibly filled) endohedral metallofullerene peapods [81].

After the transport measurement, the sample is etched and the free-standing tube is observed by TEM (Fig. 6.4). The TEM micrographs show a bundle composed of two single-walled carbon nanotubes, both with a diameter of $1.15\pm0.1nm$. Contrary to our expectation, no fullerene filling is observed. No twisting of the two nanotubes around each other is visible along the entire length. This implies that before etching the two nanotubes were lying parallel and next to each other on the substrate without overlapping or crossing. The substrate was orthogonal to the direction of the electron beam, and correspondingly the nanotubes appear at maximum separation orthogonal to the beam and do not overlap in the projection of the TEM images.
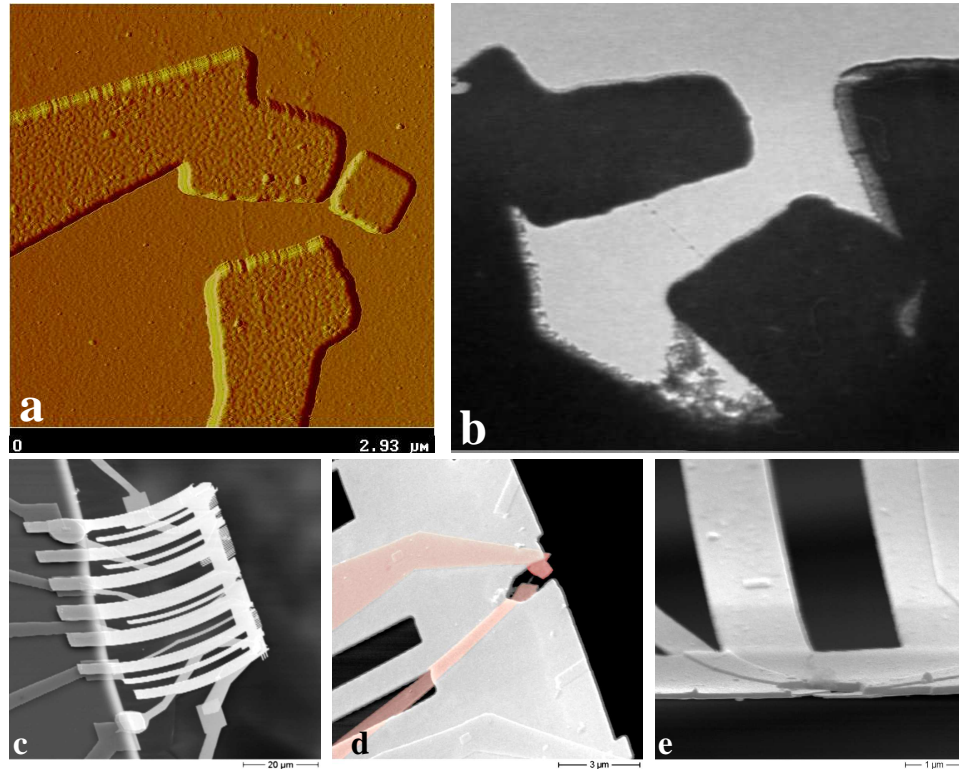
Figure 6.2: (a) AFM image of a contacted nanotube. The contacts are used for a transport measurement. Afterwards, a support structure is created and the sample is etched. (b) TEM image of the nanotube suspended between the same contacts. (c-e) SEM images of the free-standing structure. Image (d) is artificially coloured to show the different parts of the structure. Highlighted in red are the contacts which were used for the transport measurements, now embedded in the supporting structure.
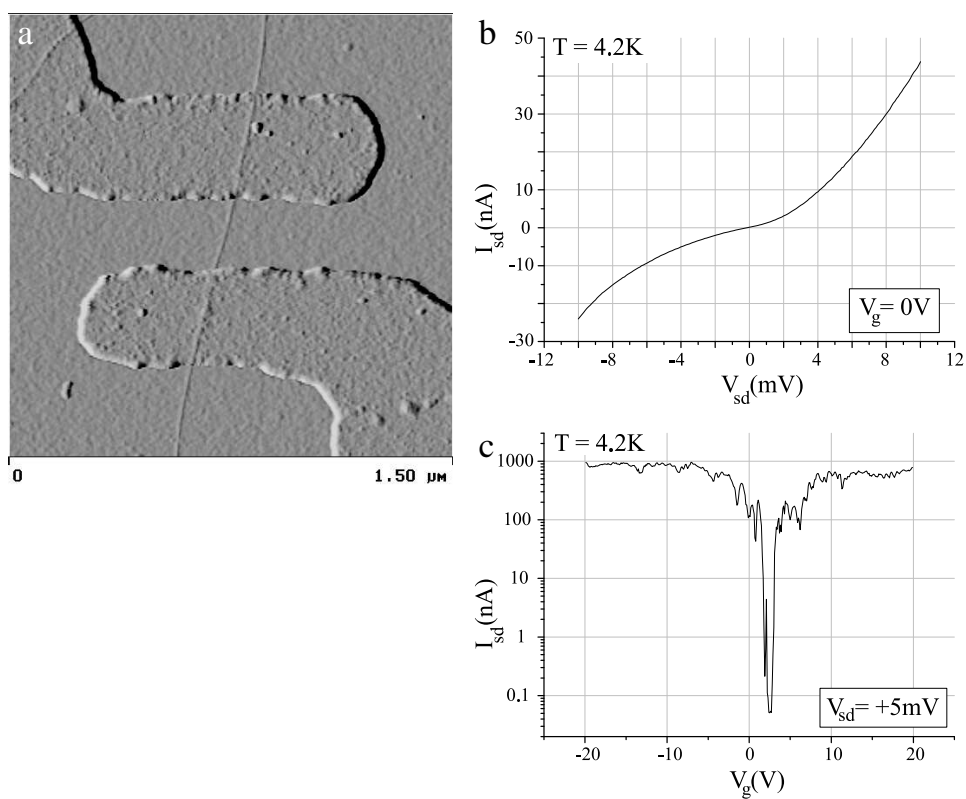
Figure 6.3: (a) AFM image of the contacted nanotube. (b) Output characteristic at $V_g = 0$V and (c) transfer characteristic at $V_{sd} = 5$mV, both measured at 4.2K.
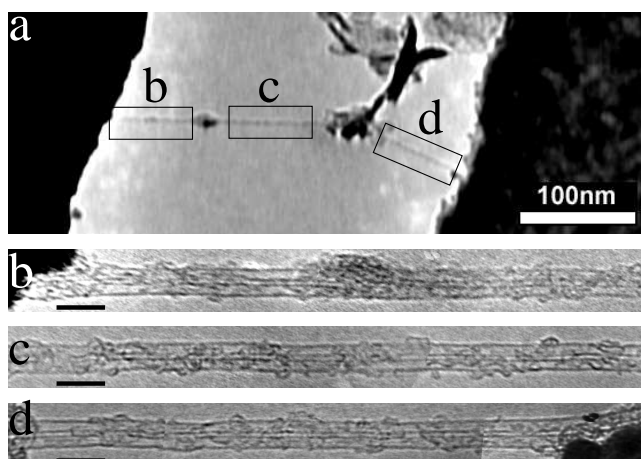

Figure 6.4: (a) TEM image showing the entire nanotube suspended between the its contacts. Some debris has accumulated due to a contamination in the etching process. (b-d) High-resolution images of the segments as indicated in (a). A bundle of two empty nanotubes is found. Scale bar in (b-d) is 5nm.

6.1.3 Discussion

Lee et al. have shown by Scanning Tunnelling Spectroscopy, that filling of SWNTs with endohedral metallofullerenes reduces the band gap significantly [80]. This band gap narrowing makes the observation of ambipolar transfer characteristics likely, as reported in [81]. However, band gap narrowing due to insertion of metallofullerenes can be ruled out for the bundle of tubes investigated within this study. The TEM images reveal that the two carbon nanotubes the bundle consists of are empty, and also that their diameters are too small to allow a filling with $Dy@C_{82}$.

To estimate the band gap E_{g} of the investigated SWNT bundle, it is required to know the coupling factor $\alpha = C_{\mathrm{g}}/C_{\Sigma}$, where C_{g} is the capacity between the SWNT and the gate electrode and C_{Σ} the total capacity of the nanotube with respect to the metal electrodes and the gate. With a given α the band gap E_{g} is obtained by $E_{\mathrm{g}} = \alpha\,\Delta V_{\mathrm{g}}\,e$. Within this study a carbon nanotube which was not treated with the fullerene filling method exhibited Coulomb blockade behaviour at 4.2K which allowed to extract $\alpha \approx 0.2$ from the diamond plot. Similar values for α have been reported by other authors [85]. Assuming the same α for the nanotube bundle investigated here results in a band gap of $E_{\mathrm{g}} \approx 400$meV. For the tube diameter of 1.15 nm the predicted band gap [16] is $E_{\mathrm{g}} = 309$meV, in reasonable agreement with the value deduced from the transport measurements.

Of course, $\alpha = 0.2$ is only a crude estimate, and α can be different for different carbon nanotube field effect transistors, even if they are prepared in the same way. The smallest value of α we have found in the literature is $\alpha = 0.05$ [86], which would lead to $E_{\mathrm{g}} \approx 100$meV, too small for the gap of a semiconducting nanotube and too large for a curvature-induced small band gap in a "quasi-metallic" SWNT [87, 88].

Fig. 6.5 shows a TEM image of another nanotube bundle on which transport measurements were carried out. Unfortunately only a partial filling is observed. It is therefore not clear whether the properties of the filled or empty nanotubes dominate the electronic properties. We have not (yet) achieved a measurement on an isolated filled single-walled carbon nanotube peapod. The material is strongly bundled, and only partially filled. Tubes suspected to be single, based on the AFM analysis, often turned out to be small bundles. However, the procedure is developed up to a point where a TEM analysis of our transport samples can be reliably done, and will be a matter of preparing sufficiently many samples in order to find an individual peapod.

6.2 Diffraction and transport in free-standing tubes

A procedure for an efficient preparation of free-standing carbon nanotubes for TEM and transport investigations has been developed. In contrast to the method described above, it requires only a single lithography step, and the structure can be mass-produced, i.e. it is not required to prepare a different structure for each sample. No time-consuming searching for carbon nanotubes by AFM is required
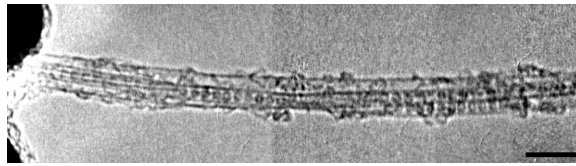
Figure 6.5: Example of a nanotube bundle on which transport measurements were carried out, but which is unfortunately only partially filled. Scale bar is 5nm.

(the AFM part in this process is a check and a manipulation on a small section). These samples are also used for the in-situ experiments shown in section 6.3. The TEM information is available *before* the nanotube is selected for the transport measurement. However, the gate effect by the nearby substrate is smaller compared to the previously described approach.

6.2.1   Sample preparation

A grid structure consisting of 3nm Cr and 110nm Au is prepared on top of CVD-grown carbon nanotubes. The sample is cleaved in such a way that the grid is on the edge of the sample. The previously described etching process produces a partly free-standing structure. Some contacts in the structure can readily be used for a transport measurement in case a nanotube is suspended between them. However, it turned out that the probability for obtaining exactly one of the randomly located nanotubes between two contacts is low. Since there is only limited space for bond pads, it is not possible to have a large number of prefabricated contacts in this way.

Instead, many potential contacts are arranged in a grid structure, but only some have a connection to a bond pad. A thin short-circuit bridge connects all contacts. Since the free-standing structure can be investigated by TEM, it is possible to locate an individual nanotube for the transport measurement within the grid. The bridge which short-circuits this specific tube is then opened using the AFM (Fig. 6.6).

At the same time as opening the short-circuit bridge, the AFM is used to make sure that no additional tubes are present between the contacts above the substrate. The free-standing part of the structure can be seen by TEM, but the part above the substrate can not. It is important to make sure that the measurement is done on precisely the one nanotube that was found in the free-standing part. Figure 6.7 shows connected AFM images of the region between the contacts, and the bridge before and after opening. The metal bridge has a width of ≈ 150nm, thin enough to be completely under-etched during the etching process. After etching, it is a free-standing metal bridge. Therefore it is easily opened by pushing it sideways with the AFM tip.

As a result we obtain free-standing individual single-walled carbon nanotubes with metal contacts. A TEM and electron diffraction analysis as well as a transport measurement can now be carried out on the same nanotube.
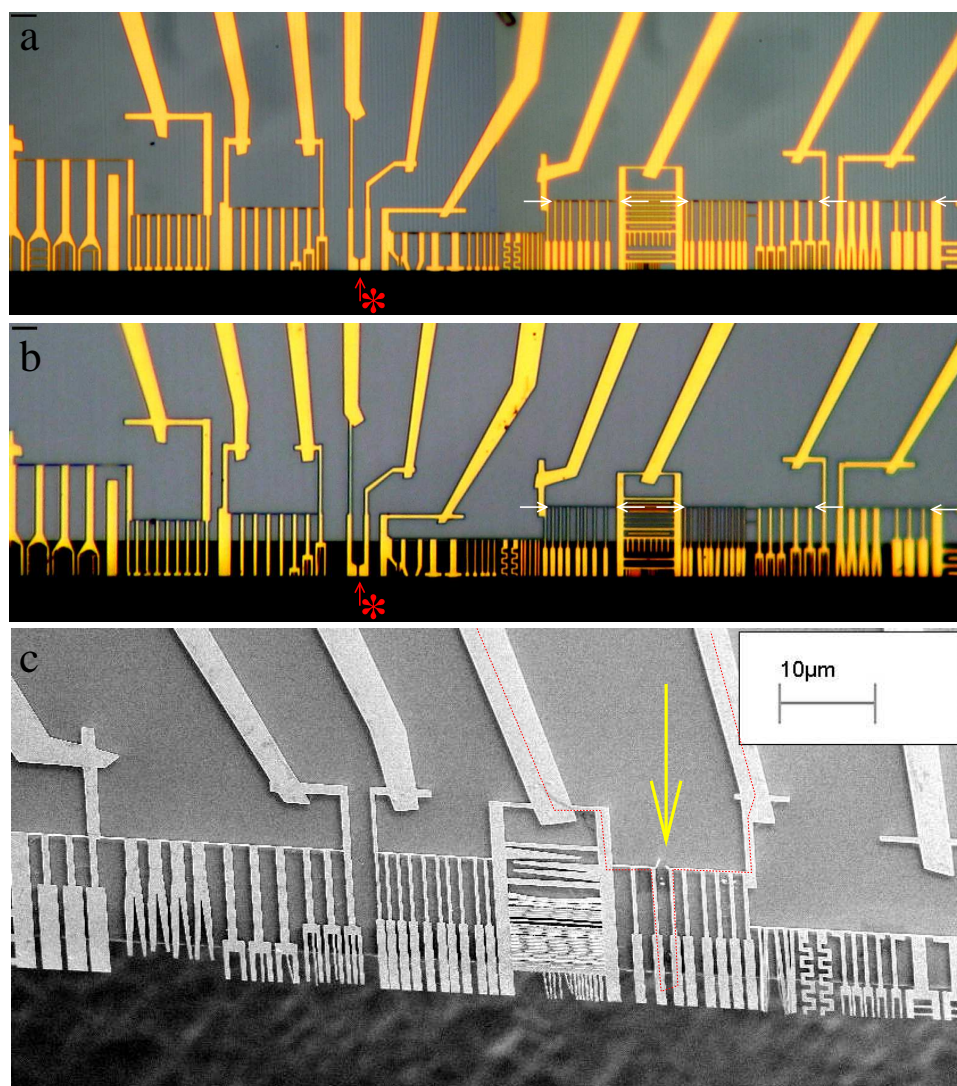
Figure 6.6: Optical microscope image of the structure before (a) and after etching (b). The two contacts indicated by the red arrow with the (*) can be readily used for a transport measurement in case a carbon nanotube bridges the gap. If not, a single nanotube is usually found somewhere in the remaining free-standing grid structure. This nanotube can be contacted by opening the small metal bridge at the end of the grid (some are indicated by the white arrows in (a) and (b)) at the right position. These bridges short-circuit all contacts, except those where the bridge is opened by pushing with the AFM tip. (c) is an SEM image of a free-standing structure. Here, one of the bridges was opened by AFM (indicated by the yellow arrow). The red dotted line indicates the path of the current in a transport measurement on a nanotube suspended within the free-standing structure. Scale bars in (a) and (b) are 5μm.
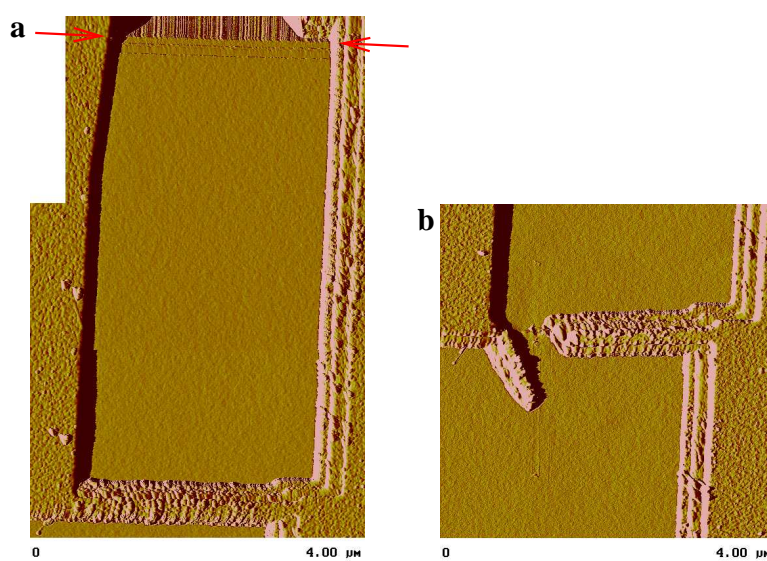
Figure 6.7: (a) AFM images of the region between the contacts. The red arrows indicate the edge of the substrate, with the free-standing part above. The AFM images show that no additional tube bridges the contacts above the substrate (where it can not be seen by the TEM). The metal bridge (which is free-standing after the etching procedure) is at the lower end of the image. (b) AFM image of the bridge after opening. The bridge is opened by pushing with the AFM tip.
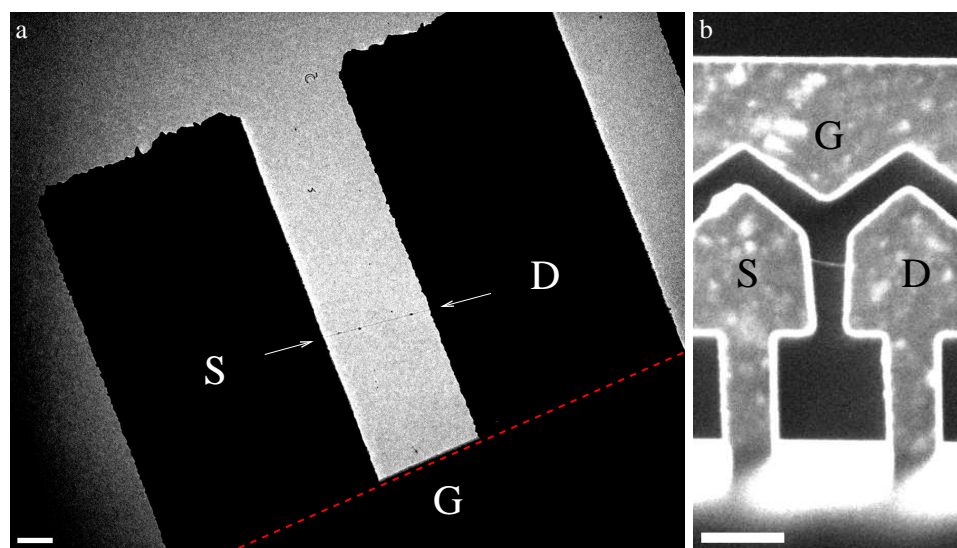
Figure 6.8: (a) Individual (14,10) single-walled carbon nanotube suspended between metallic contacts. The nearby substrate serves as gate. The dashed red line indicates the edge of the substrate (gate), with the source and drain contacts reaching out across the edge. (b) Dark-field TEM image of a (15,15) nanotube with metal contact structure. In this sample, a third metal electrode serves as side-gate. Scale bar 200nm (a) and 1μm (b).

6.2.2   Experimental

Several free-standing nanotube samples were prepared as described above. Successful transport measurements were carried out on carbon nanotubes identified as (13,09), (45,18), (10,10), (14,10), and (15,15). The (13,09) and (45,18) nanotubes were electrically measured *in-situ* in the TEM, with and without irradiation, as described in section 6.3. The in-situ measurements are carried out at room temperature in the ultra-high vacuum of the microscope. The (10,10), (14,10) and (15,15) were measured in a liquid helium atmosphere at 4.2K; and also various temperatures between 4.2K and room temperature in case of the (10,10) and (14,10).

If a third electrode or the highly doped substrate is close enough to the nanotube, it can serve as gate, and the tube can be analyzed in transistor configuration. This provides significantly more information about the nanotube than only the current-voltage characteristics. As shown in Fig. 6.8a, the (14,10) nanotube was prepared close to the substrate, which could be used as gate. The structure containing the (15,15) nanotube was designed to have a metallic gate electrode at one side (Fig 6.8b).
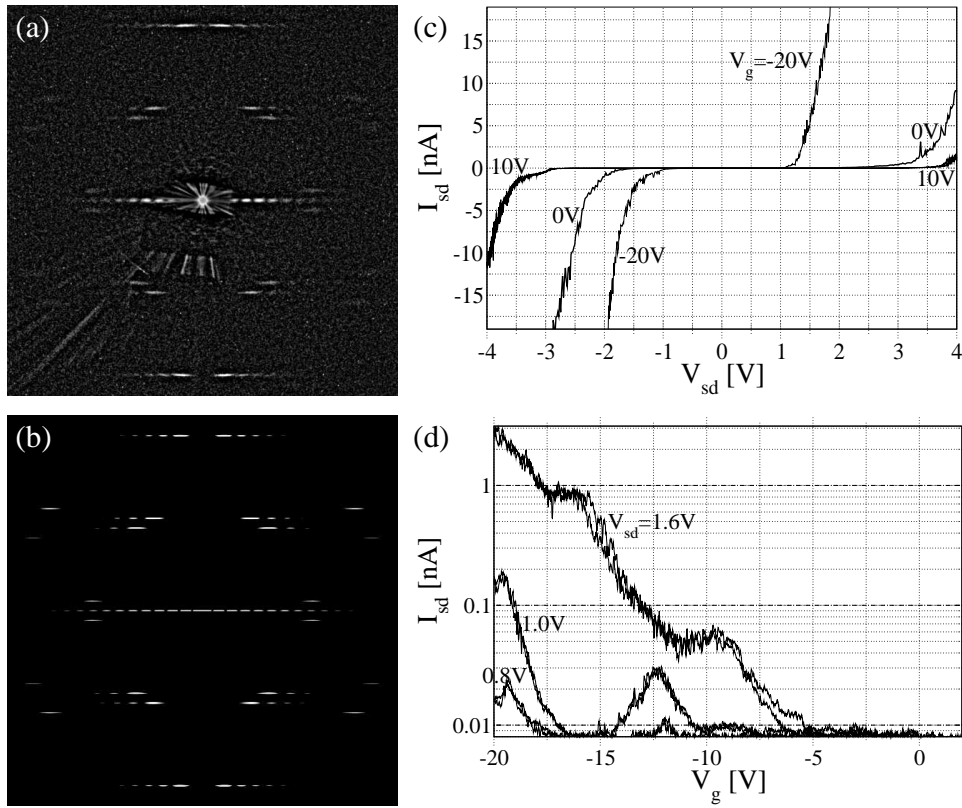
Figure 6.9: (a) Experimental and (b) simulated diffraction pattern of the (14,10) carbon nanotube (from Fig. 6.8a). (c) Output characteristics of the same nanotube for different gate voltages V_g. (d) Transfer characteristics (gate dependence) of the (14,10) nanotube at different bias voltage. Both (c) and (d) show the expected behaviour of a semiconducting nanotube.

6.2.3 Results

The complete transistor characteristics of identified (14,10) and (15,15) carbon nanotube were measured, i.e. the current-voltage characteristics for various gate voltages, and the gate dependence of the current for different bias voltages. For the (14,10) carbon nanotube, Fig. 6.8a shows a TEM image of the nanotube with its contacts, and Fig. 6.9 shows the diffraction pattern (from which the indices were derived) together with the transport data. For the (15,15) nanotube, the contact configuration is shown in Fig. 6.8b, and the diffraction and transport data in Fig. 6.10. These transport measurments were carried out at 4.2K.

Further, the electronic properties at various temperatures between 4.2K and 293K were measured for the (14,10) and a (10,10) nanotube. Current-voltage (I-V) plots at various temperatures for these tubes are shown in Fig. 6.11.
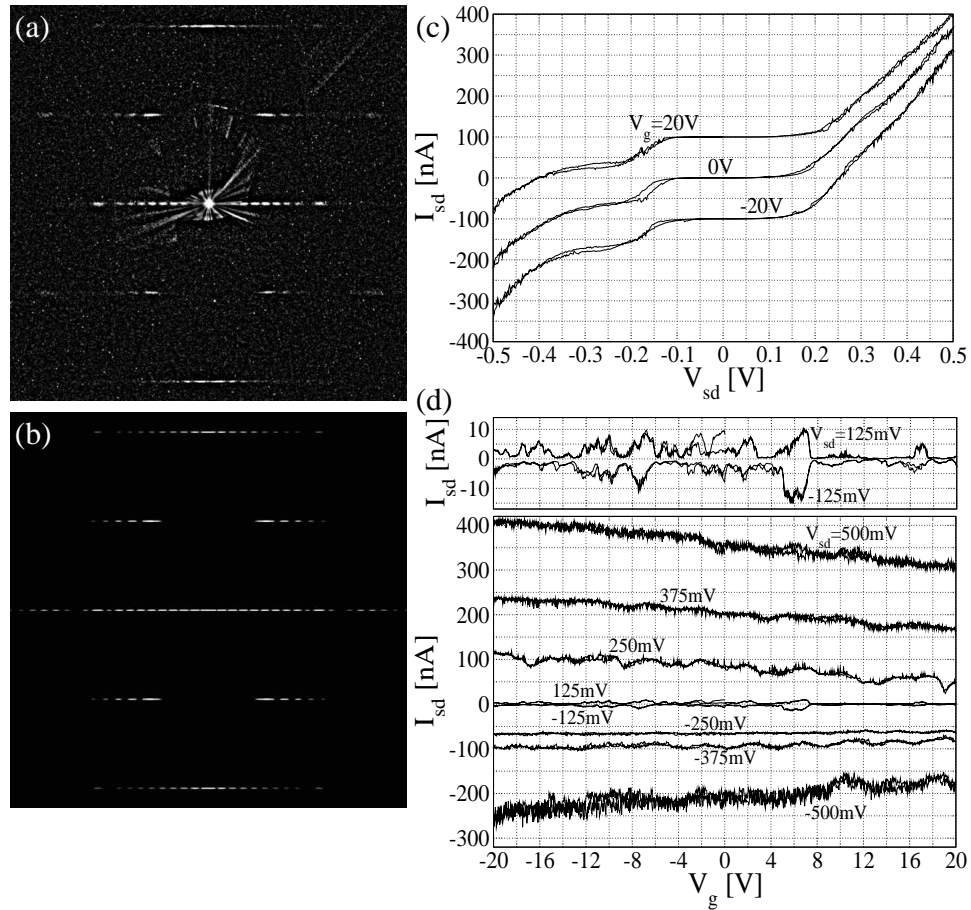
Figure 6.10: (a) Experimental and (b) simulated diffraction image of a (15,15) carbon nanotube (Fig. 6.8b). (c) Output characteristics of the same nanotube, for different gate voltages V_g . The lines are offset by 100nA in vertical direction. (d) Transfer characteristics (gate dependence) of the (15,15) nanotube at different bias voltages V_{sd}. At low bias voltages within the blockade regime ($\pm$125mV, enlarged), reproducible variations in the current as a function of gate voltage due to charging effects are observed, showing the effectiveness of the gate. At higher bias, the clearly metallic behaviour expected for a (15,15) nanotube is found.
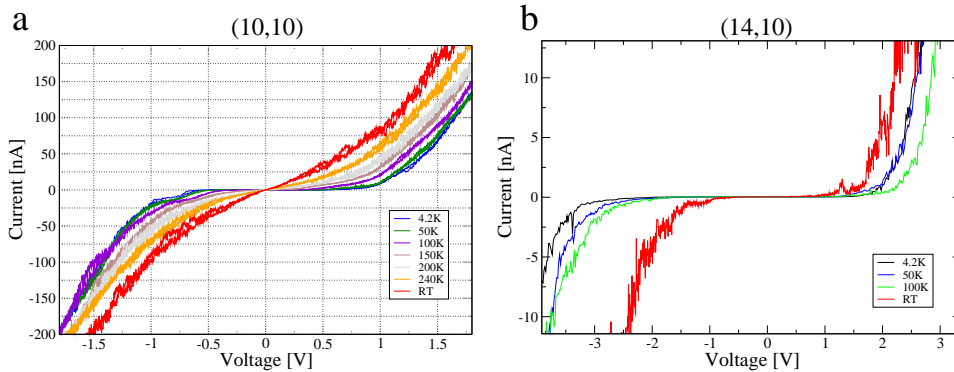
Figure 6.11: Current-voltage characteristics at varying temperature (a) for the (10,10) and (b) the (14,10) SWNT. The metallic (10,10) SWNT displays a suppression, due to coulomb blockade effects, up to 50K, and nearly linear behaviour at room temperature. The semiconducting (14,10) shows a suppression, of different width, at all temperatures. This it can be explained by the semiconducting gap at room temperature, and additionally coulomb blockades at low temperature.

6.2.4   Discussion

According to the structural indices, the (14,10) carbon nanotube is expected to be semiconducting with a band gap of 0.5eV [77, 17]. Similarly, metallic behaviour is expected for the (15,15). The (15,15) nanotube is of the so-called "armchair" type for which no curvature-induced small band gap [18, 19] is expected.

The current-voltage (I-V) characteristics at 4.2K of both nanotubes, at zero gate voltage, exhibits a wide suppression. This an indication of coulomb blockade behaviour, which is also evident in the gate dependence. Contacts made from chromium and gold are known to form high-resistance contacts to carbon nanotubes. In case of the semiconducting nanotube, there is additionally a Schottky barrier formed at the nanotube-metal interface. The observed suppression is clearly wider for the (14,10) nanotube as compared to the (15,15).

The I-V curves of the (15,15) nanotube (Fig. 6.10) do not depend on the gate voltage. The width of the suppression changes only slightly. The asymmetry in the I-V curves points to an asymmetry in the contacts. Also the variation of the current as a function of gate voltage agrees well with the behaviour predicted for a metallic carbon nanotube. At low bias (± 125mV), just above the suppression region, reproducible variations in the current appear as the gate voltage is varied. These are coulomb blockade effects, and they demonstrate that the gate does indeed have an effect. At all higher bias voltages, the current through the nanotube is nearly independent of the gate voltage. Although there is a (small) variation of the current with the gate voltage, this behaviour is in good agreement with the expectations for a metallic carbon nanotube.

A very different behaviour is observed in the (14,10) nanotube (Fig. 6.9). The
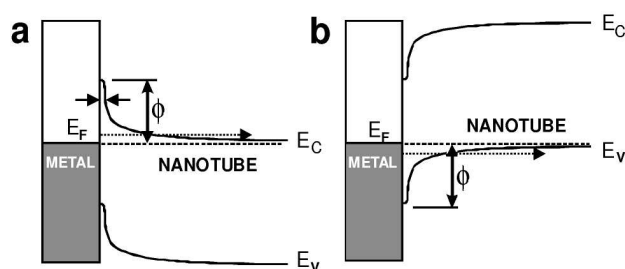
Figure 6.12: Schematic of a nanotube-metal Schottky barrier (from [89], modified). (a) electron conduction regime and (b) hole conduction regime. Due to the p-doping of nanotubes under ambient conditions, and the weak coupling to the gate in our free-standing tube devices, only the hole-conduction regime can be reached.

I-V curves are strongly modified by the gate potential. The width of the suppression at 4.2K is smaller for negative gate voltages, and increases for positive gate voltages. This nanotube clearly behaves like a p-type semiconductor. This picture is confirmed by the gate dependence of the current at a fixed bias. For small bias, there are again maxima in the current (as a function of gate voltage), due to coulomb blockade. At larger bias voltages, a clear p-type semiconducting behaviour of the nanotube is found.

Even for a precisely identified carbon nanotube, the transport behaviour can be understood only if the effects of the nanotube-metal interface (the contacts) are considered. Measurements at different temperatures help to elucidate this point. For the metallic (10,10) tube, ohmic behaviour is found at room temperature, while a coulomb blockade suppression is present below 100K. Also the (45,18) tube (Fig. 6.17, one of the in-situ measurements) exhibits a nearly linear, ohmic behaviour at room temperature.

In contrast, our two semiconducting tubes, the (13,09) (Fig. 6.17) and the (14,10) at $V_g = 0V$, show a wide suppression at room temperature. Transport on the semiconducting nanotubes here is suppressed (a) by the Fermi level being between the conduction and valence band edges (transistor is in the "off" state), and (b) by Schottky barriers at the metal-semiconductor interface. We can tune the (14,10) nanotube to the "on" state for hole conduction by applying a gate voltage of $-20V$ (Fig. 6.12b). Now, the transport is dominated by the Schottky barriers. At low temperatures (and low bias) the current is dominated by tunnelling through these barriers, while thermal activation is dominant at higher temperatures. From I-V curves at at different temperatures, each with a gate potential of $-20V$, we can derive the activation energy for transport across these barriers.

Thermally activated transport across a barrier of finite height is described by a temperature dependent current

$$I \sim \exp\left(-\frac{E_\mathrm{a}}{k_\mathrm{B}T}\right) \tag{6.1}$$

where k_B is Boltzmann's constant, T the temperature, and E_a the activation energy which describes the height of the barrier. We can estimate the height of the barrier from transport measurements at several temperatures. The shape and height of a Schottky barrier depends on the bias [90]; we will thus measure the activation energy for several small bias voltages and extrapolate to zero bias. The extrapolation is done assuming that the height of the Schottky barrier Φ depends on the bias as

$$\Phi = \Phi_0 - \alpha \cdot V_{sd}^2 \tag{6.2}$$

(after [90]), where Φ_0 is the height of the undeformed barrier at zero bias.

Fig. 6.13 shows the temperature dependence of the current through the (14,10) SWNT for different bias voltages. It is plotted as the logarithm of the current vs. the inverse temperature, so that the slope is $-\frac{E_a}{k_B}$ according to equation (6.1). In these so-called Arrhenius plots, we observe two distinct temperature ranges: The current at low temperature is dominated by tunneling, and thus temperature independent, while thermally activated transport dominates at higher temperatures. The measured slopes in the thermally activated regimes are extrapolated towards $V_{sd} = 0$, yielding $\frac{E_a}{k_B} \approx 340\text{K}$ for the undeformed Schottky barrier. We thus obtain a height of $\Phi_0 \approx 30\text{meV}$ for the Schottky barrier.

It should be noted that this activation energy value is only a rough estimate of the height of the Schottky barriers, as it includes a contribution from the coulomb charging energy which varies with gate voltage. Similar values were obtained on carbon nanotubes that were not etched, and are not free-standing, but contacted with the same metal [91]. This indicates that the contact interfaces are not influenced by our etching process. Lower activation energies were measured e.g. for titanium contacts [89]. It is worth noting that, even though we are analyzing the interface between a single molecule and a metal contact, the Schottky barrier description for bulk semiconductors (as in [90]) applies reasonably well: The concept of thermally activated transport is, of course, not specific to the Schottky barrier. But the bias-dependent deformation of the barrier (Equation 6.2), which is modelled for a conventional Schottky junction (after [90]), does fit surprisingly well the observed behaviour as evidenced by the experimental points falling on the straight line in the inset of Fig. 6.13.

6.3 In-situ transport experiments

With samples prepared as described in 6.2.1, it is also possible to do transport measurements *in situ* in the transmission electron microscope. In this way we observe the effect of irradiation on the tube and contact properties, and the effect of high currents on the tube up to its failure.
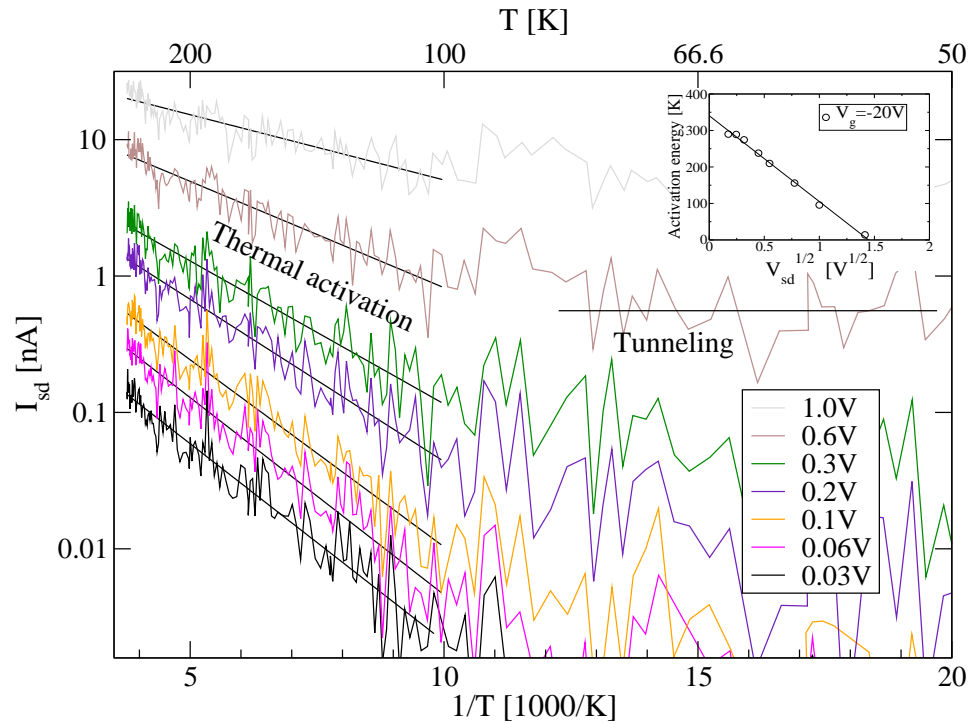
Figure 6.13: Temperature dependence of the current through the (14,10) SWNT, at different bias voltages. All measurements were done at a gate voltage of $V_g = -20$V. The source-drain bias voltage for each line is given in the legend. The two regimes of thermally activated transport across the Schottky barrier at higher temperatures, and temperature independent tunnelling through the barrier at lower temperatures, can be clearly distinguished (the temperature independent behaviour continues down to 4.2K). The slope in the thermally activated region is the activation energy divided by k_B. The inset shows the slope vs. square root of the bias voltage. The extrapolation to $V_{sd} = 0$ gives the height of the undeformed barrier. The abscissa is 340K, corresponding to an activation energy for the undeformed barrier of 30meV.
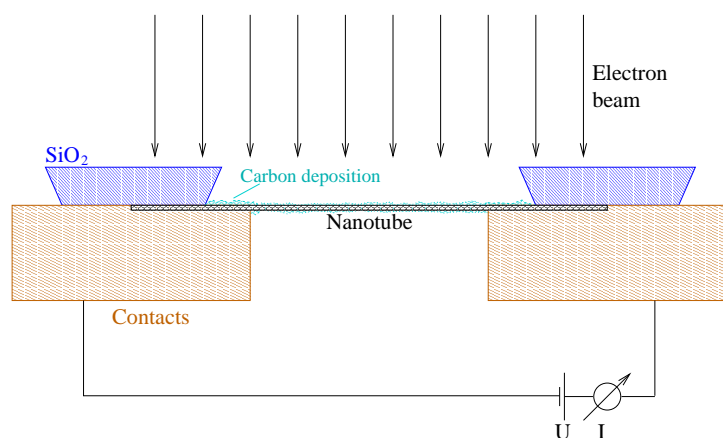
Figure 6.14: Schematic of the in-situ transport measurements. The electrically connected nanotube is irradiated and imaged in the transmission electron microscope during the transport measurement. The irradiation can also be limited to the tube or the contacts. In all experiments, an electron beam induced deposition of carbon around the nanotube and contacts is clearly observed (depicted in cyan).

6.3.1 Experimental set-up

The samples are carefully mounted and connected to a TEM sample holder which has electric connections to the outside for up to four contacts. These are connected on the outside to the same PC controlled hardware for transport measurements as used in the ex-situ transport measurements. We can now measure the current vs. voltage with and without electron irradiation, or a time dependence of the current at a fixed bias. The back-gate can not be used, since the bulk of the sample is electrically connected to the reference potential due to the way it is mounted.

Figure 6.14 shows a schematic of the in-situ transport set-up. In three of the four samples, the nanotube and contact structure is nearly orthogonal to the beam, one sample is mounted so that the tube is nearly parallel to the beam. The samples can be imaged and irradiated during the transport measurement, or the beam can be blanked for reference measurements. All measurements are carried out at an acceleration voltage of 60kV, which is below the threshold for knock-on damage in carbon nanotubes. We therefore expect no structural damage to the tubes. Finally, the samples were destroyed by slowly increasing the bias, while capturing a series of images at the same time to observe the current-induced failure of the nanotube.

6.3.2 Sample description

Of the four samples measured in-situ, one sample comprises SWNT bundles while the other three contain precisely one individual nanotube between the contacts. Sample 1, shown in Fig. 6.15, comprises three small bundles of carbon nanotubes
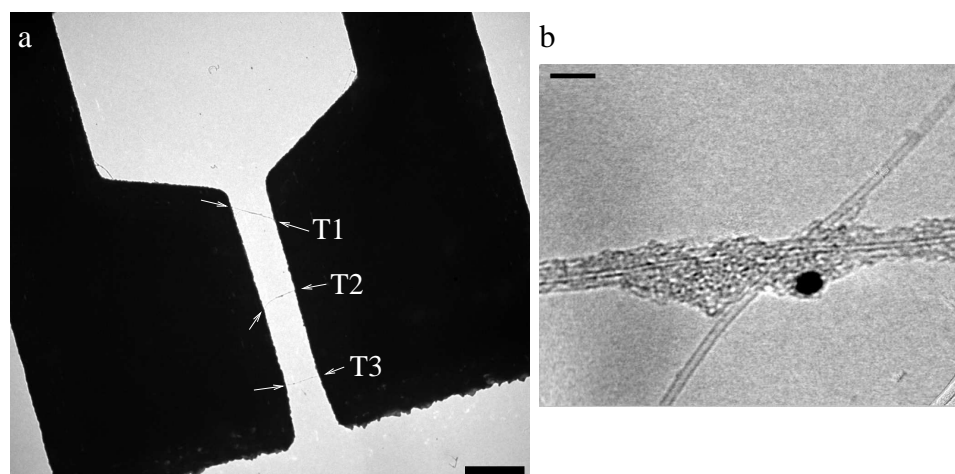
Figure 6.15: (a) Three small bundles are present in sample 1. We will refer to them as Tubes 1, 2 and 3 (or T1, T2, T3) as indicated in the image. No high-resolution images of the transport tubes T1-T3 were taken prior to the experiment to avoid irradiation damage. (b) A typical nanotube bundle from a similar sample (same CVD growth), intersecting with a single nanotube. Mo/Co catalyst particles are frequently attached to these tubes. Scale bars are 500nm (a) and 5nm (b).

bridging the contacts. Figure 6.15a shows the sample before beginning the transport measurements.

Samples 2-4 contain individual single-walled carbon nanotubes (the tube in sample 2 is partly a DWNT). Sample 2 contains a very long (4.2μm) nanotube, and a diffraction analysis was done on three points of the tube. It shows that it is a large-diameter SWNT on two thirds of the length, and a DWNT in the remaining part. The orientation of the SWNT is present on the full length, showing that there is one continuous (45,18) nanotube shell on the full length. Additionally there is a smaller tube inside on 1/3 of the length. Since it is the outer shell of the DWNT which continues to the SWNT section, and the contacts are also on the outer shell, we ignore the partial inner tube in the analysis of the transport measurement. A TEM image of the sample and diffraction images are shown in Figure 6.16.

Sample 3 also contains an individual SWNT. No diffraction analysis was done on this nanotube. Sample 4 contains an individual single-walled carbon nanotube identified as (13,9), with contacts at a distance of 420nm.

6.3.3   Transport behaviour before electron irradiation

Initial measurements were performed on all samples without electron irradiation. Before these initial measurements, the samples have been exposed to only small doses of radiation, compared to the doses leading to observable effects as shown
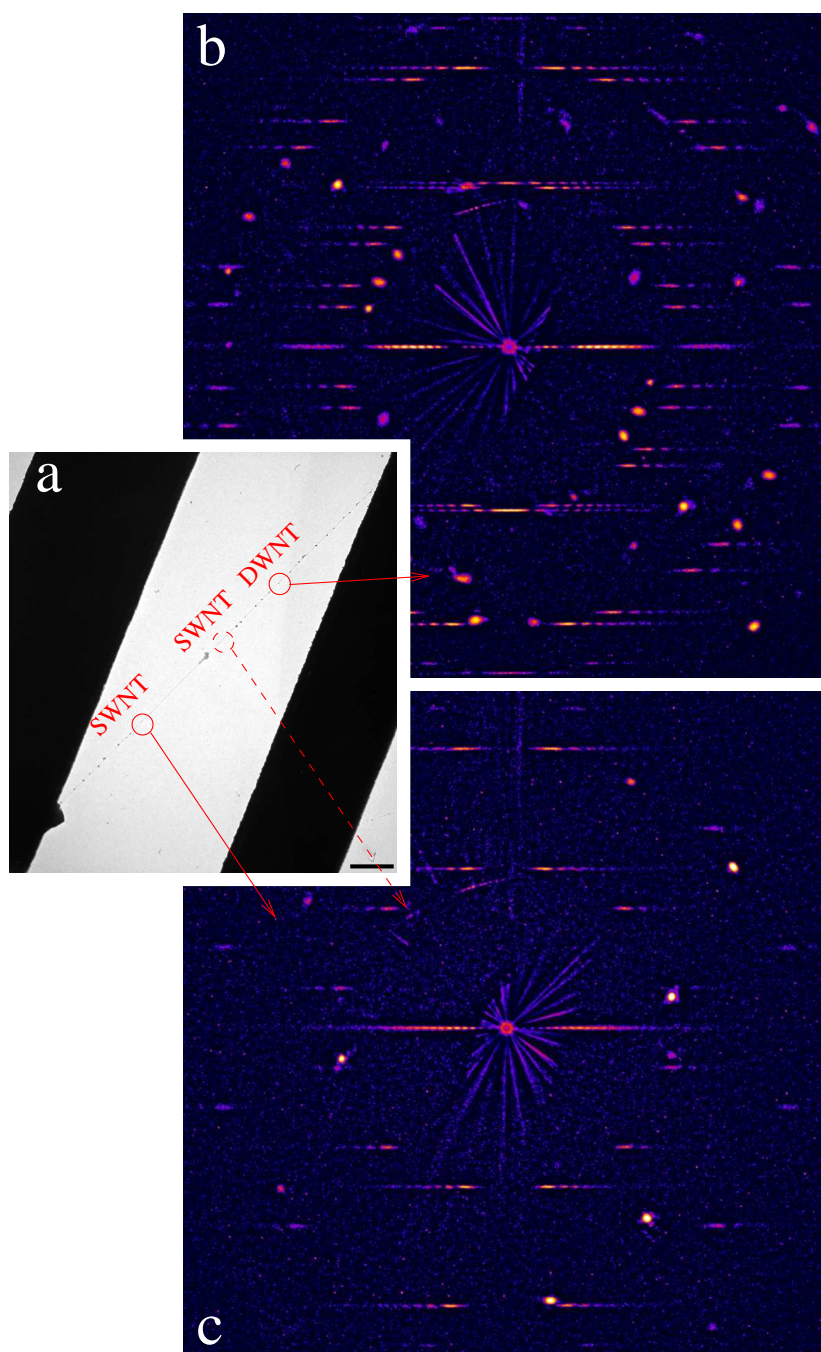
Figure 6.16: (a) TEM image of nanotube and contacts in sample 2. Diffraction patterns were obtained from three points of the tube, showing that it is a large-diameter (45,18) SWNT (c) on part of the length, and a DWNT (b) in the remaining part. The regions from which the diffraction images (b) and (c) were obtained are marked by red circles. The diffraction image obtained from the region indicated by the dashed line is not shown, it is similar to image (c). The graphene orientation in the SWNT (c) continues in the DWNT section (b). It shows that this tube contains one continuous (45,18) nanotube shell, partly as outer shell of a DWNT. Scale bar in (a) is 400nm.
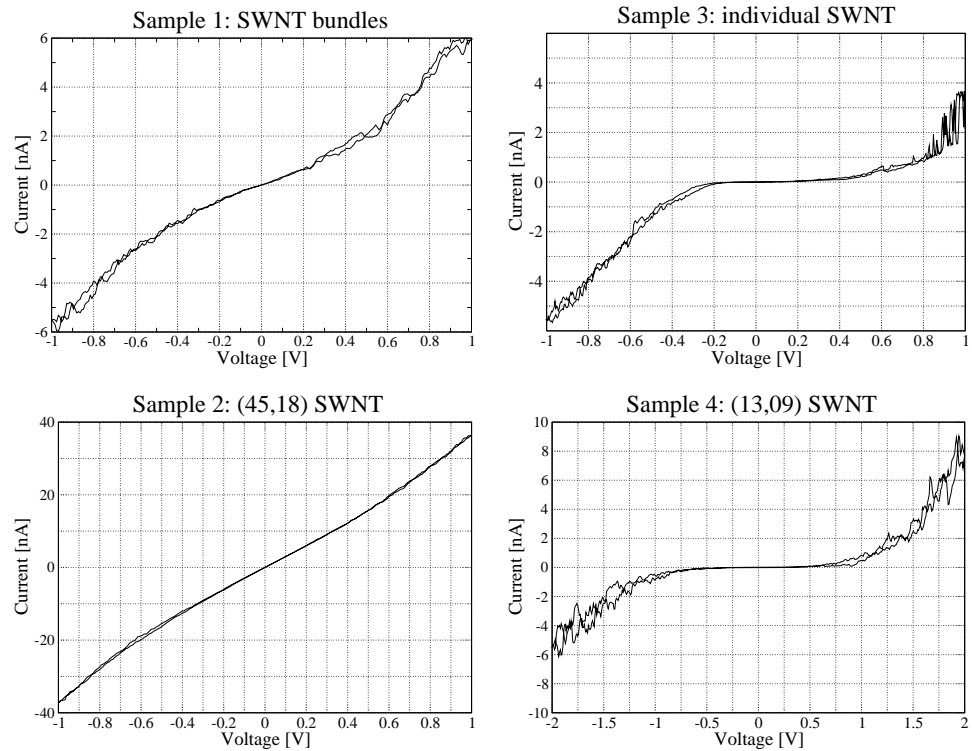
Figure 6.17: Measurements before electron irradiation. The SWNT bundles (sample 1) and the large diameter metallic SWNT (sample 2) exhibit a nearly linear behaviour at small voltages. Both the unknown SWNT (sample 3) and the semiconducting (13,09) nanotube (sample 4) show a wide suppression in the current-voltage plot. All measurements are at room temperature.

later. This was required for locating the nanotubes in the grid structure, and for the diffraction analysis in samples 2 and 4.

Figure 6.17 shows the initial current vs. voltage (I-V) characteristics. The individual metallic nanotube and the bundles (which are likely to contain metallic as well as semiconducting tubes) present a nearly ohmic behaviour. Sample 1, with its three bundles, has initially a contact resistance of $200\text{M}\Omega$. However, it is not (yet) clear how the current is distributed between the three nanotube bundles. The large-diameter metallic (45,18) nanotube in sample 2 shows a resistance of $32\text{M}\Omega$.

The individual nanotubes in samples 3 and 4 exhibit a wide suppression in the I-V curve. This behaviour can be attributed to Schottky barriers between metal contacts and a semiconducting object. We know that tube 4 is a (13,09) tube which is semiconducting according to the indices. The very similar behaviour of samples 3 and 4 indicates that sample 3 also contains a semiconducting nanotube.

6.3.4 Transport behaviour with electron irradiation

Electron irradiation at an acceleration voltage of 60kV, below the limit for knock-on damage, leads to an increase in conductivity. We observe a significant effect only if the contacts are irradiated, not if the beam is limited to a free-standing nanotube segment.

Figure 6.18 shows the increase in conductivity in samples 1-3. In all samples, the conductivity increases by one or two orders of magnitude during the course of the experiment. We point out that the samples are irradiated while a voltage is applied (and the current is measured) at the same time, typically with a current of a few tens of nA through the nanotube. The increase in conductivity can be observed as a current increase over time during irradiation (Figure 6.18b), or during repeated cycling of the voltage (Figure 6.18a, c, d) with irradiation during some of the cycles.

The conductivity increase could be attributed to an electron beam induced deposition of carbon that is "soldering" the tubes to the contacts. However, there are several indications that the current plays a role in the contact modifications: The electronic properties keep changing even after the irradiation is switched off, as e.g. seen in Fig. 6.18b. In the I-V plots, we find that the properties still change during the first cycle after irradiation, while the second and further cycles are reproducible (Fig. 6.18d). This is a clear indication that the deposited carbon is further modified by the electric current.

Further, we observe strong noise-like variations in the conductivity of bundles and individual semiconducting nanotubes during irradiation, while this effect is not found in the metallic tube. An example is shown in Fig. 6.19. The variations are visible only if the contacts are irradiated, not if the beam is limited to the free-standing section of the nanotube. A possible explanation is that localized charges close to the semiconducting tubes are induced by the electron beam, for example in the silicon dioxide layer (Fig. 6.14). These varying charges would modulate the conductivity of semiconducting tubes. This effect may also lead to the switching effect observed in one device as described below (section 6.3.6).

6.3.5 Observation of nanotube breakdown

6.3.5.1 Sample 1 (Fig. 6.15)

The first indication that most of the current in this sample flows through the tube T2 (Fig. 6.15a) stems from the current fluctuation during irradiation. We apply a fixed bias of 1V and focus the electron beam onto different sections of the sample. We observe large fluctuations in the current *only* if the Tube T2 *and its contact region* is irradiated. Figure 6.19 shows this measurement.

The assumption that tube 2 carries the largest portion of the current is confirmed by the final measurement, where the bias is increased until the tubes break down. We observe that T2 breaks first, followed by T3 and T1. The current vs.
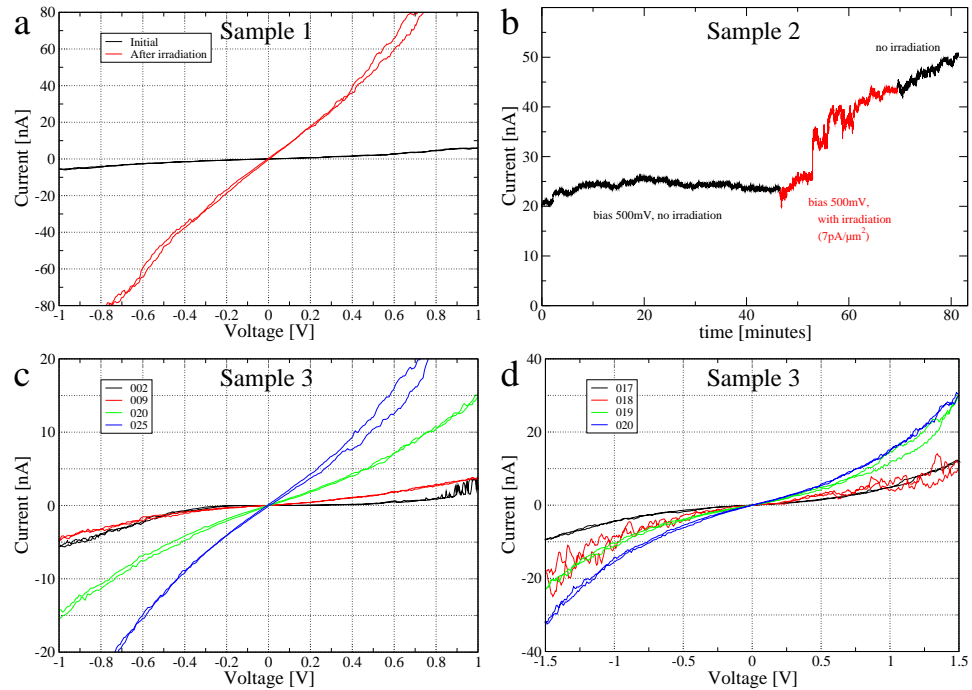
Figure 6.18: Increase in conductivity in samples 1-3 under electron irradiation. (a) shows a current-voltage plot from sample 1 before and after approximately 30 minutes of irradiation. The resistance decreases from $200M\Omega$ to $9.5M\Omega$. (b) shows the current through the nanotube in sample 2 at a fixed bias of 500mV. Irradiation is present during the red part of the curve. After the irradiation is stopped, the current keeps increasing for several more minutes. (c) shows a sequence of I-V curves from sample 3, showing the gradual increase in conductivity. The curves in (c) are taken without irradiation, but in-between several measurements are done with irradiation on the nanotube and the contact area. An example is given in (d): First, the black curve is obtained without irradiation. Next, the red curve is measured with an electron beam on nanotube and contacts. Strong fluctuations are present. The next measurement, the green curve, is again without irradiation. However, properties still vary during the green curve (up- and down-sweep is different), and only in the next sweep of the voltage a stable configuration (blue curve) is reached.
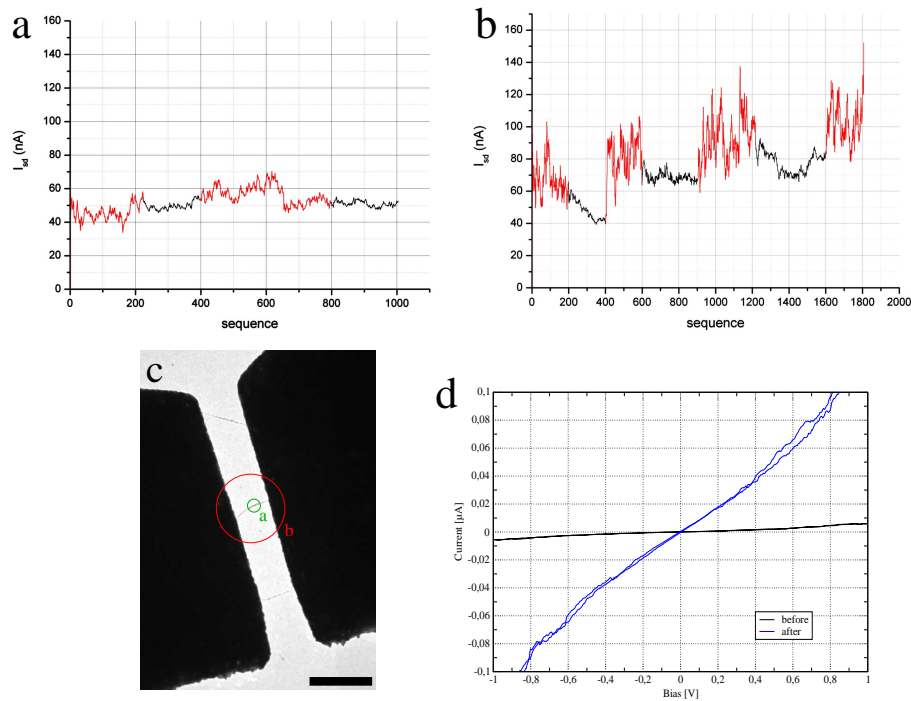
Figure 6.19: Current at a constant bias of 1V, with irradiation on only tube 2 (a), and tube 2 and its contact regions (b). Image (c) shows the irradiated regions during measurements (a) and (b). In (a) and (b) the beam was switched off in the black segments, and on during the red part of the curve. We find that the current strongly varies only if the contacts of tube 2 are irradiated (red sections in (b)). Small variations in the current are visible if a small spot illuminates only a section of the nanotube 2 without contacts (red sections in (a)). No change in the current was observed when irradiating the other tubes or their contacts (not shown). (d) shows the first and last current vs. voltage characteristic obtained from the sample. In between, significant electron irradiation (and electron beam induced carbon deposition) during various measurements have occurred. The resistance has decreased from 200MΩ to 10MΩ. Scale bar in (c) is 500nm.

voltage plot for the final measurement is shown in figure 6.20, together with images of the broken tubes. It seems that upon breakdown of T2 and T3, a catalytic reaction has occurred. Apparently, the catalyst particles attached to these tubes have consumed a significant part of the amorphous carbon and the nanotubes, producing a new hollow, tube-like structure with an inner diameter of approximately 10nm (Fig. 6.20b). Unfortunately, the reaction itself was too quick to be captured in the recorded images.

High-resolution images of a nanotube bundle after breakdown are shown in Fig. 6.20b. Clearly, the amorphous carbon on the nanotubes (deposited in the electron beam) has been rearranged into a more ordered, graphitic structure. This is evidence that the tube was heated significantly by the electric current. Before breakdown of the nanotubes, the carbon was annealed from an amorphous form to the graphitic structure. The tubes reached the highest temperature near the center, while the ends were presumably kept close to room temperature by the large metal contacts.

We summarize that one of the three tubes in this sample dominates its transport properties. Irradiation of the contacts induces strong variations in the contact resistance, while irradiation of just the tube has only a small effect. Joule heating by the current leads to high temperatures in the free-standing nanotube sections.

6.3.5.2   Sample 2

As in the previous sample, we measure the current at a fixed bias with and without electron irradiation. In contrast to sample 1, we do not observe fluctuations in the current as an effect of irradiation. This sample also shows an increase in conductivity during the course of the experiment (from 32MΩ to 2.9MΩ). Finally, we increase the bias until the nanotube fails. Sample 2 displayed several interesting effects during this process.

The first observation is related to the catalyst particles which are attached to the nanotube. As the current through the nanotube reaches 2μA, the nickel catalyst particles begin to migrate towards the contacts. Figure 6.21 shows the I-V plot and TEM images of the nanotube. Catalyst particles start to disappear at the center; the dark spots that disappear first are inside the large piece of debris near the center of the tube. We assume that the metal becomes mobile as it reaches a certain temperature. Thus, the hottest part of the tube would be near the center, while the ends are cooled by thermal contact with the sample structure.

At the left end, the metal appears to move from one nucleation site to the next, observed as consecutive catalyst particles growing and shrinking during the process. Disappearing metal is also seen at the right end, but the material here is not carried to subsequent particles closer to the contact. This indicates that the direction of the current dictates the way the material migrates along the tube. The catalyst moves against the direction of the electron flow.

After observing the catalyst migration, the measurement is stopped, and images of the nanotube are obtained at higher magnification. This is also shown in Figure
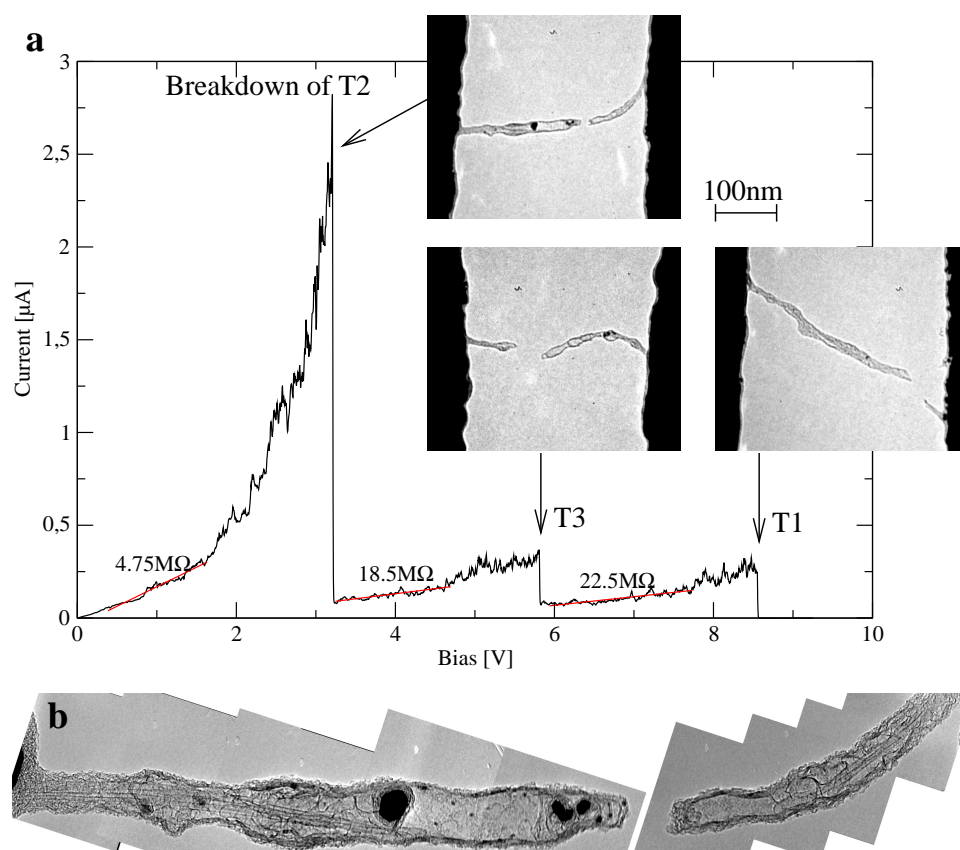
a

b

Figure 6.20: (a) Current-driven breakdown of the nanotubes in sample 1. In three fits to the graph (red lines) the differential resistance in the corresponding section is given. This shows that tube T2 has a significantly lower resistance than T1 and T3. Inset are images of each tube after breakdown. Upon breakdown T2 and T3 have partly turned into hollow structures with an internal diameter of roughly 10nm, probably through a reaction catalyzed by the leftover catalyst that was sticking to these tubes. (b) High resolution image of T2 after breakdown (scale bar 10nm).
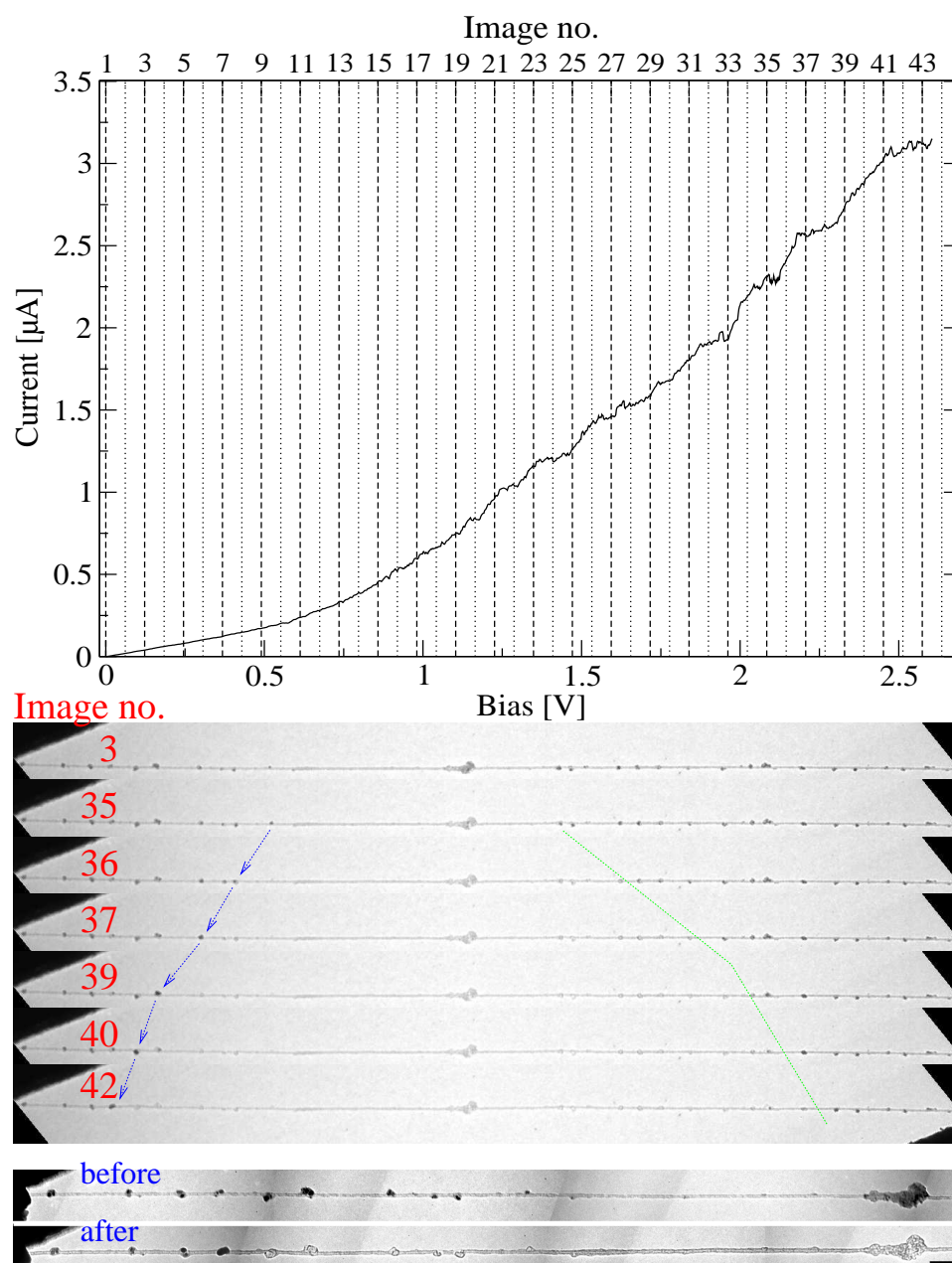
Figure 6.21: Migration of Ni catalyst at high current in the nanotube. The upper image shows the I-V plot with the positions where images were taken. Images with corresponding numbers are displayed below. At the left contact, we observe that catalyst material migrates towards the contact, with consecutive spots growing and shrinking during the process. At the right contact the catalyst also disappears, but no growing particles are observed. The two images at the bottom show the left end of the tube at higher magnification, before and after the migration of the catalyst. Empty carbon shells remain which have previously encapsulated the catalyst. The scale bar (valid for the two images at the bottom) is 100nm; for the other images the visible length of the tube is 4μm.

6.21. We find that the carbon shells around the catalyst particles are still present, but the metal is not.

Next, we continue to slowly increase the voltage up to 5V (starting again from 0). Much heat seems to be dissipated in the large piece of debris near the center of the nanotube. This is where the catalyst migration starts, this debris itself is mostly evaporated before failure of the nanotube, and it is the point where the tube finally breaks. However as we know from the diffraction analysis, on both sides there is an identical SWNT, so the tube should be continuous through this object. It is the mere presence of this debris that allows additional scattering.

In the leftover nanotube end from the first breakdown, we see that part of the amorphous carbon coating (deposited by the electron beam) was turned into more ordered graphitic layers on the nanotube (Fig. 6.23b). This is most likely an annealing effect at elevated temperatures, because it occurred only slightly away from the (cold) contact. Close to the breakdown point, the entire tube structure is rearranged (Fig. 6.23c): There is hardly any carbon left in an amorphous form, it has been fully converted into a layered structure.

After the second breakdown, the nanotube still bridges the gap with an undefined, thin carbon structure. Instead of breaking at a single point, the structure has completely rearranged along a significant part of its length. Again, no modification has occurred near the cold contact (the contact at that end where the tube was attached all the time, not where it re-attached after the first breakdown).

6.3.6 Switching effect

A peculiar effect is observed in the sample with the individual semiconducting (13,09) nanotube: The conductivity of the tube is reversibly switched by 2-3 orders of magnitude. We will denote this as "on" and "off" state of the nanotube.

The tube is switched to the "on" state by passing a high current ($\approx 1\mu$A) (Fig. 6.24a). Irradiation of the contacts switches the device back to the "off" state (Fig. 6.24b). As seen in Fig. 6.24b, the current at a fixed bias can drop by more than 3 orders of magnitude shortly after the irradiation is switched on, and remains low even after the beam is blanked. But passing a current of $\approx 1\mu$A brings the device back to the "on" state, and the whole process is repeated several times. Fig. 6.25 shows an I-V characteristic in the on- and off-states, at a different scale for comparison. Similar to the previously described devices, the conductivity in the "on" state increases during the course of the irradiation experiment.

6.3.7 Discussion

The in-situ experiments demonstrate the dominating effect of the contact resistances on the transport properties. A steady increase in conductivity is observed during irradiation of the contacts (together with a current trough the device), not during irradiation of only the free-standing nanotube section. However, it is not the deposited carbon alone which improves the contact; there must be further reorga-
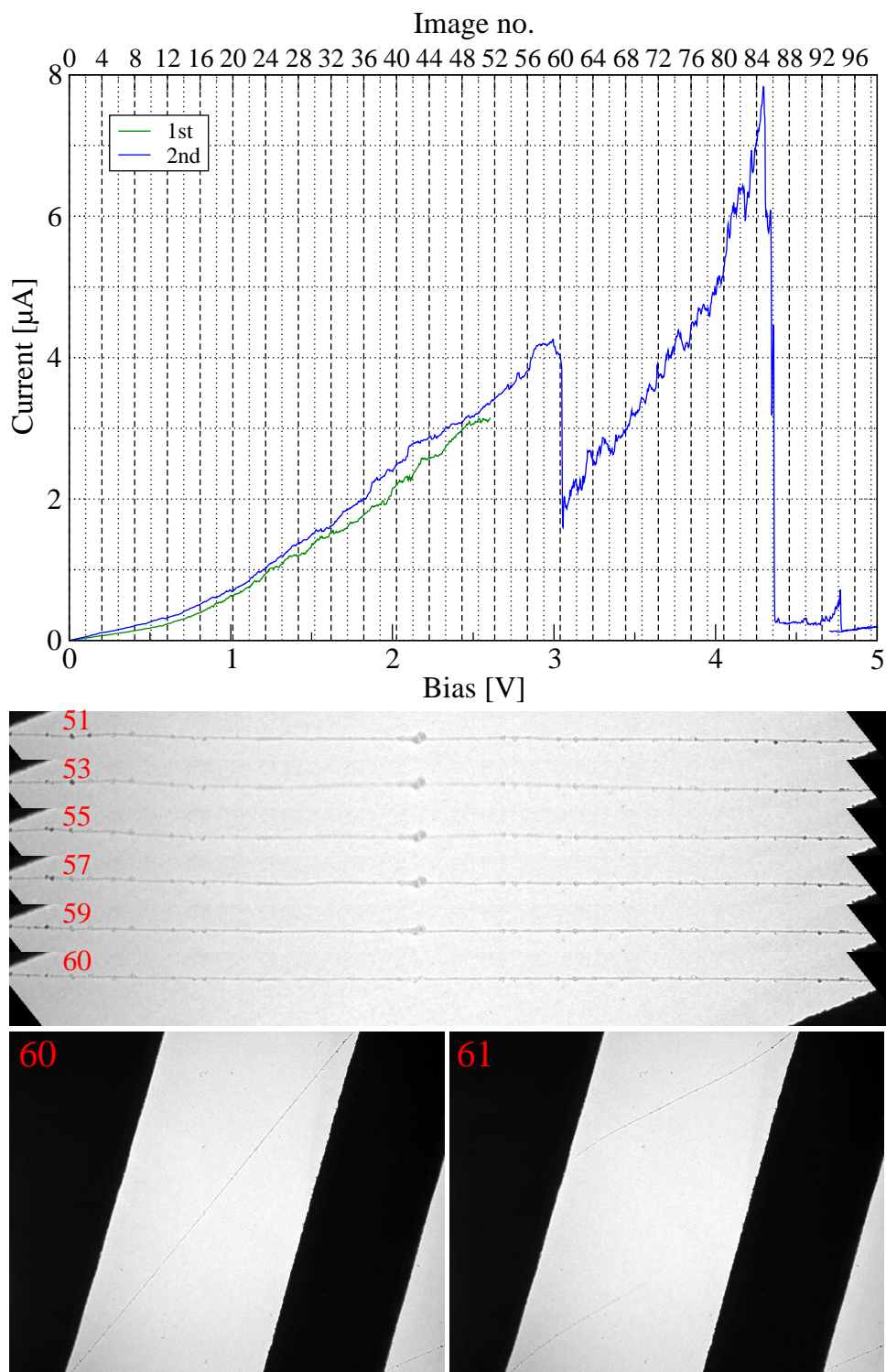
Figure 6.22: First breakdown of the nanotube. Between images 60 and 61 the nanotube breaks, but one of the open ends re-attaches to the other contact. The debris near the center of the nanotube evaporates just before breakdown.
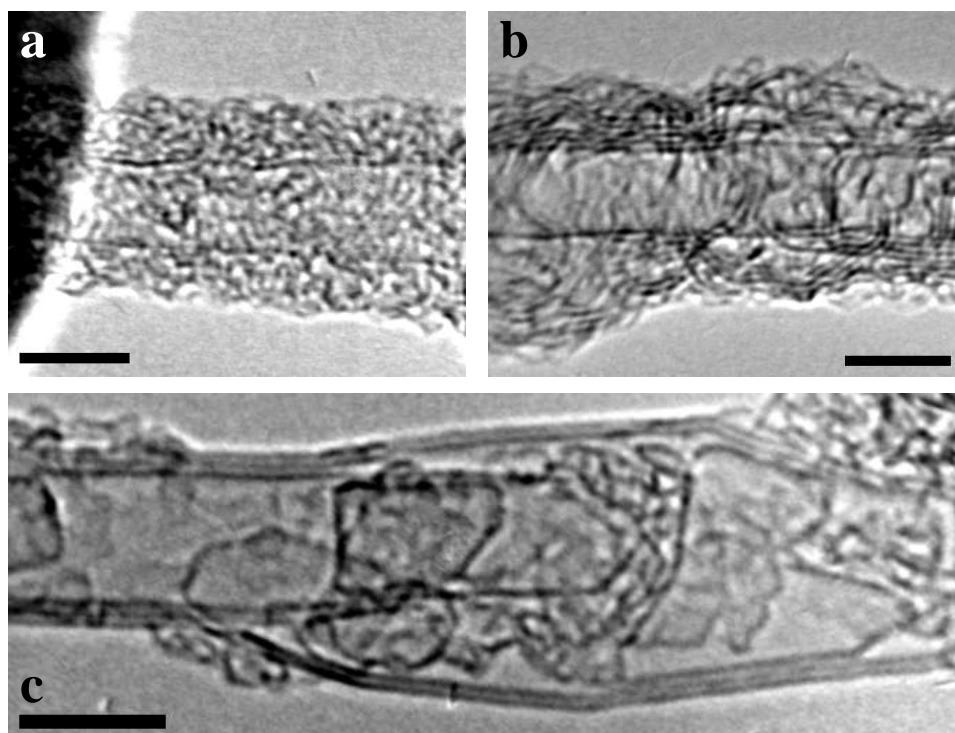
Figure 6.23: Modifications of the amorphous carbon on the current-heated nanotube. (a) At the cold contact, the amorphous carbon remains in its original conformation. (b) Away from the contact, the carbon was annealed into layered sheets around the central tube, reminiscent of multi-shell nanotubes. (c) Near the breakdown point, the entire carbon has rearranged into a layered but no longer perfectly tubular structure. All scale bars are 5nm.
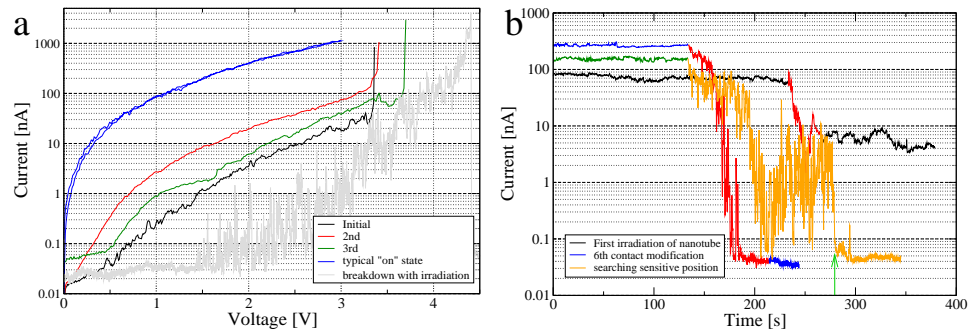
Figure 6.24: Current- and radiation induced contact modifications of the semiconducting (13,09) nanotube. We obtain a distinct "on" state after passing a current of $\approx 1\mu$A through the nanotube (a), and switch the device back to the "off" state after a short irradiation with electrons (b). In (a), the voltage is slowly increased until the current suddenly increases to more than 1μA, where the voltage is switched off (black, green and red curves). Afterwards, a high conductivity is found (blue curve). In (b), the current is measured at a fixed bias, and the irradiation is switched on during the red or orange parts of the curves. In this device, we observe a decrease in conductivity by up to 3 orders of magnitude as the irradiation is switched on. In the green/orange curve, a small beam (130nm diameter) is used to localize the sensitive point in the sample. At the point indicated by the green arrow, the irradiation is moved to underneath one of the contacts, where the device finally reaches its "off" state. The sample is reproducibly switched in this way between "on" and "off" 9 times. Finally, we increase the bias in presence of irradiation until the nanotube is destroyed. This is shown in the grey curve in (a). The breakdown observed by TEM exactly coincides with the drop in the current.
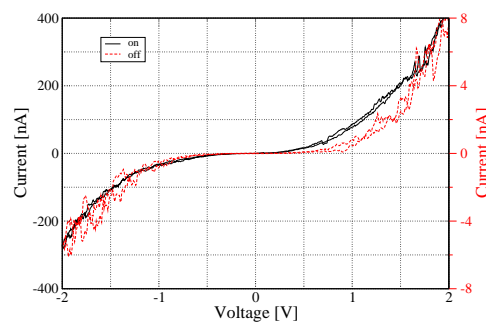

Figure 6.25: Current- vs. voltage characteristic of the (13,09) in the on-state (black) and off-state (red). Note the 50x different scale for both curves, while the shape of the curves is similar.

nizations of the deposited material by the electric current through the device. This is clearly shown by the continued change in resistance after the beam is switched off again (Fig. 6.18b+d).

In an ideal ballistic conductor, the entire energy would be dissipated in the contacts. The mean free path in carbon nanotubes, however, is clearly shorter than the length of our free-standing nanotubes. Therefore we observe the joule heating which turns the amorphous carbon on the nanotubes into ordered, layered structures (Fig. 6.23). If a similar amount of energy is dissipated at the nanotube-metal interface, it is reasonable to assume that well graphitized structures form at these interfaces as well. Unfortunately, the nanotube-metal interfaces can not be observed with our free-standing nanotube devices in the present geometry.

Large variations in the conductivity due to irradiation are observed in the semi-conducting nanotubes, and the bundle (Fig 6.19b) (a bundle will very likely contain also some semiconducting tubes). These variations are visible as noise (like in Fig. 6.19b) in the semiconducting devices, and in one device also as two stable config-urations (Figs. 6.24 and 6.25, Section 6.3.6). As illustrated in Fig. 6.14 there is a silicon dioxide layer remaining in the free-standing structure, which may easily be charged by the electron beam. A semiconducting nanotube would be sensi-tive to such charges, while metallic tubes are not influenced. Irradiation of silicon dioxide with high energy electrons creates positively charged defect sites, i.e., in total more electrons are released by the radiation than are captured from the beam [92]. A positive charge near a (p-doped) semiconducting nanotube would suppress conduction through the tube. This can explain the switching off of the device in Fig. 6.24b, while it is not clear why it switches back to the "on" state by passing a high current. In any case, the noise-like variations in the current during irradiation of semiconducting tubes can be explained by a variation of local charges close to the nanotubes. In agreement with this explanation, no noise-like variations in the current during irradiation were observed in the metallic nanotube.

There is significant joule heating by the current through the free-standing nanotube. One effect is the annealing of amorphous carbon (Fig. 6.23). Al-ready at lower temperatures, we observed the migration of catalyst particles (Fig. 6.21). Both observations clearly indicate a temperature profile where the nanotube reaches the highest temperatures near its center, while it is held at lower temper-atures at the ends by the metal contacts. We expect the nickel nanoparticles to become mobile at temperatures near its melting point, which is 1455°C. No modi-fications of the nanotube were observed up to this point. This shows that the free-standing SWNT, in the high vacuum environment of the microscope, can withstand very high temperatures. More important, these temperatures were not applied from outside, but induced by joule heating from a current through the tube. The tube is heated homogeneously, not just at individual defects.

This single-tube nanoscopic hot filament would most likely emit black-body radiation in the visible and infrared range, as well as thermally excited electrons, from a very small (line-shaped) region. Further, it could provide a means to heat an object, which is suspended (like the catalyst nanoparticles) on the free-standing

carbon nanotube.

6.4 Conclusions

We have carried out transport measurements on carbon nanotubes which were precisely characterized by high-resolution TEM imaging and/or electron diffraction. The results confirm the previously established dependence of the metallic or semiconducting behaviour on the nanotube indices. These are the first direct measurements of the SWNT structure in combination with its electronic transport properties. Additionally, our approach allows measurements in a transistor configuration, which provides significantly more information than only the current-voltage characteristics. Temperature dependent measurements allow us to determine the activation energy for transport along the nanotube. For the semiconducting tube, the barrier is attributed to a Schottky interface at the contacts, and it appears to be well described by the conventional models for a Schottky interface.

The combined study of transport and high-resolution imaging of endohedral metallofullerene peapods so far did not find a significant difference in the transport properties of filled and empty nanotubes. However, we did observe a behaviour that was previously attributed to filled nanotubes also in definitely empty ones. Additional experiments are required to definitely establish the effect of fullerene doping on the electronic properties, especially measurements on individual and completely filled tubes.

The in-situ transport measurements showed that the contact resistances have a large contribution to the transport properties of carbon nanotubes. Irradiation of the contacts causes large variations in the conductivity, while irradiation of only the free-standing tube section does not. Additionally we investigate the breakdown of the nanotube caused by passing a high current. The nanotube is heated by the current to high temperatures, sufficient to melt the nickel catalyst or even reorganize the amorphous carbon into a more ordered structure.

Chapter 7

Nanoelectromechanical devices

Due to their outstanding mechanical and electronic properties, carbon nanotubes are considered as potential building blocks for a wide range of future nanoscale devices. The miniaturization of electronic devices in the past decades has had an enormous impact. But the scaling down of silicon-based electronic systems has reached a level where it will be difficult for emerging technologies to compete. The miniaturization of mechanical systems, on the other hand, is not easily achieved by scaling down micro-electromechanical systems (MEMS), and is limited by the strength and flexibility of the material. Here, the combination of a high strength, flexibility, and thermal and electrical conductivity of carbon nanotubes, still offers plenty of room for miniaturization. We demonstrate that true nano-electromechanical systems (NEMS) can be built based on carbon nanotubes.

7.1   MWNT based devices

Due to their (compared to SWNTs) easier handling and higher rigidity and stability, various MWNT based NEMS have been shown by several groups. In the most spectacular of these devices, the multi-walled nanotube serves as torsional spring for small angular deformations [93] and torsional oscillations [94], or as bearing for continuous rotational operation [95, 96]. Basically, a bearing is formed where some of the shells rotate around or inside the remaining shells. Further investigations dealt with the telescopic extension of MWNT shells [97], and observations of bending and resonant vibrations [98, 99].

We show devices, prepared by electron beam lithography and an etching process, where MWNTs are attached on one side and bent by an electric field towards another lithographically defined contact. These experiments are carried out inside the Zeiss 912Ω transmission electron microscope, equipped with a special sample holder that allows electric connections to the sample from the outside simultaneously with the TEM investigation. In the more advanced devices, metal structures are attached to the open end of the MWNT, actuated also by an external field.
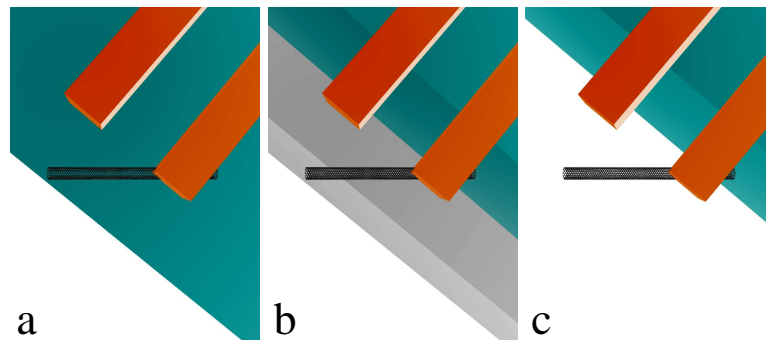
Figure 7.1: Principle of the device preparation: (a) The desired structure is prepared on top of the carbon nanotubes, close to a cleaved edge of the substrate, using electron beam lithography and a marker system. The etching process undercuts the structure from the side, removing the shaded volume in (b). This results in the structure reaching out across the side edge of the substrate (c). The free-standing part is now free to move, and accessible by TEM.

7.1.1   Sample preparation

For building the devices shown in this subsection, multi-walled carbon nanotubes (MWNTs) are dispersed on a GaAs substrate with a lithographically prepared marker system. Individual tubes are located with respect to the marker system using an atomic force microscope (AFM). The desired metal structure is built on top of the nanotubes by electron beam lithography. An etching process is used to remove a part of the substrate in such a way that the structure is free-standing and accessible with a transmission electron microscope (TEM). The principle of this process is shown in Figure 7.1. The substrate is coated with a resist as a protection layer, and is cleaved so that the structure is near the cleaved edge. In the following etching step the structure is undercut (due to the resist) only from the side. The etching process, in a mixture of citric acid and hydrogen peroxide, is monitored with an optical microscope and stopped when a sufficient part of the structure is reaching out across the side edge of the substrate. The resist is then dissolved in methylpyrrolidon and acetone. A critical point drying step afterwards is important since any surface tension would destroy the delicate structures.

This process is conceptually similar to the silicon-based devices shown before, except that we use different etchants for the GaAs substrate, and a resist layer (instead of silicon oxide) as mask on the top of the substrate.

7.1.2   In-situ experiments

In the devices shown in figures 7.2 and 7.3, one end of the nanotube is attached to a metal block, and the open end is electrostatically attracted by a second nearby metal contact. The tubes are bending towards the second contact, with the tube

bending into a smooth curve (as opposed to a sharp kink). In the second device, a small piece of metal was placed onto the tube, moving along with the tube and even twisting it at higher voltages. In this device, it is clearly not only the tube end which is pulled towards the second contact, but also the metal block on the tube.

7.1.3 Discussion

Although the nanotubes undergo a large deformation, they stay within the elastic regime and move back to the initial position as soon as the voltage is switched off. A wear or fatigue is neither observed nor expected for these deformations. Carbon nanotubes exhibit a combination of high strength and large elastic range not found in other materials. Individual tubes have a Young's modulus Y=1TPa and are stable at strains of more than 7%. The values for silicon are Y=0.13TPa and a maximum strain of less than 3%. What is more important is that fabricating a cantilever beam of a size and aspect ratio similar to the carbon nanotube is not possible with current lithographic technologies. However, only a sufficiently thin flexible rod can be bent into a small radius of curvature: The minimum radius of curvature r_{min} for a cantilever beam of a width d and material limited maximum strain s_{max} is given by $r_{min} = d/2s_{max}$ (at this curvature the outermost layer would experience the maximum strain). This means that a multi-walled carbon nanotube with a typical diameter of 15nm could be bent into loop with a radius of 110nm. A single-crystal silicon cantilever beam with a width of 200nm, on the other hand, would ideally break if bent into a circle with a radius of less than 3.3μm; and in reality already at much lower strain since defects play an important role in brittle materials. The nanotube shown in Fig. 7.2, for comparison, shows a bending radius of 1μm at the point of highest curvature. These devices clearly demonstrate the high potential for carbon nanotubes as motion-enabling elements in nanoscale electromechanical systems, and they may replace the silicon-based cantilever beams used in today's microelectromechanical systems.

7.2 SWNT based NEMS

Nanoelectromechanical systems based on single-walled carbon nanotubes are much less frequently found in literature. For example, there exists no previous work where objects were suspended on a SWNT and actuated in any way. There are a variety of ways to fabricate suspended nanotubes, clamped at two ends with a free-standing section. Guitar-string like oscillations have been excited and detected in suspended single-walled carbon nanotubes [100]. A key aspect in [100] is the detection of a mechanical deformation by the nanotube itself, i.e. from changes in the electronic structure caused by the deformation. Several publications deal with the investigation and manipulation of free-standing SWNTs, e.g. by AFM [101] or irradiation [102, 103]. However, they can not be considered to be a nanoelec-
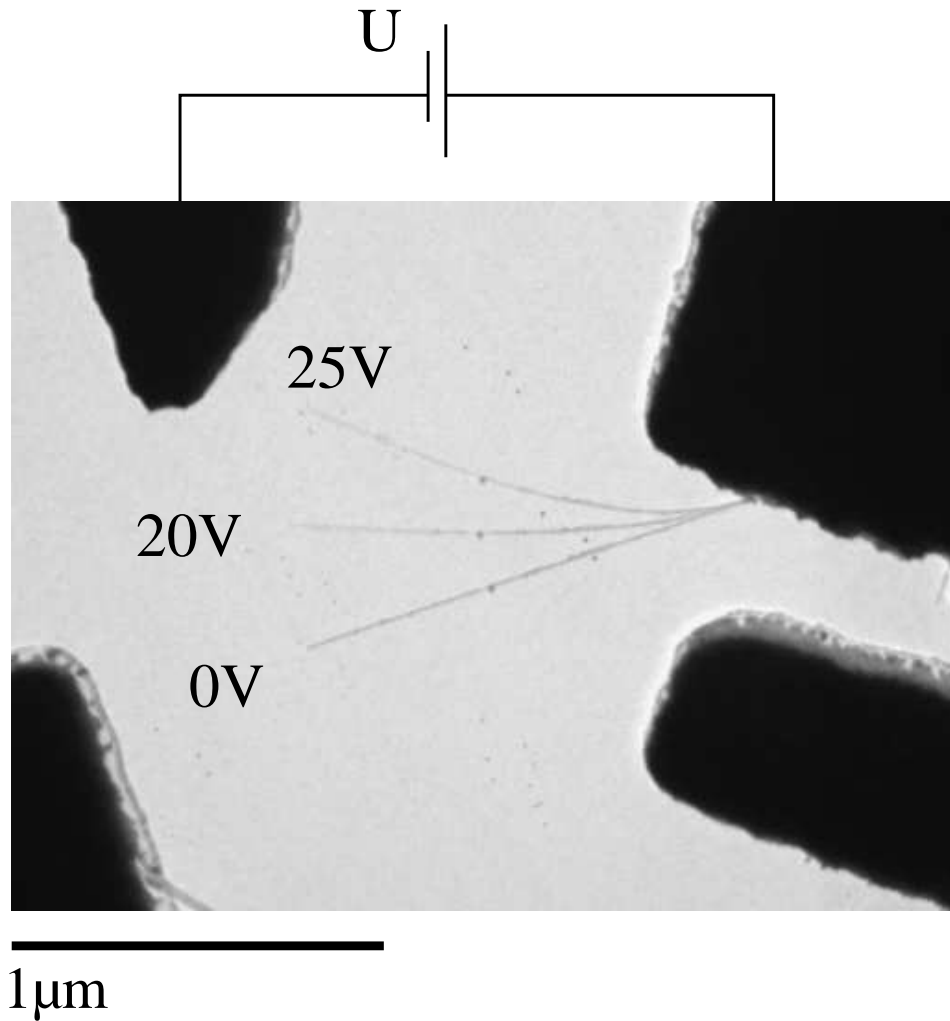
Figure 7.2: A multi-walled carbon nanotube (MWNT) attached at one end to the first electrode. As the tube is charged with respect to the second electrode, it bends towards it due to electrostatic attraction. The deformation is reversible, showing that it is within the elastic regime. No sign of wear or fatigue is observed after multiple deformations.
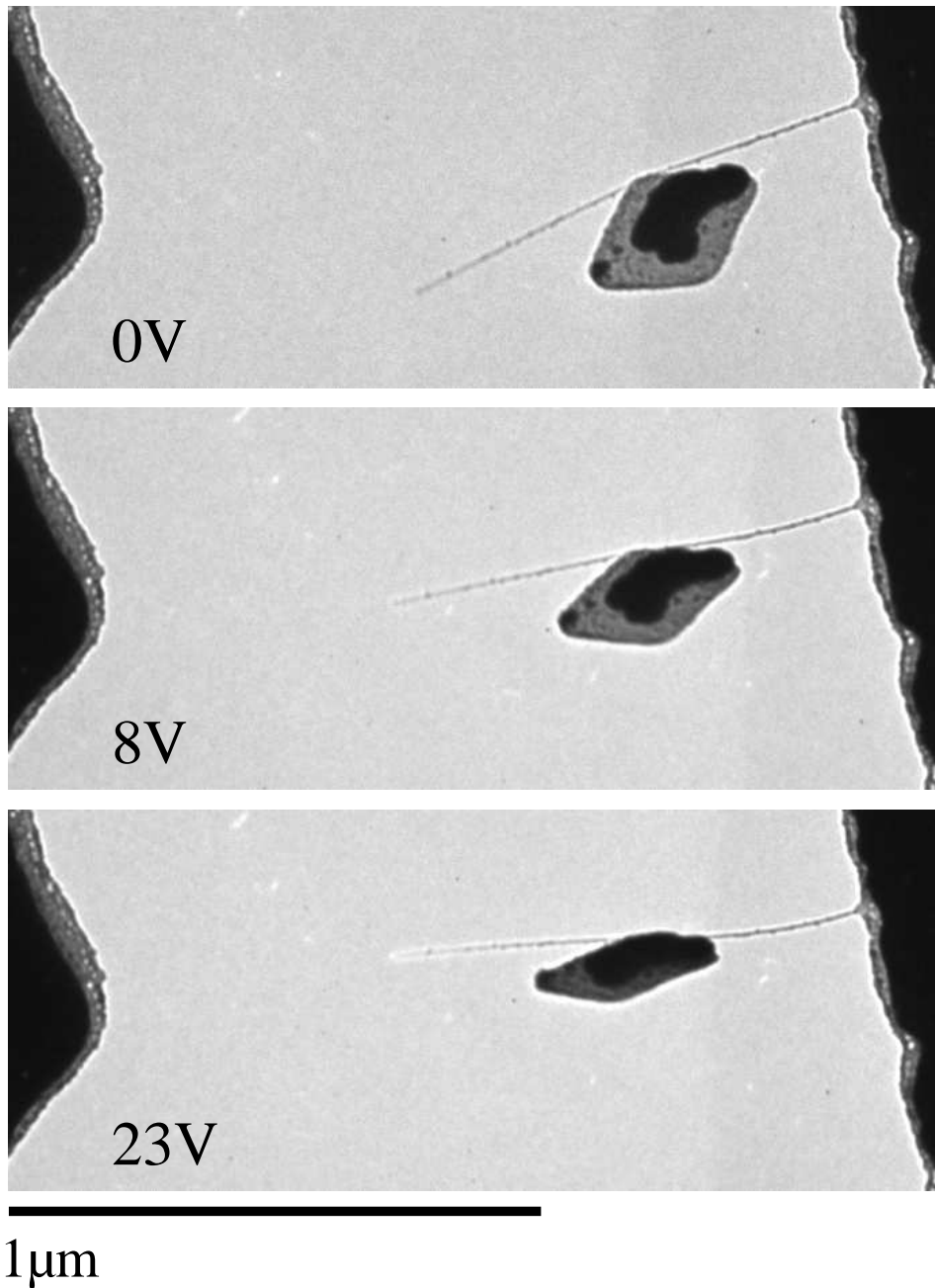
Figure 7.3: Another device, with a metal platelet attached to the nanotube. It moves along with the bending nanotube (0-8V), and twists out of the plane at higher voltage (up to 23V).
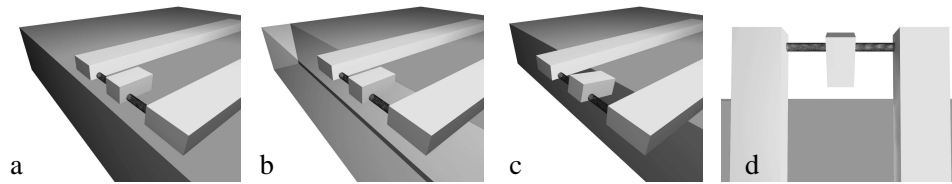
Figure 7.4: Principle of sample preparation: The structure is prepared on top of the nanotubes by electron beam lithography close to a cleaved edge of a substrate (a). An etching process removes part of the substrate (b). The part of the structure reaching out across the side edge is now free to move (c). Viewed from top (d), it is accessible by the transmission electron microscope.

tromechanical system, since the mechanical movement of the tube is caused by the (much larger) external tools like the AFM.

We achieved to prepare lithographically defined objects attached on individual single-walled carbon nanotubes that can be actuated by a local electric field. The cross-section of a SWNT is more than two orders of magnitude smaller than that of a MWNT. In these devices, large deformations are possible within the elastic regime. The moving part returns to its initial position even after being turned by 180°. Our way of preparation allows a characterization by TEM, which due to its high resolution is crucial for optimizing nanoelectromechanical systems of this size. And the ultra-low torsional spring constant provided by the SWNT allows for an easily detected deflection of the pendulum from excitations as small as those from the thermal energy.

7.2.1 Sample preparation

The sample preparation again consists of a lithographically defined structure that is made free-standing in an etching process. The structure is designed so that free-standing objects are obtained, attached only by the nanotubes.

The devices were prepared either from laser-grown nanotubes on gallium arsenide substrates, or from CVD-grown nanotubes on a Silicon substrate with a 200nm oxide. The tubes are located with respect to a marker structure by atomic force microscopy (AFM). The device structure, consisting of 100nm Au with a 3nm Cr adhesion layer, is prepared by electron beam lithography. The substrate is cleaved so that the structure is close (few μm) to a cleaved edge as illustrated in Fig. 7.4. The GaAs substrates undergo the same etching process described before. The Si substrates are etched first in 15% tetramethylammoniumhydroxide (TMAH) solution for several hours, and then in buffered HF for 2 minutes to remove the oxide layer, followed by critical point drying. The KOH process is not suitable for these delicate devices: The large amount of bubbles generated at the Si surfaces creates too much mechanical stress.

7.2.2 Suspended objects

Objects suspended on several SWNTs can be prepared by creating separated metal objects in the free-standing grid structure. Figure 7.5 shows several examples. These are precursors of the nanoelectromechanical devices built on single nanotubes which are shown in the next subsections.

7.2.3 Torsional pendulum built on SWNT bundles

Objects suspended on one tube or bundle exhibit rotational freedom. The tube serves as torsional spring, and allows large elastic deformations. These devices are torsional pendulums built on a few nanotube molecules, or ultimately a single molecule.

If the nanotubes are absorbed on the substrate from a suspension, bundles frequently occur. Often it can not be decided from the AFM image whether a nanotube is individual or a small bundle. Consequently, some of the nanoelectromechanical devices were built on small bundles of SWNTs. Figure 7.6a shows AFM images of a marker system with nanotubes and the structure to be prepared by electron beam lithography. After lithography, the sample is cleaved and etched, and the free-standing structure in Figure 7.6b is obtained.

This example also demonstrates how well controlled a free-standing structure can be "designed" by electron beam lithography. The only thing that can not be controlled is the location of the nanotubes, so the structure has to be built around those tubes which happen to be in a useful configuration. Zooming in to the suspended objects, we find that some of them are not free to rotate due to tubes that were overseen by the AFM (inset in Fig. 7.6b). This is a problem if the AFM images are not taken at a sufficient resolution, which was of course solved in the following devices. Figure 7.7 shows a metal block suspended on a bundle of SWNTs.

By applying a potential between the support of the pendulum and a nearby electrode (Fig. 7.7a), the pendulum can be turned by up to $180°$. Figure 7.7b-i shows a series of TEM images obtained with an increasing potential.

7.2.4 The single molecule torsional pendulum

The devices presented in Fig. 7.8 and 7.9 consist of a metal block suspended on an *individual* single-walled nanotube. The key motion-enabling element here is a single molecule. Yet, the suspended object is large enough to be visible in an optical microscope. A pendulum on a 1.5nm diameter SWNT is supported by a total of only 40 C-C bonds (20 on each side), close to the limit (support by a single bond) that could be conceived for a mechanically attached object.

In the TEM, the pendulum shown in Fig. 7.8 is already turned by approximately $70°$ by electrostatic charging from the electron beam. Note that this effect would not affect the device in possible applications outside an electron microscope. The charging is attributed to high resistance contacts to the nanotube. It is not present in the device shown in Fig. 7.9, which can be actuated by an external field
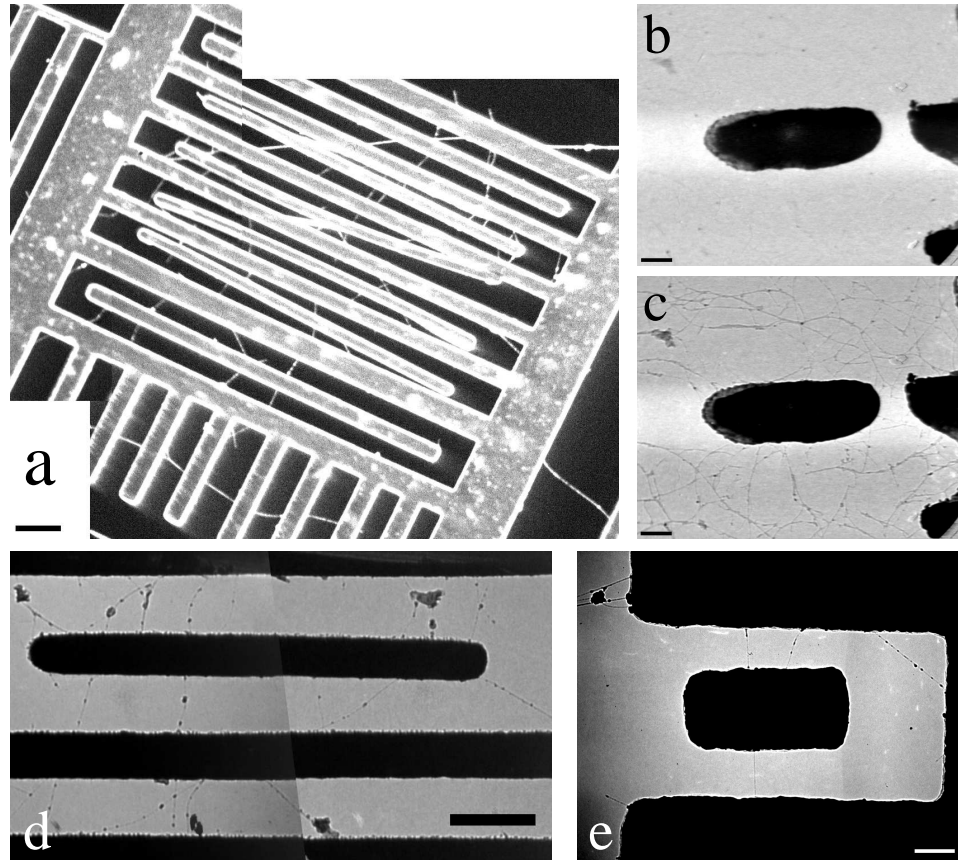
Figure 7.5: Lithographically defined metal objects suspended on a few single-walled carbon nanotubes. (a+d) Long metal bars suspended on few individual SWNTs. (b+c) Metal block suspended in a dense nanotube network at zero defocus (b) (nanotubes not visible) and at a large underfocus (c). (e) Metal block held by only three individual SWNTs. (a) is a dark-field TEM image, (b-e) are bright-field TEM images. All metal structures have a thickness of 100-120nm. Scale bars: 1μm (a), 200nm (b,c,e), 500nm (d).
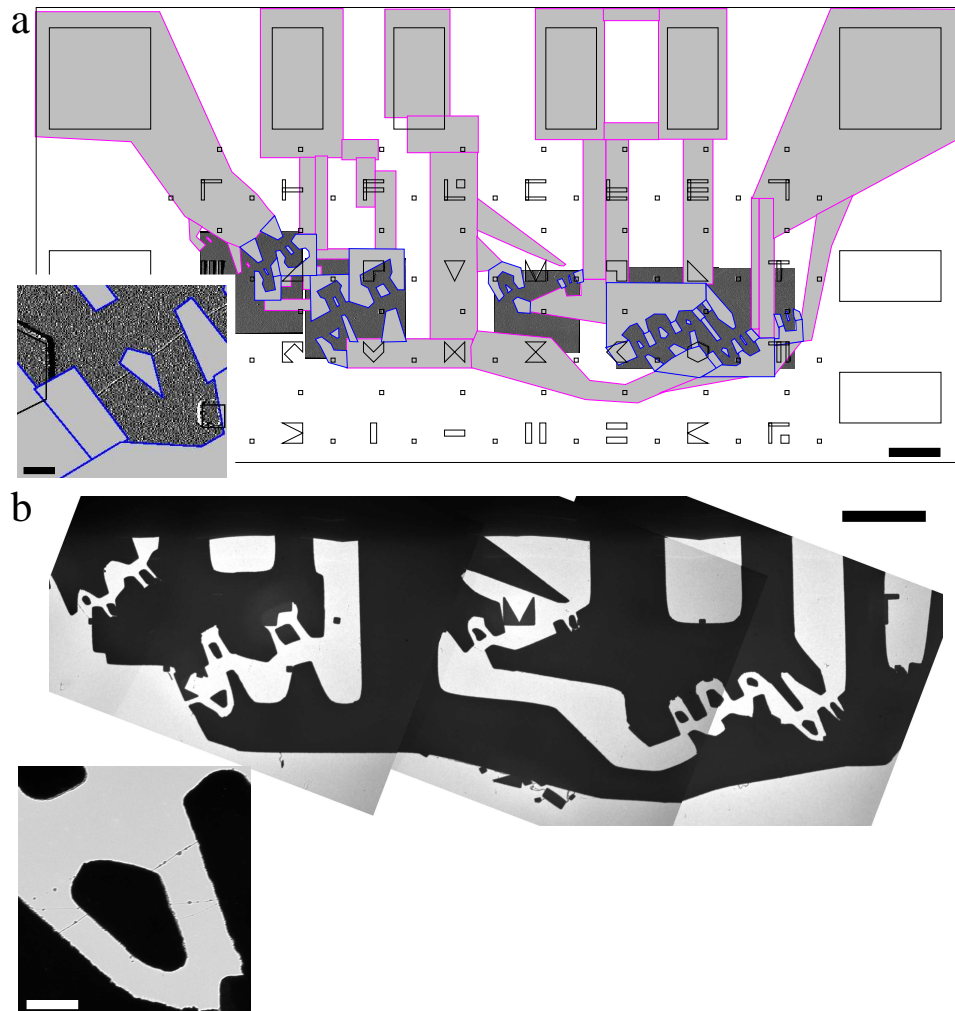
Figure 7.6: (a) Sample design: AFM images are located with respect to the marker system, and the structure is designed according to the location of the nanotubes. Inset in (a) shows a magnified view on a metal block to be placed on a small nanotube bundle. (b) shows the same structure after lithography and etching (low-magnification TEM images). Several objects suspended on a few nanotubes are visible. The nanotubes are not visible at this magnification. The inset in (b) shows the device from the inset in (a). It contains additional tubes (not detected by AFM) which block the torsional motion. Scale bars are 5μm in (a) and (b), and 500nm for the insets.
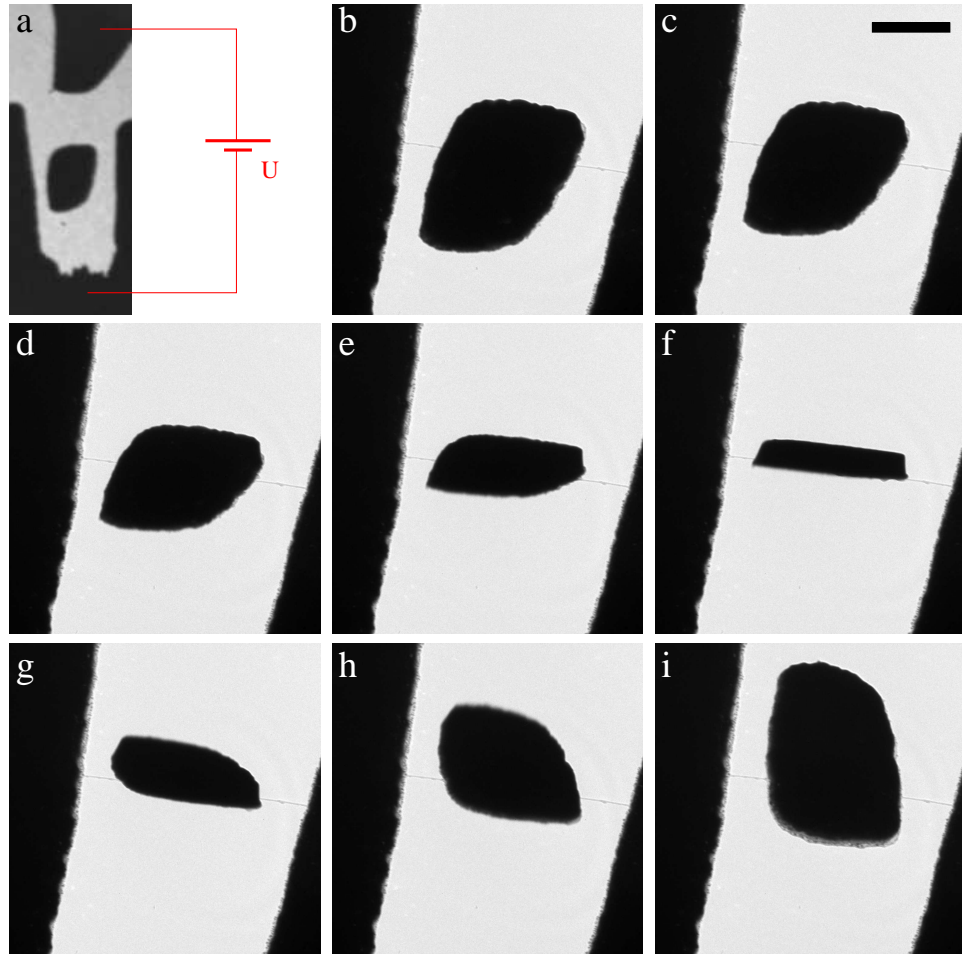
Figure 7.7: A metal block suspended on a small bundle of SWNTs. (a) shows the configuration of the pendulum with its support and the second electrode. As the potential is increased, the metal block is turned by up to 180° (b-i). Scale bar is 500nm.
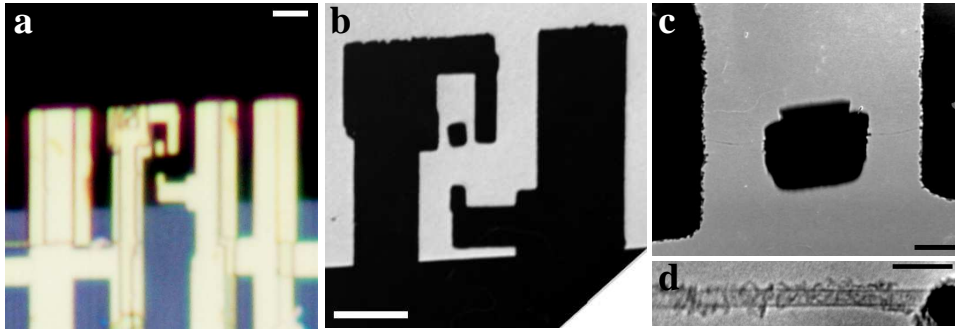
Figure 7.8: A metal block suspended on one individual single-walled carbon nanotube. The metal block is visible in an optical microscope (a). In the transmission electron microscope , the suspended part rotates by up to approximately 70 degrees due to charging by the electron beam with increasing magnification (b+c). The high-resolution TEM image (d), taken at the right end of the tube, shows that this device is indeed built on one single molecule. Most of the amorphous carbon visible in (d) was deposited during the TEM analysis. Scale bars are 2μm (a+b), 200nm (c) and 5nm (d)

between the support of the pendulum and a nearby electrode. The pendulum turns back to the initial position immediately as the potential is switched off, even though it was turned by approximately $150°$.

7.2.5 Device geometry and classical mechanics

The geometry of the rotor and nanotube is illustrated in Fig. 7.10. We consider it as a cuboid with a mass density ρ and dimensions x, y, $z_1 + z_2$. It is suspended on a nanotube with diameter d and length l (lengths l_1 and l_2 on the two sides, for a pendulum not centered on the tube). The mass of the nanotube is neglected. The total mass is:

$$m = \rho xy(z_1 + z_2) \tag{7.1}$$

The moment of inertia J is calculated as

$$J = \int dV \cdot r^2 \rho(r) \tag{7.2}$$

where r is the distance of the volume element dV from the nanotube axis.
For a thin rotor $y \ll z_{1,2}$ we approximate this as

$$J = xy\rho \int_{-z_1}^{z_2} dz \cdot z^2 = \frac{xy\rho}{3}(z_1^3 + z_2^3) \tag{7.3}$$

The shear modulus M of the curved graphene sheet in a nanotube is calculated in [104] and is close to the value for the planar graphene sheet. The inter-tube distance of a multi-walled nanotube is taken as wall thickness of a hollow cylinder
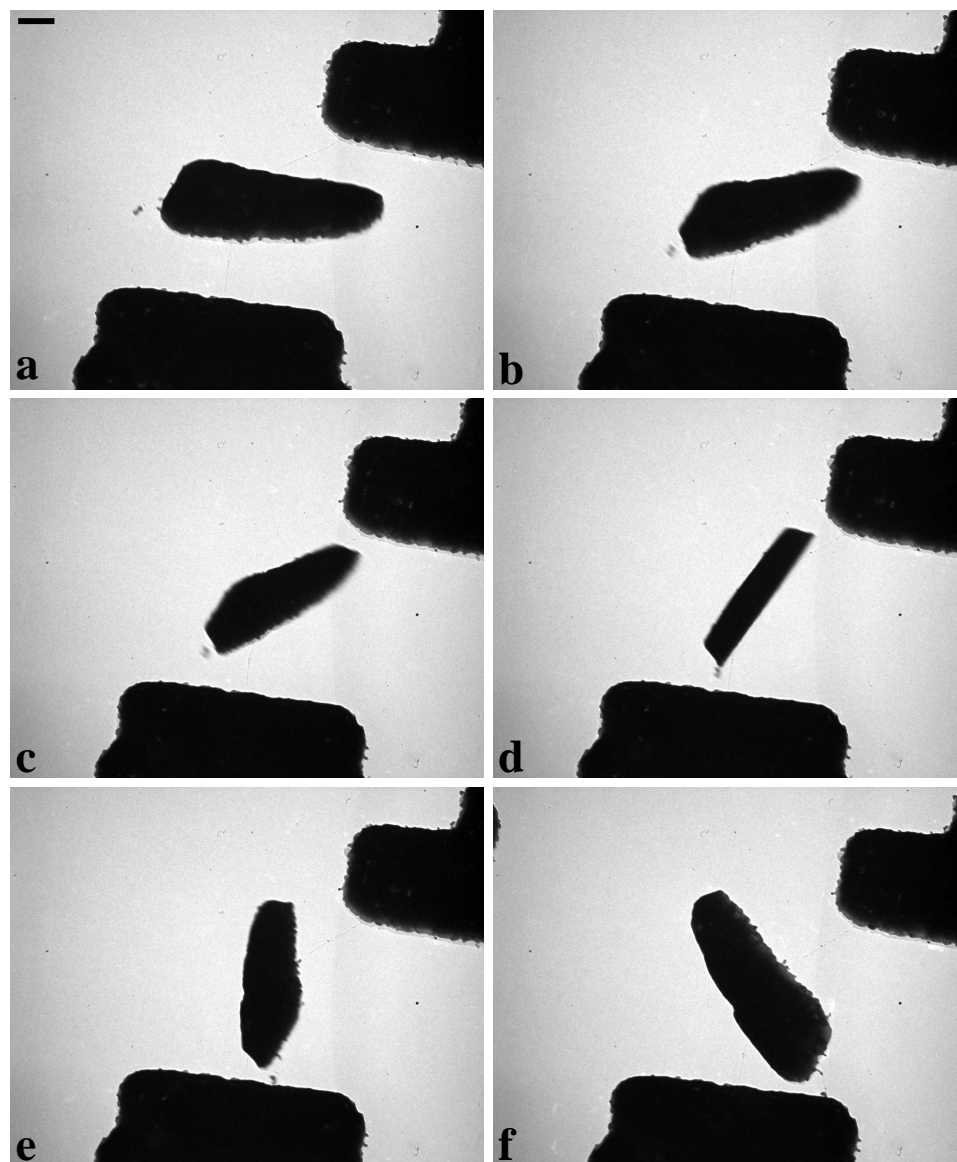
Figure 7.9: A torsional pendulum built on a single-walled carbon nanotube. Images a-f are obtained at a potential of 0V, 5V, 6V, 7.4V, 9.7V, and 22V between the support and the second electrode (visible in the upper left corner of image f). The sample is tilted by 30° for a slightly side-on view on the device. Scale bar is 100nm.
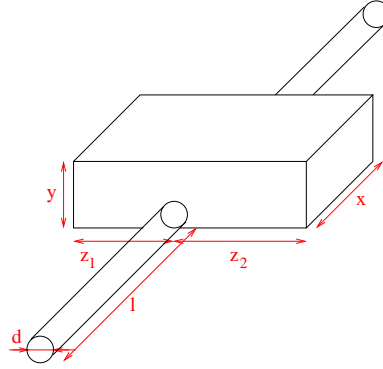
Figure 7.10: Device geometry.

both in [104] and in the following calculations: We use a shear modulus $M = 0.46$TPa and a wall thickness of $w = 3.4$Å.

Twisting a hollow cylinder (one nanotube on each side) of length l_n, diameter d and wall thickness $w \ll d$ by an angle α requires a torque T of

$$T = \frac{M\pi d^3 w \alpha}{4l_n} = C_n \alpha \tag{7.4}$$

where we define

$$C_n = \frac{M\pi d^3 w}{4l_n} \tag{7.5}$$

as the torsional spring constant. The index $n = 1, 2$ describes the two nanotube sections on each side of the pendulum, with a length l_1 and l_2. The total torsional spring constant is

$$C = C_1 + C_2 \tag{7.6}$$

The differential equation for a torsional oscillation

$$J\frac{d^2}{dt^2}\alpha + C\alpha = 0 \tag{7.7}$$

leads to solutions of the form

$$\alpha(t) = a\sin(\omega t) + b\cos(\omega t) \tag{7.8}$$

with the arbitrary constants a and b and the resonant frequency:

$$\omega = \sqrt{\frac{C}{J}} \tag{7.9}$$

For example, for the rotor in Fig. 7.8 we use the values d=2.4nm, x=500nm, y=110nm, z_1=250nm, z_2=600nm, l=300nm, and $\rho = 19.3 \cdot 10^3$kg/m^3 (density of gold). This gives a mass of $m = 9 \cdot 10^{-16}$kg, and a moment of inertia of

$J = 8 \cdot 10^{-29} \text{kgm}^2$. The torsion spring constant is $C \approx 1 \cdot 10^{-17} Nm$. With these values we arrive at a resonance frequency of $f = \frac{\omega}{2\pi} \approx 60\text{kHz}$ for the torsional mode of oscillation.

7.2.6 Quantum mechanical considerations

For the torsional harmonic oscillator the Schrödinger equation is

$$-\frac{\hbar^2}{2J}\frac{\delta^2}{\delta\alpha^2}\Psi(\alpha) + U(\alpha)\Psi(\alpha) = E\Psi(\alpha) \tag{7.10}$$

with the harmonic potential

$$U(\alpha) = \frac{1}{2}C\alpha^2 \tag{7.11}$$

and C and J as defined previously. By substituting $\omega = \sqrt{\frac{C}{J}}$ (as before) and

$$\alpha_0 = \sqrt{\frac{\hbar}{\omega J}} \tag{7.12}$$

the solutions (in analogy to the linear harmonic oscillator) are

$$\Psi_n = \left(2^n n! \sqrt{\pi}\alpha_0\right)^{-\frac{1}{2}} \exp\left\{-\frac{1}{2}\left(\frac{\alpha}{\alpha_0}\right)^2\right\} H_n\left(\frac{\alpha}{\alpha_0}\right) \tag{7.13}$$

with the hermite polynomials

$$H_n(x) = (-1)^n e^{x^2} \frac{d^n}{dx^n} e^{-x^2}. \tag{7.14}$$

The energy eigenvalues are:

$$E_n = (n + \frac{1}{2})\hbar\omega \tag{7.15}$$

The mean value of the angular displacement is obviously $< \alpha >= 0$. More interesting is the mean square value of the angular displacement,

$$< \alpha^2 >= \frac{\hbar}{\sqrt{C \cdot J}}(n + \frac{1}{2}) \tag{7.16}$$

With this expression we can calculate the root mean square (rms) value of the angular displacement $\Delta\alpha$ as

$$\Delta\alpha = \sqrt{< \alpha^2 >} = \sqrt{\frac{\hbar}{\sqrt{C \cdot J}}(n + \frac{1}{2})} \tag{7.17}$$

which defines for $n = 0$ the quantum limited position uncertainty.

For investigating quantum effects in macroscopic mechanical devices, a device with a large zero-point motion would be useful. The above equation shows that

for a large zero-point oscillation, it is not only important to have a small moving object (leading to a small mass and moment of inertia J), but also a weak coupling (here given by the spring constant C). Attaching a moving part with an individual single-walled carbon nanotube is presumably one of the weakest couplings (lowest spring constant) that can be realized.

For a typical device, the zero-point motion would have a width $\Delta\alpha_{max} = 4 \cdot 10^{-6}$, or approximately $2 \cdot 10^{-4}$ degrees. This corresponds to a position uncertainty of $2 \cdot 10^{-12}m$ at the edge of the pendulum, two orders of magnitude more than in silicon based nanoelectromechanical devices [105].

7.2.7 Thermally excited oscillations

Although we have not directly excited the torsional oscillation mode using e.g. an AC electric field, we can observe the thermally induced vibrations at room temperature and compare it to the amplitudes predicted for the device geometry. For $kT \gg E_0$ the thermal occupation number is:

$$n_{th} = \frac{1}{\exp(\frac{\hbar\omega}{k_B T}) - 1} \approx k_B T / \hbar\omega \qquad (7.18)$$

The corresponding rms value of the angular displacement, obtained by substituting (7.18) into (7.17) with $n \gg 1$, is:

$$\Delta\alpha = \sqrt{\frac{k_B T}{C}} \qquad (7.19)$$

This is also the classical amplitude for a harmonic torsional oscillation with an energy $k_B T$.

From the observations we will obtain the peak-to-peak amplitude of the oscillation α_{pp}. For a sinusoidal oscillation it is related to the rms value as

$$\alpha_{pp} = 2\sqrt{2}\Delta\alpha = 2\sqrt{\frac{2kT}{C}}. \qquad (7.20)$$

Now, before comparing observed with predicted oscillations, I will present further devices built on single-walled carbon nanotubes.

7.2.8 The single molecule torsional pendulum: more examples

Nanoelectromechanical devices based on individual single-walled carbon nanotubes and small nanotube bundles have been successfully prepared with very different geometries and sizes. The nanotube diameter in devices built on individual nanotubes ranges from 1 to 2.4 nm. On individual nanotubes, objects as heavy as $\approx 10^{-15}$kg have been suspended. On the other end of the scale, a low-mass pendulum consisting of a 5nm Cr layer was built on an individual SWNT (Fig. 7.11a+b), and for comparison on a MWNT (Fig. 7.11c+d). In the nominally 5nm thick Cr
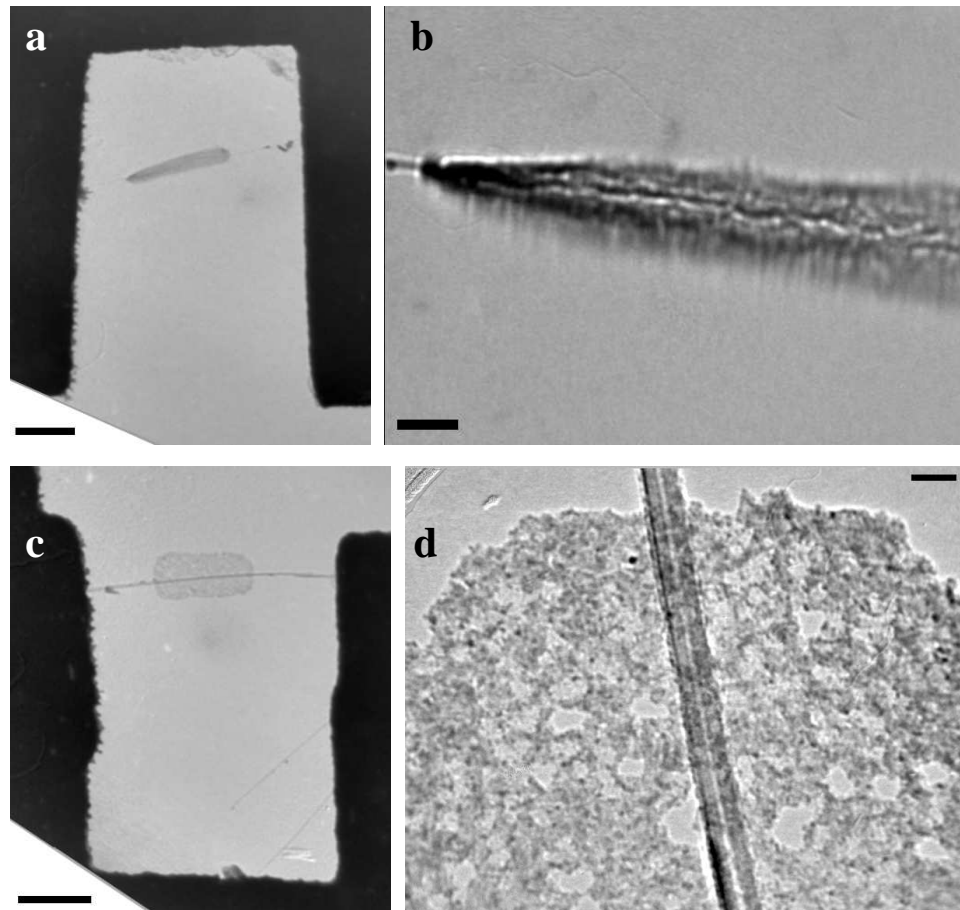
Figure 7.11: A pendulum built from an only 5nm thick layer of Chromium, attached to an individual SWNT (a+b), and to a MWNT (c+d) for comparison. The SWNT based device is already turned by nearly 90°, and vibrations are visible (b). No vibrations are visible for the object attached to the MWNT (c+d). Here we see that the nominally 5nm thick Cr layer, made by thermal evaporation, is not homogeneous. Scale bars are 500nm (a+c), 50nm (b), and 20nm (d).
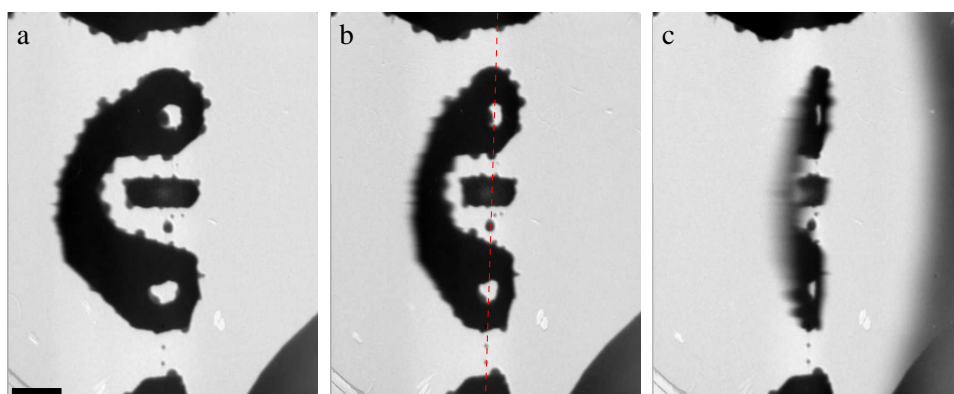
Figure 7.12: A large metal structure suspended on a small bundle of 2-4 SWNTs (a). It is turned by moving the center of the electron beam, which has the effect of charging parts of the structure (b+c). This device has already two separated components: The metal block in the center is attached to the larger structure by carbon nanotubes. This larger structure is in turn attached to the supports (visible at the top and bottom of the images). The dashed line in (b) indicates the orientation of the nanotube, which is not visible at this magnification. Scale bar is 1μm.

layer, holes are visible (no homogeneous layer is formed in the evaporation process). This object has a mass of only $\approx 10^{-17}$kg.

Much larger objects have been attached to SWNT bundles. Figure 7.12 shows a metal structure suspended on a bundle of a few nanotubes (2 tubes on one side, 4 tubes on the other side). Within the suspended structure, another metal block is held by several nanotubes. The device is turned by up to $90°$ by moving the electron beam, which has the effect of charging different parts of the structure.

The nanotube torsional pendulum can be reliably prepared by the described procedure. After preparation, most devices were mounted into the standard TEM holder for an initial check and characterization. Most devices survived up to this point. Afterwards, mounting into the sample holder with electric contacts was planned for in-situ operation, carried out in a different microscope. Now, most suspended objects had fallen off, and many devices were destroyed until we found the reason: Upon insertion into the TEM, the airlock is slowly evacuated, so that the sample is going smoothly from ambient pressure to high vacuum. On the way out of the microscope, however, the sample is subjected to a sudden change from vacuum to ambient pressure. In this process, the delicate suspended objects are blown off from their support.

7.2.9 Predicted and measured thermal oscillations

For various devices the thermal oscillations were calculated for the device geometry and also measured from TEM images. From the width of the blurred edge of the pendulum, the amplitude of the vibration is obtained. One example is shown
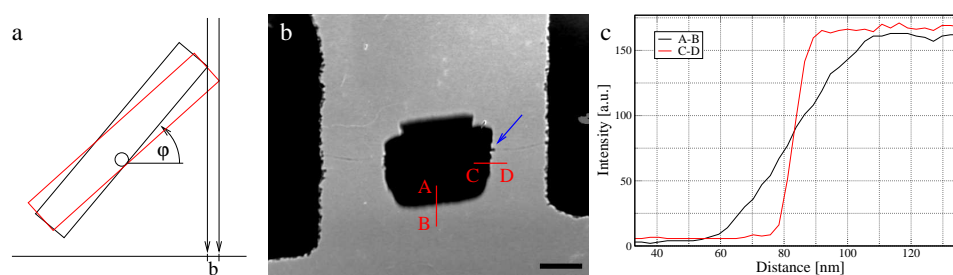
Figure 7.13: Measurement of the thermal vibration amplitude from TEM images. (a) The observed width b depends on the viewing angle on the pendulum. From the TEM image (b), two profile plots along A-B and C-D are shown in (c). The profile A-B shows the apparent width of the vibration, C-D is taken as reference. Since features close to the axis and the axis itself are much sharper (blue arrow in (b)), we conclude that we observe mainly a torsional oscillation and not a translational one. Curves in (c) are from the original image data, while the image displayed in (b) is modified in brightness and contrast. Scale bar in (b) is 200nm.

in Figure 7.13. The width of the blurred edge b depends on the angle φ of the pendulum with respect to the direction of view, and of course on the actual vibration amplitude. Several profile plots across the vibrating edge, and reference plots at different positions are taken. The angle φ is derived from the known length of the pendulum (from the lithography) and its apparent length in the TEM image. The amplitude of the torsional vibration is then deduced from the angle φ, the width of the blurred edge, and the geometry of the device. In all devices we observe that the vibrations at the outer edges of the pendulum are much larger than close to the nanotube axis. Therefore we conclude that the blurred edges are mainly due to torsional oscillations, and not to translational modes. A comparison of thermal vibrations, measured from TEM images and calculated for the device geometry, is given in table 7.1.

We see that the observed vibration is in agreement with the predictions based on the geometry of each device. For a pendulum that is turned by electrostatic attraction to a nearby electrode (Fig. 7.9), the vibration amplitude decreases as the potential is increased. At the maximum deflection, no vibration is visible any more. The electrostatic attraction strongly increases the effective spring constant.

7.2.10 Discussion

A major distinction from existing nanoelectromechanical systems is the ultra-low spring constant associated with the suspension on a single molecule. Therefore, a torsional pendulum built on a single-walled nanotube can be turned by extremely small forces. For a rotation of $1°$ a torque of $5 \cdot 10^{-20}$Nm is necessary. This corresponds to a force of 0.1pN acting on one end of the rotor 400nm away from the axis. Such a deflection could be detected by optical means, since the rotor is suffi-

Sample	03a30 (Fig. 7.8)	03a40 (Fig. 7.9)	0861 (Fig. 7.11)	1023u1
Mass [kg]	$9 \cdot 10^{-16}$	$2 \cdot 10^{-16}$	$1 \cdot 10^{-17}$	$3 \cdot 10^{-16}$
Moment of inertia [kgm^2]	$8 \cdot 10^{-29}$	$7 \cdot 10^{-30}$	$2 \cdot 10^{-31}$	$2 \cdot 10^{-29}$
Nanotube diameter [nm]	2.4	1.7	1.5	1.0
Resonance freq. (calc.) [kHz]	60	140	580	40
Calculated thermal osc. [°]	3.0 ± 0.3	4.2 ± 0.5	$6.2 \pm .7$	9 ± 1
Measured thermal osc. [°]	3.7 ± 0.8	$2.9 \pm 0.5*$	6.5 ± 1	8 ± 2

Table 7.1: Comparison of thermal oscillations in the SWNT based torsional pendulum. Values are calculated for the geometry of each device, and measured from vibrations observed in TEM images. The oscillation (*) was measured with a potential applied between the pendulum and the side electrode. Uncertainties in the calculated values arise from the not precisely known device geometry (especially nanotube diameter).

ciently large. Optical detection with nanometer sensitivity has been demonstrated for objects of similar size [106]. More intriguing however, is the possibility that the nanotube itself could be used to sense the deformation. A torsional deformation is expected to strongly influence the tube's electronic structure [107], making it possible to build a truly nano-scale force or torsion sensor that detects tiny deformations from changes in the tube's transport properties. Either way, the SWNT pendulum will be able to detect tiny forces.

Similarly, extremely small perturbances could excite a detectable torsional oscillation. We already observe the thermally excited oscillations at room temperature in the TEM as unsharp edges of the pendulum. The good agreement between observed and calculated values confirms that the modelisation of the vibrational modes is valid and the nanotubes indeed exhibit the predicted mechanical properties.

7.3   Enantiomer identification

Nanotubes (with exception of the armchair (n,n) or zigzag (n,0) types) are chiral molecules, i.e. they are not identical with their mirror objects. Normally it is not possible to determine the handedness of a nanotube from a diffraction pattern. The diffraction pattern is the Fourier transform of the projected atomic potentials, and the (n,m) nanotube, and its mirror counterpart which we will call (m,n) have the same projected potential for normal incidence.

For non-normal incidence, the projected potential is identical for the (n,m) nanotube and the (m,n) nanotube with opposite incidence angle. But in any case the diffraction pattern remains symmetric, so that the enantiomers can not be identified. It would be possible in principle to determine the enantiomer by atomic resolution TEM imaging of a tilted nanotube (with known sign and value of the
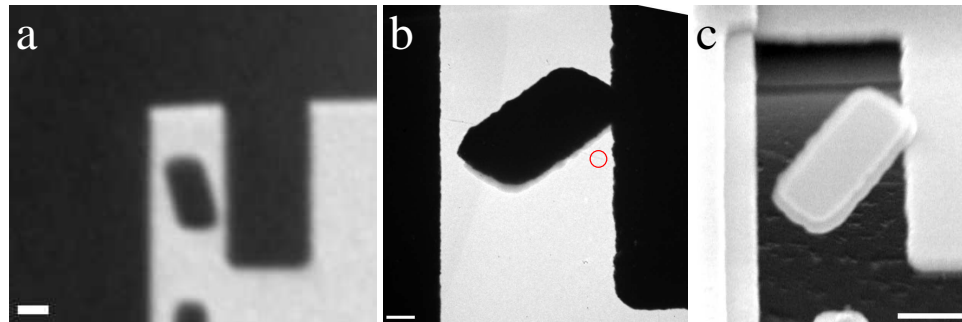
Figure 7.14: (a) Low-magnification TEM image of the as-prepared SWNT pendulum device. The metal block is freely suspended on the nanotube. (b) As the magnification is increased (leading to a higher current density of the electron beam) the object is charged, it flips by 180° and gets stuck on one of the contacts. (c) An SEM image taken afterwards clearly shows in which direction the pendulum is turned. The red circle in (b) indicates the section of the nanotube from which a diffraction pattern is obtained. This is now a diffraction pattern from a *twisted* nanotube (shown in Fig. 7.16), where one end of the 300nm long tube section is turned by nearly 180°. Scale bars: 500nm (a+c), 200nm (b).

incidence angle), or by dark-field imaging on a given diffraction peak. The latter has been demonstrated for MWNTs [45], but would be difficult for SWNTs since the diffraction intensities are extremely weak (for adjusting the objective aperture and/or illumination tilt angle for dark field imaging, the diffraction peaks must be visible on the screen or CCD).

In a SWNT torsional pendulum, the nanotube is torsionally deformed in a known direction. This literally breaks the symmetry: The two mirror-symmetric enantiomers, after deformation in a given direction, are no longer mirror-symmetric. It now becomes possible to determine which type is present by electron diffraction. This is conceptually different from the aforementioned approaches: Instead of determining the handedness in the original molecule, we remove the symmetry by a deformation and investigate the deformed molecule.

7.3.1   Experimental

For the diffraction experiment a torsional pendulum that is stuck in the fully rotated position is used. Figure 7.14 shows the sample. It allows to capture a diffraction pattern from a torsionally deformed nanotube, with a known orientation of the torsional deformation. By the turned pendulum, one end of the 300nm long tube section is rotated by nearly 180°. By comparison with simulations, the nanotube can be identified as (14,12), with a small deviation due to the deformation. Among the many diffraction patterns obtained from undeformed nanotubes within this work, we also have a diffraction pattern for an undeformed (14,12) nanotube taken under the same conditions that is used as reference.

7.3.2 Results and discussion

By twisting a nanotube, we change the angle between the graphene lattice and the nanotube axis. The torsional deformation corresponds to a shear deformation in a planar graphene sheet. Figure 7.15 illustrates the effect of a torsional deformation. The main point is that the torsionally deformed (14,12) nanotube is no longer mirror symmetric to a (12,14) nanotube deformed in the same way (it would be mirror symmetric to a (12,14) nanotube twisted in the opposite direction).

Figure 7.16 shows the diffraction pattern obtained from the twisted nanotube. The inset shows a profile plot across two diffraction peaks, and the same profile for an undeformed (14,12) and for simulated diffraction images of twisted and undeformed nanotubes. As reference length, the distance between the lines denoted by X and X' is used. In this way, the compared peak distances are independent of the incidence angle. There is clearly a deviation in the peak distances, both compared to the simulations and to the diffraction image of the undeformed nanotube. Further, the observed diffraction image agrees very well with a simulated diffraction image of a torsionally deformed (14,12) nanotube. It does not match the deformed (12,14) nanotube. This result shows that the tube is indeed homogeneously twisted (and not e.g. deformed at a single defect) and we can conclude that precisely the tube structure (14,12) is present in this device, and not its mirror counterpart.

7.4 Further in-situ experiments

7.4.1 SWNT biprism

Figure 7.17 shows two interesting effects observed in a failed SWNT pendulum device. First, the supporting nanotube survives a loss of the attached metal block. This may be possible because the oxide layer underneath the metal was completely etched away in this particular sample, so that the tube was not surrounded by material (in other samples, the tube is in-between the metal block and a remaining oxide layer, visible e.g. in Fig. 7.8c.). Second, since we have now a free-standing nanotube with a nearby electrode, the tube can be charged electrostatically. Fig. 7.17c and d show images respectively of the neutral and charged nanotube. The charged nanotube acts as biprism which focuses or de-focuses the electron beam in a direction perpendicular to the tube axis.

Further, we observe that the vibrations in the free-standing tube section are strongly reduced by applying the potential, which is due to the electrostatic attraction towards the side electrode. Diffraction images were obtained for the positively and negatively charged tube. No difference was observed in these diffraction patterns. However, if more charge can be induced on the tube (e.g. by a closer nearby electrode) this could provide a way to measure the charge-induced bond length change predicted for single-walled carbon nanotubes [108, 109].
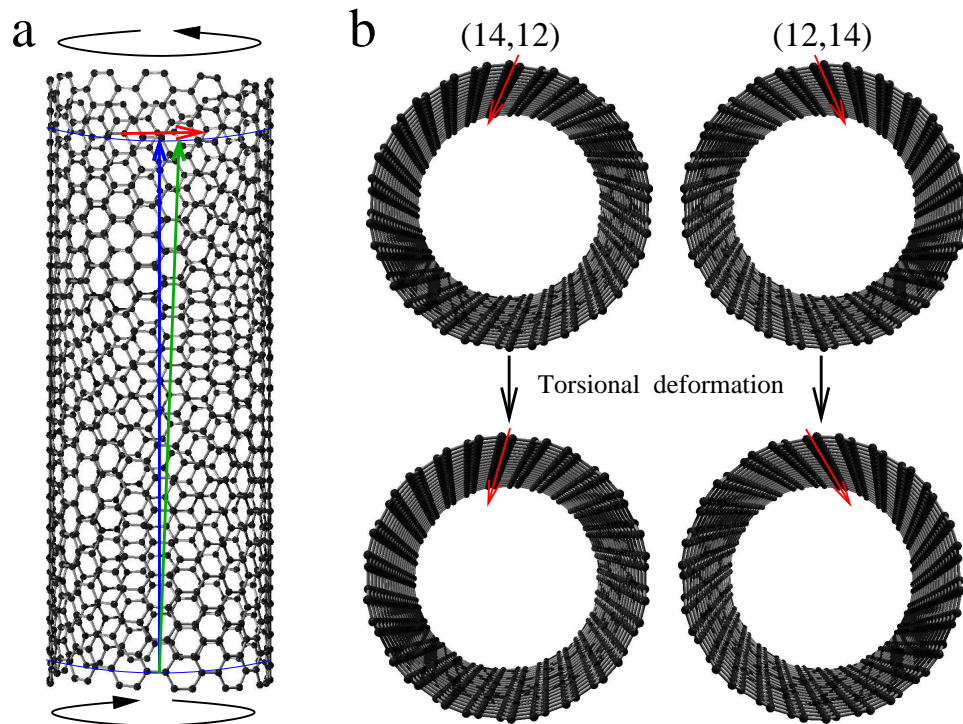
Figure 7.15: (a) Modelisation of the torsional deformation. The shear deformation of the graphene sheet turns the blue arrow towards the green arrow. The atoms are displaced along lines around the circumference only. (b) Effect of torsional deformation on the enantiomers of a (14,12) nanotube, viewed along the nanotube. Without deformation, the angle between the nanotube axis and one of the main directions along the graphene lattice shown here is the same for the (14,12) and (12,14) nanotubes. This line along the graphene sheet continues in a helix- or screw-like line around the nanotube cylinder. By twisting the nanotube, this angle, or the pitch of the helix, is changed. For a deformation in a given direction, the sign of this change is different for each enantiomer. The twisted (14,12) is no longer mirror symmetric to the twisted (12,14).
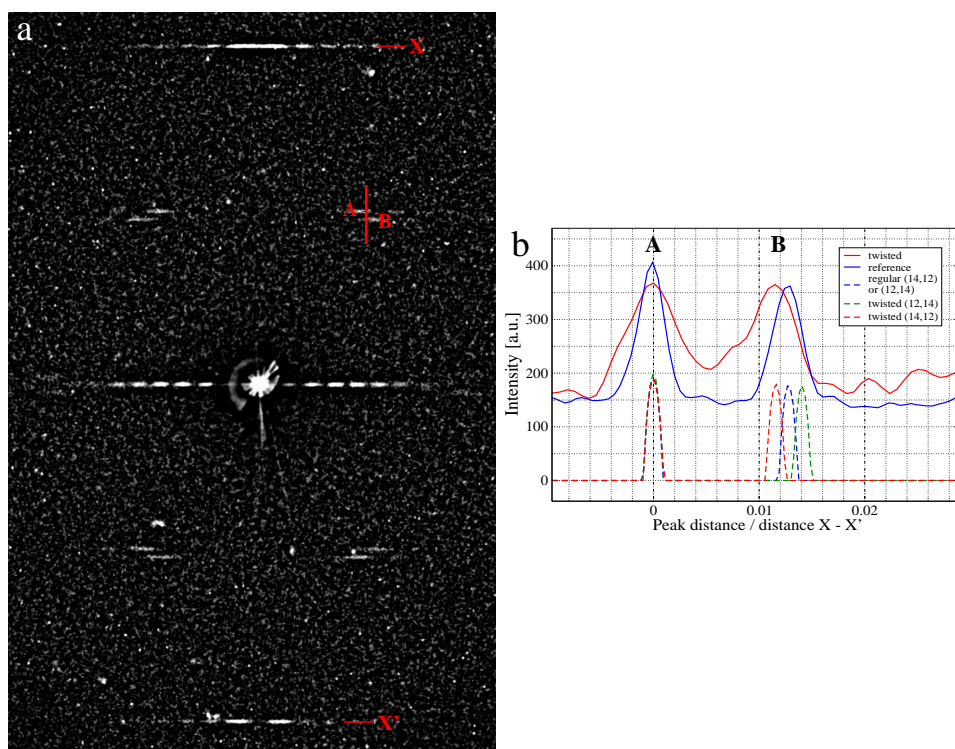
Figure 7.16: (a) Diffraction pattern obtained from a twisted SWNT. (b) Profile across A-B in the diffraction pattern (solid red line) and in a diffraction pattern of an undeformed (14,12) nanotube (solid blue line). The dashed lines are from simulated diffraction images of torsionally deformed (14,12) nanotubes, twisted in the same direction and magnitude as in our device. All A peaks are plotted at x=0 in (b). The clear difference in the peak distances makes it possible to determine which enantiomer is present. Since the direction of the twist is known, we can determine that precisely the tube structure (14,12) is present in this device, and not its mirror counterpart.
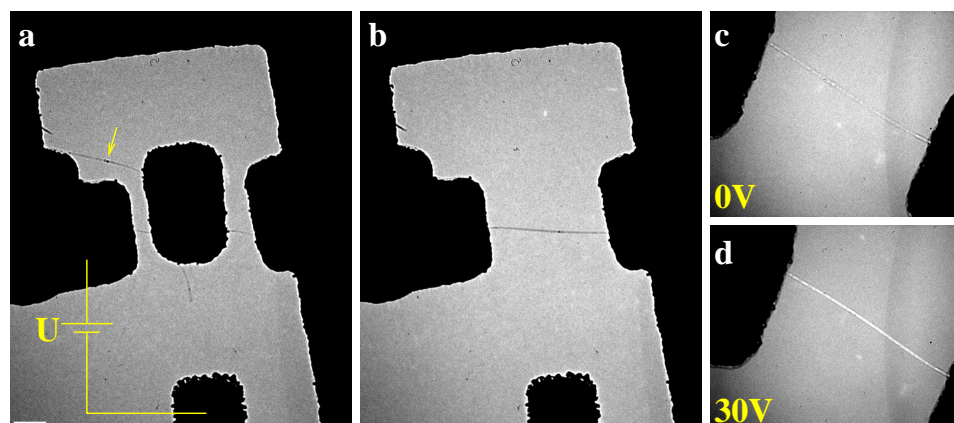
Figure 7.17: (a) A SWNT torsional pendulum which is blocked by an additional carbon nanotube between the support and the moving part (arrow). The potential is applied between the pendulum and the nearby electrode as indicated. Scale bar is 200nm. (b) Attempting to move the pendulum by high and abruptly changing fields results in a loss of the metal block. Surprisingly, the nanotube remains intact. (c+d) The nanotube can now be charged by applying a voltage between the support and the nearby electrode. The charged tube acts as biprism and focuses the electron beam (d). In images (c+d) the microscope is defocused in order to observe the biprism effect.

7.4.2 Suspended nanospheres

Objects suspended on SWNTs can be significantly heated by electron irradiation in the TEM. The gold structure reaches a liquid phase and forms a nearly spherical object. The silicon dioxide part of the structure retains its original shape. Figure 7.18 shows a single molecule torsional pendulum where the moving part was melted by electron irradiation. The object can still be turned by electrostatic attraction.

Another observation on this and other melted objects are the metal nanoparticles that condense near the supporting structure (Fig. 7.18c+d). The nanotubes get hottest near the center, but the ends remain cold. Thus, the metal condenses only at the outer ends of the tubes, not near the suspended, heated object. Afterwards, the nanotubes appear very clean, presumably because many contaminations have been evaporated.

Figure 7.19 shows a series of images obtained during melting of a suspended object by electron irradiation. The melting metal forms a nearly spherical structure, only disturbed by some remaining silicon dioxide.

Higher intensities are required to melt objects attached to many carbon nanotubes. This clearly shows that the main path of thermal dissipation is along the tubes, and not by radiation. Objects which are in touch with the supporting structure (similar to Fig. 7.14), or attached on large bundles, can not be melted at all. We conclude that in the equilibrium, the object is heated by the beam, and the heat
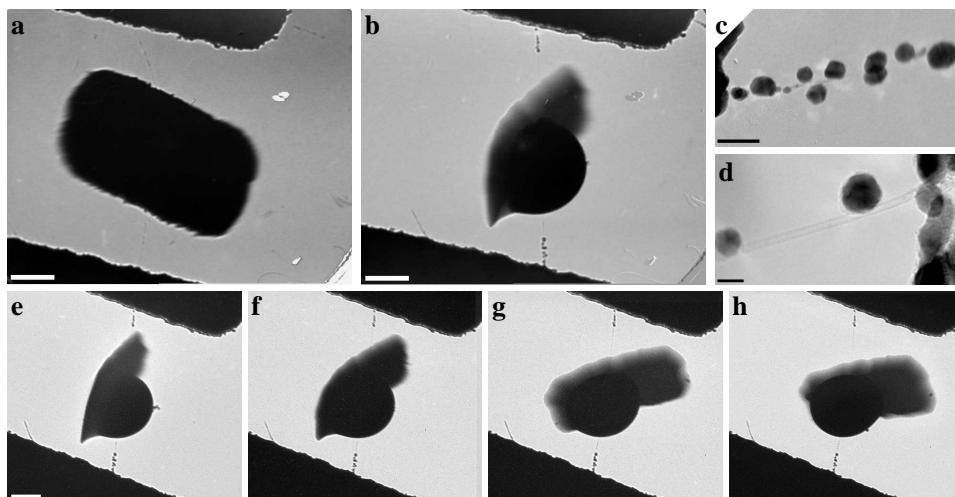
Figure 7.18: A suspended object before (a) and after (b) melting due to electron irradiation. The gold structure melts into a nearly spherical object, while the silicon dioxide layer remains in its shape. (c+d) Some of the metal condenses into small clusters near the cold ends of the nanotube. The resulting object can still be actuated by the electric field (e-h). Scale bars: 200nm (a,b,e), 20nm (c), 5nm (d).
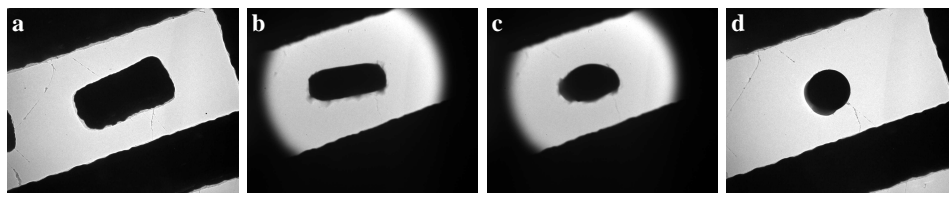

Figure 7.19: Melting of an object suspended on three nanotubes by electron irradiation. (a) Before, (b+c) during irradiation with increasing dose, (d) afterwards. Scale bar, 500nm.

is dissipated mainly along the nanotubes.

Thus, one would expect that the thermal conductivity of SWNTs can be obtained from these experiments. We know the melting point of gold, and we observe the beam intensity where the melting point is reached. In this moment the power which is heating the object is dissipated along a known temperature difference. The suspended object is at the melting temperature of gold, and the support is at room temperature. We can also estimate the number and length of the nanotubes from TEM images. However, melting of ~20 suspended objects revealed that the beam power required for melting varies by up to an order of magnitude for objects suspended on the same number of tubes. It seems that there are huge variations in the thermal contact between the object and the tube - very similar to the large variations in electric contact resistances observed in transport measurements.

7.5   Conclusions

We have built versatile novel nanoscale devices that are potentially useful in nanoscale mechanical systems for both basic research as well as practical applications. We have reached the single-molecule level for the motion-enabling element in our NEMS. Our SWNT pendulum can be reproducibly turned to any position between 0° and almost 180° using a single electrostatic potential. Among obvious NEMS applications, they could serve as a micromirror in various optical applications. Further, the device would allow a continuous tilting of any object attached to the nanotube or the pendulum, with a precisely defined rotation axis. This can be useful for tomography in a TEM or x-ray microscope. Deflections and oscillations can be induced by extremely small forces, which will make it possible to build very sensitive nanoscale force sensors. Devices with varying geometry, and a simple multi-component device demonstrate the potential for a flexible design of more complex nanoelectromechanical systems based on carbon nanotubes.

Chapter 8

Summary, conclusions and outlook

A range of different measurements were carried out on individual carbon nanotubes which were precisely characterized by electron diffraction and high-resolution transmission electron microscopy. We have obtained structural information in combination with electronic and vibrational properties from the very same molecule. This was achieved by the development of a novel and versatile procedure for preparing free-standing lithographically defined structures. Further, novel devices for in-situ transport measurements, and nanoelectromechanical devices that contain individual single-walled nanotubes as key motion-enabling element, were developed.

Our combination of Raman spectroscopy and electron diffraction provides the first measurements of vibrational properties of carbon nanotubes where the structural information is determined independently, and not derived through a modelization from spectroscopic information. This is important because as long as the structure is deduced via modelization, a verification of the model is not possible. Further, the index assignment only from Raman spectroscopic data is only possible for small diameter nanotubes. We have measured the radial breathing mode frequency dependence on the nanotube diameter for a large diameter range, and find that the previously established relationships can not be extended to the larger diameter nanotubes. Also, our measurements are done on freely suspended nanotubes, so that an influence from the environment (substrate, suspension) can be excluded. Yet, we find a surprisingly good agreement with previous work with nanotubes on substrates or in suspension, showing that the effect of the environment is much smaller than previously assumed. The diameter dependence of the tangential mode frequencies, and the deviations between measured and calculated transition energies, agree with previous work; although additional data especially from smaller diameter nanotubes is desirable for a more quantitative comparison.

Transport measurements were carried out in combination with an electron microscopic analysis in different ways. For analyzing the electronic properties of a

carbon nanotube, it is important set up a transistor configuration with an effective gate electrode. The solution which provides the most effective gate, but also the most labor-intensive one, is to measure the transport properties on the substrate before etching, and analyze the tube by TEM after etching. Here, the highly doped substrate serves as gate, separated from the nanotube by an oxide layer. High-resolution images can show whether a nanotube is filled with fullerenes or not. Preparing samples so that the transport and TEM measurements are done on free-standing nanotubes requires less lithography and AFM work, but the substrate or nearby metallic electrode is less effective as gate. We have measured the electronic properties of nanotubes of which the indices were determined by electron diffraction. The metallic or semiconducting behaviour as predicted for the given indices was confirmed by the transport measurement. In-situ transport measurements show modifications of the contact by irradiation and currents. We observe joule heating of the free-standing nanotube to high temperatures by passing a current, seen as modifications of the catalyst particles and amorphous carbon on the tube.

A variety of nanoscale electromechanical devices based on carbon nanotubes were demonstrated. Multi-shell nanotubes, small bundles and even individual nanotube molecules serve as spring and mechanical support for lithographically defined moving parts. The single-molecule based pendulum can be turned to any position between 0° and almost 180° with the use of a single electrostatic potential. Possible nanoelectromechanical systems applications include micromirrors or other devices that require a continuous tilting with a precisely defined rotation axis of an object attached to the nanotube. Deflections and oscillations can be induced by extremely small forces, so that the devices may also serve as very sensitive nanoscale force sensors. We observe the thermally excited oscillations at room temperature. The torsional deformation of a chiral molecule lifts the mirror symmetry between the enantiomers, which allows a determination of its handedness.

As outlook, further measurements could be carried out on precisely identified carbon nanotubes. The presently investigated samples comprised mostly larger diameter nanotubes, while e.g. effects of curvature in the graphene sheet will be more dominant in smaller diameter samples. The Raman studies could be extended towards a measurement of the transition energies, if many closely spaced excitation lines were available. This would allow a direct comparison with calculated electronic properties of a particular nanotube structure. Further, fluorescence spectroscopy should be possible, in the same way as Raman spectroscopy, to gain additional information on a specific nanotube's electronic properties. Transport measurements could be improved by using other contact materials for lower contact resistances, and by designing a more effective gate electrode in case of the free-standing nanotubes. Concerning the nanoelectromechanical systems, it is certainly desirable to measure directly the mechanical resonances by an A.C. excitation and in-situ observation of the resonances. For the single-molecule torsional pendulum, a transport measurement through the torsionally deformed tube is envisaged.

Bibliography

[1] Sumio Iijima and Toshinari Ichihashi. Single-shell carbon nanotubes of 1-nm diameter. *Nature*, 363:603–605, 1993.

[2] N. Hamada, S. Sawada, and A. Oshiyama. New one-dimensional conductors: Graphitic microtubules. *Phys. Rev. Lett.*, 68:1579, 1992.

[3] J. W. G. Wildoer, L. C. Venema, A. G. Rinzler, R. E. Smalley, and C. Dekker. Electronic structure of atomically resolved carbon nanotubes. *Nature*, 391:59, 1998.

[4] T. W. Odom, J. L. Huang, P. Kim, and C. M. Lieber. Atomic structure and electronic properties of single-walled carbon nanotubes. *Nature*, 391:62, 1998.

[5] L. C. Venema, V. Meunier, P. Lambin, and C. Dekker. Atomic structure of carbon nanotubes from scanning tunneling microscopy. *Phys. Rev. B*, 61:2991, 2000.

[6] L. Vitali, M. Burghard, M. A. Schneider, L. Liu, S. Y. Wu, C. S. Jayanthi, and K. Kern. Phonon spectromicroscopy of carbon nanostructures with atomic resolution. *Phys. Rev. Lett.*, 93:136103, 2004.

[7] A. Hashimoto, K. Suenaga, A. Gloter, K. Urita, and S. Iijima. Direct evidence for atomic defects in graphene layers. *Nature*, 430:870, 2004.

[8] A. Hashimoto, K. Suenaga, K. Urita, T. Shimada, T. Sugai, S. Bandow, H. Shinohara, and S. Iijima. Atomic correlation between adjacent graphene layers in double-wall carbon nanotubes. *Phys. Rev. Lett.*, 94:045504, 2005.

[9] R. R. Meyer, S. Friedrichs, A. I. Kirkland, J. Sloan, J. L. Hutchinson, and M. L. H. Green. A composite method for the determination of the chirality of single-walled carbon nanotubes. *J. Microsc.*, 212:152, 2003.

[10] A. A. Lucas, V. Bruyninckx, and Ph. Lambin. Calculating the diffraction of electrons or x-rays by carbon nanotubes. *Europhys. Lett.*, 35:355, 1996.

[11] Ph. Lambin and A. A. Lucas. Quantitative theory of diffraction by carbon nanotubes. *Phys. Rev. B*, 56:3571, 1997.

[12] A. A. Lucas, V. Bruyninckx, Ph. Lambin, D. Bernaerts, S. Amelinckx, J. Van Landuyt, and G. Van Tendeloo. Electron diffraction by carbon nanotubes. *Scanning Microscopy*, 12:415, 1997.

[13] L.-C. Qin. Electron diffraction from cylindrical nanotubes. *J. Mater. Res.*, 9:2450, 1994.

[14] L.-C. Qin. Measuring the true helicity of carbon nanotubes. *Chem. Phys. Lett.*, 297:23, 1998.

[15] A. A. Lucas and P. Lambin. Diffraction by dna, carbon nanotubes and other helical nanostructures. *Rep. Prog. Phys.*, 68:1181, 2005.

[16] R. Saito, G. Dresselhaus, and M. S. Dresselhaus. *Physical Properties of Carbon Nanotubes*. Imperial College Press, London, 1998.

[17] S. Maruyama. Kataura plot and 1D electronic DOS of carbon nanotubes, 2002. http://reizei.t.u-tokyo.ac.jp/ maruyama/kataura/kataura.html.

[18] C. L. Kane and E. J. Mele. Size, shape, and low energy electronic structure of carbon nanotubes. *Phys. Rev. Lett.*, 78:1932, 1997.

[19] M. Ouyang, J.-L. Huang, C. L. Cheung, and C. M. Lieber. Energy gaps in "metallic" single-walled carbon nanotubes. *Science*, 292:702, 2001.

[20] S. Frank, P. Poncharal, Z. L. Wang, and W. A. de Heer. Carbon nanotube quantum resistors. *Science*, 280:1744, 1998.

[21] A. Bachtold, M. S. Fuhrer, S. Plyasunov, M. Forero, E. H. Anderson, A. Zettl, and P. L. McEuen. Scanned probe microscopy of electronic transport in carbon nanotubes. *Phys. Rev. Lett.*, 84:6082, 2000.

[22] A. Javey, J. Guo, Q. Wang, M. Lundstrom, and H. Dai. Ballistic carbon nanotube field-effect transistors. *Nature*, 424:654, 2003.

[23] M. Bockrath, W. Liang, D. Bozovic, J. H. Hafner, C. M. Lieber, M. Tinkham, and H. Park. Resonant electron scattering by defects in single-walled carbon nanotubes. *Science*, 291:291, 2001.

[24] J. Appenzeller, J. Knoch, V. Derycke, R. Martel, and Ph. Avouris. Field-modulated carrier transport in carbon nanotube transistors. *Phys. Rev. Lett.*, 89:126801, 2002.

[25] M. Paillet, V. Jourdain, P. Poncharal, J.-L. Sauvajol, A. Zahab, J. C. Meyer, S. Roth, N. Cordente, C. Amiens, and B. Chaudret. Versatile synthesis of individual single-walled carbon nanotubes from nickel nanoparticles for the study of their physical properties. *J. Phys. Chem. B*, 108:17112–17118, 2004.

[26] M. Paillet, V. Jourdain, P. Poncharal, J.-L. Sauvajol, A. Zahab, J. C. Meyer, S. Roth, N. Cordente, C. Amiens, and B. Chaudret. Growth and physical properties of individual single-walled carbon nanotubes. *Diamond and Related Materials*, 14:1426, 2005.

[27] R. Seidel, G. S. Duesberg, E. Unger, A. P. Graham, M. Liebau, and F. Kreupl. Chemical vapor deposition growth of single-walled carbon nanotubes at 600°c and simple growth model. *J. Phys. Chem. B*, 108:1888, 2004.

[28] H. Telg, J. Maultzsch, S. Reich, F. Hennrich, and C. Thomsen. Chirality distribution and transition energies of carbon nanotubes. *Phys. Rev. Lett.*, 93:177401, 2004.

[29] A. Jorio, R. Saito, J. H. Hafner, C. M. Lieber, M. Hunter, T. McClure, G. Dresselhaus, and M. S. Dresselhaus. Structural (n,m) determination of isolated single-wall carbon nanotubes by resonant raman scattering. *Phys. Rev. Lett.*, 86:1118, 2001.

[30] S. M. Bachilo, M. S. Strano, C. Kittrell, R. H. Hauge, R. E. Smalley, and R. B. Weisman. Structure-assigned optical spectra of single-walled carbon nanotubes. *Science*, 298:2361, 2002.

[31] S. M. Bachilo, L. Balzano, J. E. Herrera, F. Pompeo, D. E. Resasco, and R. B. Weisman. Narrow (n,m)-distribution of single-walled carbon nanotubes grown using a solid supported catalyst. *J. Am. Chem. Soc.*, 125:11186, 2003.

[32] Y. Miyauchi, S. Chiashi, Y. Murakami, Y. Hayashida, and S. Maruyama. Fluorescence spectroscopy of single-walled carbon nanotubes synthesized from alcohol. *Chem. Phys. Lett.*, 387:198, 2004.

[33] M. Machon, S. Reich, H. Telg, J. Maultzsch, P. Ordejon, and C. Thomsen. Strength of radial breathing mode in single-walled carbon nanotubes. *Phys. Rev. B*, 71:035416, 2005.

[34] R. Gevers and M. David. Relativistic theory of electron and position diffraction at high and low energy. *Phys. Stat. Sol.*, 113:665, 1962.

[35] C. J. Humphreys. The scattering of fast electrons by crystals. *Rep. Prog. Phys. 42*, 42:1825, 1979.

[36] J. C. H. Spence. *High-Resolution Electron Microscopy*. Oxford University Press, 2003.

[37] P. R. Buseck, J. M. Cowley, and L. Eyring. *High-Resolution Transmission Electron Microscopy*. Oxford University Press, 1988.

[38] R. P. Feynman. Space-time approach to non-relativistic quantum mechanics. *Rev. Mod. Phys.*, 20:367, 1948.

[39] R. P. Feynman and A. R. Hibbs. *Quantum Mechanics and Path Integrals.* McGraw-Hill, New York, 1965.

[40] L.-M. Peng. Electron atomic scattering factors and scattering potentials of crystals. *micron*, 30:625, 1999.

[41] P. A. Doyle and P. S. Turner. Relativistic hartree-fock x-ray and electron scattering factors. *Acta Cryst. A*, 24:390, 1968.

[42] O. Scherzer. The theoretical resolution limit of the electron microscope. *J. Appl. Phys.*, 20:20, 1949.

[43] X. F. Zhang, X. B. Zhang, G. Van Tendeloo, S. Amelinckx, M. Op de Beeck, and J. Van Landuyt. Carbon nano-tubes; their formation process and observation by electron microscopy. *J. Cryst. Growth*, 130:368, 1993.

[44] X. B. Zhang, X. F. Zhang, S. Amelinckx, G. Van Tendeloo, and J. Van Landuyt. The reciprocal space of carbon nanotubes: a detailed interpretation of the electron diffraction effects. *Ultramicr.*, 54:237, 1994.

[45] S. Amelinckx, A. Lucas, and P. Lambin. Electron diffraction and microscopy of nanotubes. *Rep. Prog. Phys.*, 62:1471, 1999.

[46] J. M. Cowley and F. A. Sundell. Nanodiffraction and dark-field stem characterization of single-walled carbon nanotube ropes. *Ultramicr.*, 68:1, 1997.

[47] L.-C. Qin, S. Iijima, H. Kataura, Y. Maniwa, S. Suzuki, and Y. Achiba. Helicity and packing of single-walled carbon nanotubes studied by electron nanodiffraction. *Chem. Phys. Lett.*, 268:101, 1997.

[48] J. M. Cowley, P. Nikolaev, A. Thess, and R. E. Smalley. Electron nanodiffraction study of carbon single-walled nanotube ropes. *Chem. Phys. Lett.*, 265:379, 1997.

[49] D. Bernaerts, A. Zettl, N. G. Chopra, A. Thess, and R. E. Smalley. Electron diffraction study of single-wall carbon nanotubes. *Solid State Commun.*, 105:145, 1997.

[50] R. R. He, H. Z. Jin, J. Zhu, Y. J. Yan, and X. H. Chen. Physical and electronic structure in carbon nanotubes. *Chem. Phys. Lett.*, 298:170, 1998.

[51] H.-Z. Jin, R.-H. He, and J. Zhu. Helicity and inter-tube bonding in bundles of single-walled carbon nanotubes. *J. Electron Microsc.*, 48:339, 1999.

[52] L. Henrard, A. Loiseau, C. Journet, and P. Bernier. Study of the symmetry of single-wall nanotubes by electron diffraction. *Eur. Phys. J. B*, 13:661, 2000.

[53] J.-F. Colomer, L. Henrard, Ph. Lambin, and G. Van Tendeloo. Electron diffraction study of small bundles of single-wall carbon nanotubes with unique helicity. *Phys. Rev. B*, 64:125425, 2001.

[54] J.-F. Colomer, L. Henrard, Ph. Lambin, and G. Van Tendeloo. Electron diffraction and microscopy of single-wall carbon nanotube bundles produced by different methods. *Eur. Phys. J. B*, 27:111, 2002.

[55] J.-F. Colomer, L. Henrard, P. Launois, G. Van Tendeloo, A. A. Lucas, and Ph. Lambin. Interpretation of electron diffraction from carbon nanotube bundles presenting precise helicity. *Phys. Rev. B*, 70:075408, 2004.

[56] L. C. Qin, T. Ichihashi, and S. Iijima. On the measurement of helicity of carbon nanotubes. *Ultramicr.*, 67:181, 1997.

[57] M. Gao, J. M. Zuo, R. D. Twesten, I. Petrov, L. A. Nagahara, and R. Zhang. Structure determination of individual single-wall carbon nanotubes by nanoarea electron diffraction. *Appl. Phys. Lett.*, 82:2703, 2003.

[58] B. W. Smith and E. Luzzi. Electron irradiation effects in single wall carbon nanotubes. *J. Appl. Phys.*, 90:3509, 2001.

[59] P. M. Ajayan, V. Ravikumar, and J.-C. Charlier. Surface reconstruction and dimensional changes in single-walled carbon nanotubes. *Phys. Rev. Lett.*, 81:1437, 1998.

[60] J. M. Zuo, I. Vartanyants, M. Gao, R. Zhang, and L. A. Nagahara. Atomic resolution imaging of a carbon nanotube from diffraction intensities. *Science*, 300:1419, 2003.

[61] M. Kociak, K. Hirahara, K. Suenaga, and S. Iijima. How accurate can the determination of chiral indices from of carbon nanotubes be? *Eur. Phys. J. B.*, 32:457, 2003.

[62] K. Hirahara, K. Suenaga, S. Bandow, H. Kato, T. Okazaki, H. Shinohara, and S. Iijima. One-dimensional metallofullerene crystal generated inside single-walled carbon nanotubes. *Phys. Rev. Lett.*, 85:5384, 2000.

[63] K. Hirahara, S. Bandow, K. Suenaga, H. Kato, T. Okazaki, H. Shinohara, and S. Iijima. Electron diffraction study of one-dimensional crystals of fullerenes. *Phys. Rev. B*, 64:115420, 2001.

[64] Stephanie Reich, Christian Thomsen, and Janina Maultzsch. *Carbon nanotubes. Basic Concepts and Physical Properties*. Wiley-VCH, Weinheim, Germany, 2004.

[65] M.S. Dresselhaus, G. Dresselhaus, R. Saito, and A. Jorio. Raman spectroscopy of carbon nanotubes. *Physics Report*, 409:47, 2005.

[66] J. Kürti, G. Kresse, and H. Kuzmany. First-principles calculations of the radial breathing mode of single-wall carbon nanotubes. *Phys. Rev. B*, 58:R8869, 1998.

[67] D. Sánchez-Portal, E. Artacho, J. M. Soler, A. Rubio, and P. Ordejón. Ab initio structural, elastic, and vibrational properties of carbon nanotubes. *Phys. Rev. B.*, 59:12678, 1999.

[68] C. Fantini, A. Jorio, M. Souza, M. S. Strano, M. S. Dresselhaus, , and M. A. Pimenta. Optical transition energies for carbon nanotubes from resonant raman spectroscopy: Environment and temperature effects. *Phys. Rev. Lett.*, 93:147406, 2004.

[69] A. Jorio, C. Fantini, M.A. Pimenta, R.B. Capaz, Ge. G Samsonidze, G. Dresselahaus, M.S. Dresselhaus, J. Jiang, N. Kobayashi, A. Grüneis, , and R. Saito. Resonance raman spectroscopy (n,m)-dependent effects in small-diameter single-wall carbon nanotubes. *Phys. Rev. B*, 71:075401, 2005.

[70] Y. Zhang and H. Dai. Formation of metal nanowires on suspended single-walled carbon nanotubes. *Appl. Phys. Lett.*, 77:3015, 2000.

[71] Y. Zhang, N. W. Franklin, R. J. Chen, and H. Dai. Metal coating on suspended carbon nanotubes and its implication to metal-tube interaction. *Chem. Phys. Lett.*, 331:35, 2000.

[72] O. Dubay, G. Kresse, and H. Kuzmany. Phonon softening in metallic nanotubes by a peiers-like mechanism. *Phys. Rev. Lett.*, 88:235506, 2002.

[73] S. B. Cronin, A. K. Swan, M. S. Ünlü, B. B. Goldberg, M .S. Dresselhaus, and M. Tinkham. Measuring the uniaxial strain of individual single-wall carbon nanotubes: Resonance raman spectra of atomic-force-microscope modified single-wall nanotubes. *Phys. Rev. Lett.*, 93:167401, 2004.

[74] S. B. Cronin, A. K. Swan, M. S. Ünlü, B. B. Goldberg, M .S. Dresselhaus, and M. Tinkham. Resonant raman spectroscopy of individual metallic and semiconducting single-walled carbon nanotubes under uniaxial strain. *Phys. Rev. B*, 72:035425, 2005.

[75] A. Jorio, A. G. S. Filho, G. Dresselhaus, M. S. Dresselhaus, A. K. Swan, M. S. Ünlü, B. B. Goldberg, M. A. Pimenta, J. H. Hafner, C. M. Lieber, and R. Saito. G-band resonant raman study of 62 isolated single-wall carbon nanotubes. *Phys. Rev. B*, 65:155412, 2002.

[76] H. Kataura, Y. Kumazawa, Y. Maniwa, S. Suzuki, Y. Ohtsuka, and Y. Achiba. Optical properties of single-wall carbon nanotubes. *Synth. Met.*, 103:2555–2558, 1999.

[77] R. Saito, A. Jorio, C. M. Lieber, M. Hunter, T. McClure, G. Dresselhaus, and M. S. Dresselhaus. Chirality-dependent g-band raman intensities of carbon nanotubes. *Phys. Rev. B*, 64:085312, 2001.

[78] A. Yu. Kasumov, R. Deblock, M. Kociak, B. Reulet, H. Bouchiat, I. I. Khodos, Yu. B. Gorbatov, V. T. Volkov, C. Journet, and M. Burghard. Supercurrents through single-walled carbon nanotubes. *Science*, 284:1508–1511, 1999.

[79] M. Kociak, K. Suenaga, K. Hirahara, Y. Saito, T. Nakahira, and S. Iijima. Linking chiral indices and transport properties of double-walled carbon nanotubes. *Phys. Rev. Lett*, 89:155501, 2002.

[80] J. Lee, H. Kim, S.-J. Kahng, G. Kim, Y.-W. Son, J. Ihm, H. Kato, Z. W. Wang, T. Okazaki, H. Shinohara, and Y. Kuk. Bandgap modulation of carbon nanotubes by encapsulated metallofullerenes. *Nature*, 415:1005, 2002.

[81] T. Shimada, T. Okazaki, R. Taniguchi, T. Sugai, H. Shinohara, K. Suenaga, Y. Ohno, S. Mizuno, S. Kishimoto, and T. Mizutani. Ambipolar field-effect transistor behavior of $Gd@C_{82}$ metallofullerene peapods. *Appl. Phys. Lett.*, 81:4067, 2002.

[82] H. Huang, S. H. Yang, and X. Zhang. Magnetic properties of heavy rare-earth metallofullerenes $M@C_{82}$ ($M = Gd$, Tb, Dy, Ho, and Er). *J. Phys. Chem. B*, 104:1473, 2000.

[83] K. Hirahara, K. Suenaga, S. Bandow, H. Kato, T. Okazaki, H. Shinohara, and S. Iijima. One-dimensional metallofullerene crystal generated inside single-walled carbon nanotubes. *Phys. Rev. Lett.*, 85:5384, 2000.

[84] K. Suenaga, M. Tencé, C. Mory, C. Colliex, H. Kato, T. Okazaki, H. Shinohara, K. Hirahara, S. Bandow, and S. Iijima. Element-selective single atom imaging. *Science*, 290:2280, 2000.

[85] B. Babić, M. Iqbal, and C. Schönenberger. Ambipolar field-effect transistor on as-grown single-wall carbon nanotubes. *Nanotechnology*, 14:327, 2003.

[86] A. Javey, M. Shim, and H. Dai. Electrical properties and devices of large-diameter single-walled carbon nanotubes. *Appl. Phys. Lett.*, 80:1064, 2002.

[87] C. L. Kane and E. J. Mele. Size, shape, and low energy electronic structure of carbon nanotubes. *Phys. Rev. Lett.*, 78:1932, 1997.

[88] C. Zhou, J. Kong, and H. Dai. Intrinsic electrical properties of individual single-walled carbon nanotubes with small band gaps. *Phys. Rev. Lett.*, 84:5604, 2000.

[89] R. Martel, V. Derycke, C. Lavoie, J. Appenzeller, K. K. Chan, J. Tersoff, and Ph. Avouris. Ambipolar electrical transport in semiconducting single-wall carbon nanotubes. *Phys. Rev. Lett.*, 87:256805, 2001.

[90] S. M. Sze. *Physics of semiconductor devices*. John Wiley & Sons, New York, 1981.

[91] D. E. Johnston, M. F. Islam, A. G. Yodh, and A. T. Johnson. Electronic devices based on purified carbon nanotubes grown by high-pressure decomposition of carbon monoxide. *Nature materials*, 4:589, 2005.

[92] J. R. Barnes, A. C. F. Hoole, M. P. Murrell, M. E. Welland, A. N. Broers, J. P. Bourgoin, H. Biebuyck, M. B. Johnson, and B. Michel. Characterization of electron beam induced modification of thermally grown sio$_2$. *Appl. Phys. Lett.*, 67:1538, 1995.

[93] P. A. Williams, S. J. Papadakis, A. M. Patel, M. R. Falvo, S. Washburn, and R. Superfine. Fabrication of nanometer-scale mechanical devices incorporating individual multiwalled carbon nanotbubes as torsional springs. *Appl. Phys. Lett.*, 82:805, 2003.

[94] S. J. Papadakis, A. R. Hall, P. A. Williams, L. Vicci, M. R. Falvo, R. Superfine, and S. Washburn. Resonant oscillators with carbon-nanotube torsion springs. *Phys. Rev. Lett.*, 93:146101, 2004.

[95] A. M. Fennimore, T. D. Yuzvinsky, Wei-Qiang Han, M. S. Fuhrer, J. Cumings, and A. Zettl. Rotational actuators based on carbon nanotubes. *Nature*, 424:408, 2003.

[96] B. Bourlon, D. C. Glattli, C. Miko, L. Forro, and A. Bachtold. Carbon nanotube based bearing for rotational motions. *Nano Letters*, 4:709, 2004.

[97] J. Cumings and A. Zettl. Low-friction nanoscale linear bearing realized from multiwall carbon nanotubes. *Science*, 289:602, 2000.

[98] Z. L. Wang, P. Poncharal, and W. A. de Heer. Measuring physical and mechanical properties of individual carbon nanotubes by in situ tem. *Journal of Physics and Chemistry of Solids*, 61:1025, 2000.

[99] S. W. Lee, D. S. Lee, R. E. Morjan, S. H. Jhang, M. Svenigsson, O. A. Nerushev, Y. W. Park, and E. E. B. Campbell. A three-terminal carbon nanorelay. *Nano Lett.*, 4:2027, 2004.

[100] V. Sazonova, Y. Yaish, H. Üstünel, D. Roundy, T. A. Arias, and P. L. McEuen. A tunable carbon nanotube electromechanical oscillator. *Nature*, 431:284, 2004.

[101] E. D. Minot, Y. Yaish, V. Sazonova, J.-Y. Park, M. Brink, and P. L. McEuen. Tuning carbon nanotube band gaps with strain. *Phys. Rev. Lett.*, 90:156401, 2003.

[102] Y. J. Jung, Y. Homma, R. Vajtai, Y. Kobayashi, T. Ogino, and P. M. Ajayan. Straightening suspended single-walled carbon nanotubes by ion irradiation. *Nano Lett.*, 4:1109, 2004.

[103] T. D. Yuzvinsky, A. M. Fennimore, W. Mickelson, C. Esquivias, and A. Zettl. Precision cutting of nanotubes with a low-energy electron beam. *Appl. Phys. Lett.*, 86:053109, 2005.

[104] J. P. Lu. Elastic properties of carbon nanotubes and nanoropes. *Phys. Rev. Lett.*, 79:1297, 1997.

[105] R. G. Knobel and A. N. Cleland. Nanometre-scale displacement sensing using a single electron transistor. *Nature*, 424:291, 2003.

[106] D. W. Carr, S. Evoy, L. Sekaric, H. G. Craighead, and J. M. Parpia. Measurement of mechanical resonance and losses in nanometer scale silicon wires. *Appl. Phys. Lett.*, 75:920, 1999.

[107] A. Pantano, D. M. Parks, M. C. Boyce, and M. Buongiorno Nardelli. Mixed finite element-tight-binding electromechanical analysis of carbon nanotubes. *J. Appl. Phys.*, 96:6756, 2004.

[108] G. Sun, J. Kurti, M. Kertesz, and R. H. Baughman. Dimensional changes as a function of charge injection in single-walled carbon nanotubes. *J. Am. Chem. Soc.*, 124:15076, 2002.

[109] Yu N. Gartstein, A. A. Zakhidov, and R. H. Bauhgman. Charge-induced anisotropic distortions of semiconducting and metallic carbon nanotubes. *Phys. Rev. Lett.*, 89:045503, 2002.

Acknowledgments

Curriculum Vitae

Name: Jannik Meyer

Date of birth: 16. 12. 1975

Place of birth: Herdecke (Germany)

Education:

1983 - 1987	Grundschule Blomberg
1987 - 1993	Städtisches Gymnasium Blomberg
1993 - 1994	Worth County High School, Sylvester, Georgia, USA
1994 - 1996	Städtisches Gymnasium Blomberg
1996	Allgemeine Hochschulreife (Abitur)
1996 - 2000	Rheinisch-Westfälische Technische Hochschule Aachen
2000	Chalmers University of Technology, Göteborg, Sweden
2001 - 2002	Rheinisch-Westfälische Technische Hochschule Aachen
	Diploma thesis: Phase contrast microtomography
2002	Physik Diplom, mit Auszeichnung
2002 - 2005	PhD thesis: Structure and Properties of Carbon Nanotubes

Miscellaneous

1998 - 2005	Stipend holder of the Studienstiftung des deutschen Volkes
1999	Internship at Matsushita Central Research Labs, Osaka, Japan

The PhD thesis "Structure and Properties of Carbon Nanotubes" was prepared at the Max Planck Institut for solid state research, Stuttgart, under the supervision of Dr. habil. S. Roth, and at the Eberhard-Karls-Universität, Tübingen, under the supervision of Prof. D. Kern, between Sept-01, 2002 and Nov-01, 2005.

My academic teachers were the following professors and lecturers:

Abramowicz, Bethke, Böhm, Capellmann, Güntherodt, Kern, Lengeler, Lübelsmeyer, Mokwa, Nordahl, Roepstorff, Roth, Schmitz, Schnakenberg, Schroer, Shumeiko, Wiegner